

Relative Merits of 3D Visualization for the Detection of Subtle Lung Nodules

Sarah Jonathan Boyce

A dissertation submitted to the faculty of the University of North Carolina at Chapel Hill
in partial fulfillment of the requirements for the degree of Doctor of Philosophy in the
Department of Biomedical Engineering

Chapel Hill
2013

Approved by:

Ehsan Samei, PhD

David Lalush, PhD

Marija Ivanovic, PhD

Henry Hsiao, PhD

Joseph Lo, PhD

©2013
Sarah Jonathan Boyce
ALL RIGHTS RESERVED

ABSTRACT

SARAH BOYCE: Relative Merits of 3D Visualization for the Detection of Subtle Lung Nodules. (Under the direction of Ehsan Samei)

A new imaging modality called bi-plane correlation imaging (BCI) was examined to determine the merits of using BCI with stereoscopic visualization to detect subtle lung nodules. In the first aim of this project, the optimal geometry for conventional projection imaging applications was assessed using a theoretical model to develop generic results for MTF, NNPS, eDQE. The theoretical model was tested with a clinical system using two magnifications and two anthropomorphic chest phantoms to assess the modalities of single view CXR and stereo/BCI. Results indicated that magnification can potentially improve the signal and noise performance of digital images. Results also demonstrated that a cross over point occurs in the spatial frequency above and below which the effects of magnification differ indicating that there are task dependent tradeoffs associated with magnification. Results indicated that magnification can potentially improve the detection performance primarily due to the air gap which reduced scatter by 30-40%. For both anthropomorphic phantoms, at iso-dose, eDQE(0) for stereo/BCI was ~100 times higher than that for CXR. Magnification at iso-dose improved eDQE(0) by ~10 times for BCI. Increasing the dose did not improve results. The findings indicated that stereo/BCI with magnification may improve detection of subtle lung nodules compared to single view CXR.

With quantitative results in place, a pilot clinical trial was constructed. Human subject data was acquired with a BCI acquisition system. Subjects were imaged in the PA position as well as two oblique angles. Realistic simulated lesions were added to a subset of subjects determined to be nodule free. A BCI CAD algorithm was also applied. In randomized readings, radiologists read the cases according to viewing protocol. For the radiologist trainees, the AUC of lesion detection was seen to improve by 2.8% ($p < 0.05$) for stereoscopic viewing after monoscopic viewing compared to monoscopic viewing only. A 13% decrease in false positives was observed.

Stereo/BCI as an adjunct modality was beneficial. However, the full potential of stereo/BCI as a replacement modality for single view chest x-ray may be realized with improved observer training, clinically relevant stereoscopic displays, and more challenging detection tasks.

DEDICATION

To daddy, for your unconditional love, your unwavering faith in my abilities, your pride in my accomplishments and telling me “you can never have enough education.”

ACKNOWLEDGEMENTS

I would like to thank my husband and children for their love and support throughout this long process.

Many, many thanks to Ehsan Samei for allowing me to study under his expert guidance and for his patient support.

I would also like to thank Varian Medical Systems, Inc. for equipment and for my co-workers there who inspired me to achieve this milestone. A special thank you to Rick Harris, if he had not hired me, I never would have started the journey.

Thank you to Planar Systems, Inc. for equipment used in this study. Thanks are also due to Robert Saunders and Brian Harrawood for image analysis routines. The author would like to thank Anne Jarvis, Brenda Prince, Rob Saunders, Ben Pollard, Amar Chawla and Xiang Li for help coordinating the clinical trial as well as Nicole Ranger and Jin Wooi Tan for coordinating the observer study. Than you to Michael Flynn of Henry Ford Health Systems, Detroit, MI for tshow software to optimize images for display and David Getty of BBN Technologies for SDMViewer software used for image display.

TABLE OF CONTENTS

ABSTRACT	iii
LIST OF TABLES	x
LIST OF FIGURES	xi
ABBREVIATIONS	xiv
1 Introduction	1
1.1 CHALLENGES OF CHEST IMAGING	1
1.2 DIGITAL DETECTOR TECHNOLOGY	4
1.3 COMPUTED RADIOGRAPHY	5
1.4 CCD/CMOS DETECTORS.....	7
1.5 FLAT PANEL DETECTORS	7
1.6 PHOTON COUNTING DETECTORS	11
1.7 COMPUTER AIDED DETECTION.....	12
1.8 APPLICATIONS FOR CHEST IMAGING.....	13
1.9 SLOT-SCANNING SYSTEMS	14
1.10 DUAL-ENERGY SYSTEMS.....	15
1.11 TOMOSYNTHESIS SYSTEMS	16
1.12 BI-PLANE CORRELATION SYSTEMS	17
1.13 OBJECTIVES AND ORGANIZATION.....	19
2 Imaging properties of digital magnification radiography	21
2.1 INTRODUCTION	21

2.2	METHODS	22
2.3	RESULTS	30
2.4	DISCUSSION.....	41
2.5	CONCLUSION.....	44
3	Physical evaluation of a high frame rate, extended dynamic range flat panel detector for real-time cone beam computed tomography applications.....	45
3.1	INTRODUCTION	45
3.2	METHODS	45
3.3	RESULTS	50
3.4	DISCUSSION.....	56
3.5	CONCLUSION.....	57
4	Effective DQE (eDQE) for monoscopic and stereoscopic chest radiography imaging systems with the incorporation of anatomical noise.....	59
4.1	INTRODUCTION	59
4.2	MATERIALS AND METHODS.....	60
4.3	RESULTS	68
4.4	DISCUSSION.....	78
4.5	CONCLUSION.....	81
5	Preliminary evaluation of bi-plane correlation (BCI) stereoscopic imaging for lung nodule detection	82
5.1	INTRODUCTION	82
5.2	METHODS	83
5.3	RESULTS	88
5.4	DISCUSSION.....	91

6	Observer study of a bi-plane correlated (BCI) stereoscopic imaging system for lung nodule detection	94
6.1	INTRODUCTION	94
6.2	METHODS	95
6.3	RESULTS	103
6.4	DISCUSSION	105
7	Conclusion	109
	REFERENCES.....	115

LIST OF TABLES

Table 2.1: Input parameters for MTF and NNPS calculations	29
Table 2.2: Input parameters for scatter calculations	30
Table 4.1: Phantom Size and Magnification Distance	62
Table 4.2: Exposure Condition	64
Table 4.3: Scatter and Transmission Fractions	74
Table 4.4: Hotelling SNR^2 per unit entrance exposure calculated to the detector plane under various noise conditions	77
Table 5.1: Observer Performance Statistics	91
Table 6.1: Observer Performance Statistics	105

LIST OF FIGURES

Figure 1.1 a. Posterior-Anterior chest radiograph and b. lateral chest radiograph.[53]	3
Figure 2.1: System MTF as a function of frequency for three magnifications. a. 100 micron pixel and 0.3 mm focal spot. b. 200 micron pixel, and 0.3 mm focal spot. c. 200 micron pixel and 0.1 mm focal spot. d. 50 micron pixel and 0.1 mm focal spot.....	31
Figure 2.2: Geometric sharpness as a function of magnification for three focal spot widths and four pixel sizes.....	33
Figure 2.3: Semilog plot of NNPS as a function of frequency for three magnifications and four pixel sizes for 74 kVp.	34
Figure 2.4: Plots of the DQE as a function of frequency for 74 kVp, three magnifications and two pixel sizes, 100 micron (a., b., c.) and 200 micron (d., e., f.).....	36
Figure 2.5: DQE_{eff} as a function of frequency for 74 kVp. a. shows the results for SID of 1 m and b. for SID of 2 m for 100 micron pixel and 0.1 mm focal spot. c. 100 micron pixel and d. 200 micron pixel for 0.3 mm focal spot and SID of 2 m. e. shows 100 micron pixel, 0.6 mm focal spot and SID of 2 m.	37
Figure 2.6: DQE_{eff} as a function of frequency for a 100 micron pixel, 0.3 mm focal spot, and 2 m SID. a. mammography (28 kVp). b. general radiography (74 kVp). c. chest radiography (120 kVp).	38
Figure 2.7: Plots of Hotelling SNR^2 efficiency for a 1 mm nodule and SID of 1 m and 2 m. a. 100 micron pixel and 0.3 mm focal spot. b. 100 micron pixel and 0.6 mm focal spot. c. 200 micron pixel and 0.3 mm focal spot. d. 200 micron pixel and 0.6 mm focal spot.....	39
Figure 2.8: Plots of optimal magnification vs. pixel size for three focal spots and two SIDS. a. mammography (28 kVp). b. general radiography (74 kVp). d. chest radiography (120 kVp).....	40
Figure 2.9: Plots of optimal magnification improvement (in terms of SNR^2) vs. pixel size for three focal spots. a. mammography (28 kVp). b. general radiography (74 kVp). d. chest radiography (120 kVp).	41

Figure 3.1: Linearity as a function of exposure (mR) for all exposures (a) and for lower exposures (b).....	51
Figure 3.2: Presampled spatial MTF as a function of frequency for frame rates 100, 500, and 750.....	51
Figure 3.3: NNPS _{lag} in units of mm ² versus frequency in units of cycles/mm for exposures ranging from 0.001 to 0.289 mR for frame rates 750 fps (a), 500 fps (b), and 100 fps (c).....	52
Figure 3.4: DQE versus frequency in units of cycles/mm for exposures ranging between 0.001 and 0.271 mR per frame for frame rates of 750 fps (a), 500 fps (b), and 100 fps (c). Figure d. is a plot of DQE(0) as a function of exposure for frame rates 100, 500 and 750 fps.....	54
Figure 3.5: (a) Profile of the LSF generated by exposing the detector for a long duration. (b) Profile of falling LSF determined by differentiating the extracted falling edge.....	55
Figure 3.6: The temporal MTF of falling LSF determined by using the long-exposure technique. The MTF was determined by exposing the detector with x-ray for a long duration of time.....	55
Figure 4.1: An anthropomorphic chest phantom (left) with realistic lung vessel structures (right).....	61
Figure 4.2: Examples of ROIs used for eNNPS calculations for single view CXR (a), stereo/BCI (b) and geometrical phantom (c).....	66
Figure 4.3: eMTF for adult (a) and large adult (b) phantoms at two different magnifications.....	69
Figure 4.4: CXR, stereo/BCI and geometrical phantom results for eNNPS: adult phantom at E=E ₀ (a), adult phantom at E=3.2E ₀ (b), adult phantom 50% magnification at E=E ₀ (c), adult phantom 50% magnification at E=3.2E ₀ (d), large adult phantom at E=E ₀ (e), large adult phantom at E=3.2E ₀ (f), large adult phantom 50% magnification at E=E ₀ (g), large adult phantom 50% magnification at E=3.2E ₀ (h).....	72
Figure 4.5: CXR, stereo/BCI and geometrical phantom results for eDQE: adult phantom at E=E ₀ (a), adult phantom at E=3.2E ₀ (b), adult phantom 50% magnification at E=E ₀	

(c), adult phantom 50% magnification at $E=3.2E_0$ (d), large adult phantom at $E=E_0$ (e), large adult phantom at $E=3.2E_0$ (f), large adult phantom 50% magnification at $E=E_0$ (g), large adult phantom 50% magnification at $E=3.2E_0$ (h).	76
Figure 5.1: BCI acquisition system[22]	84
Figure 5.2: BCI acquisition geometry where the angle $\alpha = 3^\circ$ as measured from the center of the beams.	85
Figure 5.3: Sample images (a-b) and zoom images of lesion (c-d)	86
Figure 5.4: Stereoscopic viewing system.....	87
Figure 5.5: Schematic of stereoscopic image formation[94]	88
Figure 5.6: ROC performance of PA study as dashed lines and BCI study as dotted lines for 4 radiologists (a-d). and e. Average of ROC curves	90
Figure 6.1: BCI acquisition geometry where the angle $\alpha = 3^\circ$ [15]	97
Figure 6.2: Stereoscopic viewing system.....	102
Figure 6.3: ROC curves for 8 radiologists, dashed lines are for stereoscopic while solid lines are for monoscopic. Figures a.- d. are results for experienced radiologists while e. – h. are results for inexperienced radiologists.....	104

ABBREVIATIONS

ALER	alternate line erasure and readout
a-SE	amorphous selenium
ASICs	application specific integrated circuits
AUC	area under the curve
BCI	bi-plane correlation imaging
CAD	computer aided detection
CCD	charge coupled device
CdTe	Cadmium Telluride
CMOS	complementary metal-oxide semiconductor
CNR	contrast to noise ratio
CR	computed radiography
CsI	cesium iodide
CT	computed tomography
CXR	Chest x-ray
CZT	Cadmium Zinc Telluride
DCE	detail contrast enhancement
DQE	detective quantum efficiency

eDQE	effective DQE
eMTF	effective MTF
eNNPS	effective normalized NPS
ESF	edge spread function
FOV	field-of-view
FP	false positive
FPS	frames per second
GaAs	Gallium Arsenide
HPM	chest radiologist
IEC	International Electrotechnical Commission
IRB	institutional review board
LSF	line spread function
MRMC	multi-reader, multi-case
MTF	modulation transfer function
NLST	National Lung Screening Trial
NNPS	normalized noise power spectrum
NPS	noise power spectrum
PA	posterior-anterior
PMT	photomultiplier tube

PPV	positive predictive value
ROC	Receiver operating characteristic
ROI	region of interest
Si	Silicon
SID	source-to-image plane distance
SNR	signal-to-noise ratio
s-Si	amorphous
TFT	thin-film transistor

CHAPTER 1

Introduction

The leading cause of death due to cancer in the United States is lung cancer which results in almost one third of total deaths from cancer.[3] More women die from lung cancer every year than breast cancer.[3] Although smoking is considered the main cause of most lung cancer incidence, nonsmokers constitute 10-15% of lung cancer cases.[122, 138] The 5 year survival rate for lung cancer is only 16% but if detected early, the 5 year survival rate increases to 53%.[3] Unfortunately, only 15% of cases are detected in early stages while localized.[3] Early detection is the key to survivability. Unfortunately, for lung cancer, there is no standard screening program like mammography for breast cancer and therefore, most lung cancers are detected during screenings for other purposes at later stages. A lung cancer screening program has not proven effective.[54, 91] This dissertation examines bi-plane correlation imaging (BCI) with stereoscopic visualization as a new modality for use in lung cancer detection. The introduction provides a description of the challenges of imaging the chest, an overview of digital detectors and computer aided detection as well as a summary of applications for chest imaging.

1.1 CHALLENGES OF CHEST IMAGING

Today, chest radiography is the most common method of imaging for thoracic diseases.[76] In 2006, an estimated 129 million chest radiographic procedures were performed, more than double the second most common radiographic procedure and almost 4 times the number of mammographic procedures.[82] Although a common procedure, interpretation of a chest radiograph is quite difficult and has been shown to have a miss rate of 26-90% in the detection of lung carcinomas.[11] Due to complicated

chest anatomy, detecting subtle lung nodules with chest radiography is limited by contrast to noise ratio (CNR), anatomical noise, and perceptual errors.[102]

Chest anatomy requires a large field of view which includes high contrast bony structures and soft tissue structures as well as mostly transparent lung tissue. Examples of chest radiographs can be seen in Figure 1.1. The ribs and sternum are large bony structures surrounding the lungs which attenuate x-rays more than lung tissue. The mediastinum is the area between the lungs which comprises the trachea, esophagus, bronchi, lymph nodes and the heart as well as large veins and arteries of the heart. These soft tissue structures are also much denser than lung tissue attenuating x-rays more effectively resulting in high contrast structures. X-ray transmission through the different structures of the thoracic cavity can vary by as much as two orders of magnitude.[76] Visualization of low contrast features over two orders of magnitude is a challenging task. Adequate penetration of denser structures in the thoracic cavity also necessitates larger tube potentials which further reduce contrast.[76] The higher tube potentials necessary together with the soft tissue structures results in Compton scattering which adds another type of noisy background and negatively affects the image contrast especially of low contrast features.[76] Scattering in a system without a grid can account for up to 70% of the x-rays detected in the lung region.[76]

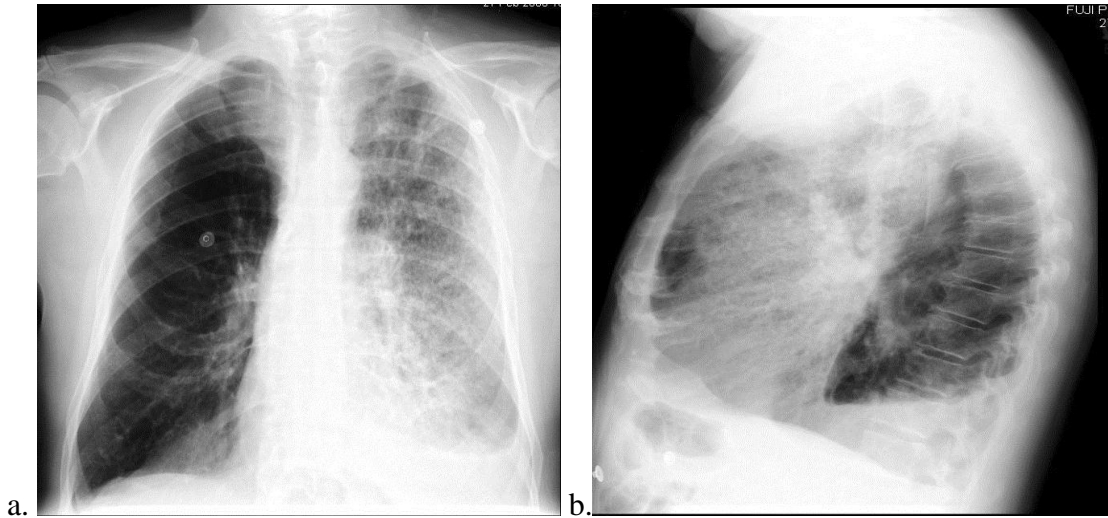


Figure 1.1 a. Posterior-Anterior chest radiograph and b. lateral chest radiograph.[53]

Chest radiography is the projection of a 3D structure onto a 2D image. Therefore, the bony and soft tissue structures contribute to anatomic noise by potentially blocking the view of lung nodules. Additionally, fine pulmonary vessels are numerous throughout the lung to provide an efficient exchange of oxygen. These structures form an overall anatomically noisy background in chest radiography. Samei and colleagues demonstrated that anatomic noise prevents detection of subtle lung lesions more than radiographic noise.[108, 110] For a reader to distinguish a lesion in a background of anatomical noise, the lesion needs to be an order of magnitude larger than the same lesion on a quantum limited background.[110] Another report determined that anatomical obstructions result in a 71% miss rate.[130]

Perceptual errors in chest radiography result in a miss rate of 10-22%.[130] Kundel et al classified observer perceptual errors as scanning errors, recognition errors and decision making errors.[67] Scanning errors occur when the observer does not sufficiently search the image for lesions and may account for as much as 30% of missed

lesions.[67, 76] Recognition errors occur when the observer has insufficient dwell time in the area of the lesion and account for approximately 25% of missed lesions.[67, 76] Decision making errors account for an estimated 45% of missed lesions, and occur when the observer adequately dwells on the lesion but makes an incorrect decision.[67, 76] The decision making process is hindered by the complicated anatomy of the chest.[93]

In conclusion, the chest radiograph contains several high contrast objects which also block the lungs and are superimposed on a noisy background. The contrast to noise ratio has been improved by the introduction of flat panel imaging systems.[35, 101, 104] However, numerous structures in chest anatomy may prevent observers from cognitively recognizing pulmonary lesions. If the miss rate from perceptual errors and anatomical obstructions could be improved on the chest radiograph, lung cancer detection would be more effective. The ability to view a chest radiograph in 3D may aid in visual suppression of the anatomical noise.

1.2 DIGITAL DETECTOR TECHNOLOGY

In November of 1895, W. C. Roentgen discovered x-rays and two weeks later, obtained an image of his wife's hand.[139] For almost a century, screen-film systems were the most common form of radiographic imaging system. In the mid 1970s, digital radiography systems became commercially available.[99] Digital detectors have become more prevalent in clinical practice. Improvements in memory capacity and processor speeds of computers, as well as improvements in detector materials and smaller electronics are some of the advances that have paved the way for digital detector technology. Digital technologies in use today include computed radiography, charge

coupled device (CCD) or complementary metal-oxide semiconductor (CMOS) based detectors, flat panel detectors and the emerging technology of photon counting detectors.

1.3 COMPUTED RADIOGRAPHY

The first digital radiography systems were computed radiography (CR) systems. The first CR systems were storage phosphor systems which trap a latent image on a photostimulable phosphor (usually BaFBr or RbBr) screen. A laser beam is used to extract the latent image which is then detected with a photomultiplier tube (PMT) the output of which is digitized to form the image. These systems provide a much better dynamic range than screen-film systems while maintaining flexibility for bedside applications and are easy to retrofit in existing screen-film systems. The screens can also be reused for thousands of exposures unlike film. The screen depth dictates the effectiveness of captured photons but also affects resolution. A thicker screen will have better stopping power at the expense of decreased resolution. Further reduction in resolution occurs because the laser beam has a spread at increased depth. Storage phosphor CR systems lose half the stored signal because the screens emit light promptly when exposed to radiation.[121] The laser beam activates fewer electrons at increased depths resulting in a loss of 30% of potential signal and some of the light signal is attenuated before reaching the surface.[120] Therefore, storage phosphor CR systems are less efficient with lower image quality than other digital technologies[35, 99, 103] and require a higher dose than other digital technologies.[120]

Commercial CR systems are usually composed of BaFBr or RbBr granular phosphors but structured CsBr phosphors (similar to CsI phosphors used for indirect flat panel detectors) have shown improved detective quantum efficiency (DQE) approaching

that of flat panel detectors.[97, 120] The structure of CsBr phosphors increases the DQE by channeling light better than granular phosphors and by allowing for a thicker phosphor without loss of resolution.[97, 120] An initial bedside clinical study with CsBr demonstrated improved low-contrast resolution and potential dose reduction compared to a BaFBr system.[63]

Dual-sided CR systems are made of transparent detector material with two optical systems to guide and collect emitted light from the front and back of the detector when scanned by a laser beam. The detection efficiency of the system is improved since more of the trapped electrons are released and the detector material can be thicker increasing x-ray absorption efficiency by approximately 50% while not suffering a loss in resolution.[24, 97] The two signals are combined resulting in over 30% improvement in signal-to-noise ratio (SNR).[134] The DQE of the dual-sided system approached the DQE of flat panel detector systems.[134] Dual-sided CR has been shown to improve detection of chest lesions on a phantom better than storage phosphor CR.[134]

A new scanning technique to replace the laser scanning is line scanning CR that simultaneously reads a row of pixels using a linear array of laser diodes.[24] The light emission is focused and collected by optics and a linear array of CCD photosensors. This technology provides twice the readout speed of typical laser scanning CR systems.[24] The design is also more compact and provides better photon collection.[24, 120] A recent study of five different CR systems concluded that a line scanning, structured phosphor system demonstrated DQE approximately double that of traditional storage phosphor systems.[97]

1.4 CCD/CMOS DETECTORS

CCD- and CMOS-based detectors are integrated detector arrays optically coupled to an x-ray phosphor. When the phosphor is stimulated, light is emitted that is sent to a CCD or CMOS camera which forms a radiograph. CCD and CMOS sensors are typically noisy due to light collection inefficiency. The detector is smaller than the phosphor requiring the original image to be reduced in size resulting in an inefficient system since only a small fraction of light photons are detected by the camera. The loss of light in this manner is often referred to as a secondary quantum sink. Another disadvantage for CCD technology is a very limited surface area due to cost, thus, CCDs cannot be used for large area arrays which limits the field of view. Using multiple detectors improves the efficiency but increases the cost and requires stitching smaller images together to form the full image. CMOS technology provides pixel level electronics that improve the financial restrictions of a large area array. However, excessive noise and high dark current remain issues. Thick housing necessary to accommodate the electronics makes retrofitting difficult.[141] The DQE of CCD/CMOS detectors has been shown to be lower than that of flat panel detectors.[116] Due to the size limitations, most CCD/CMOS detectors have been used for mammographic and dental applications except for slot-scanning applications for chest (discussed later in this introduction).

1.5 FLAT PANEL DETECTORS

Imaging modalities such as bi-plane correlation imaging are feasible with the use of flat panel detectors because of the large field-of-view (FOV), fast acquisition and relatively high DQE. Flat panel detectors have been shown to be more efficient than

other digital technologies,[35, 84] to have better contrast to noise ratio[35, 101, 104] and provide the ability to acquire digital images quickly.

Flat panel detectors are direct or indirect in design. Direct designs use a photoconductive layer of amorphous selenium (a-Se) that converts x-ray energy to an electronic charge. The electronic charge is then guided by an electric field to a storage capacitor. Indirect designs use a phosphor layer which can be made of a GadOx (Gd_2O_2S) screen or cesium iodide (CsI) that converts x-ray photons to visible light photons that is then converted to a charge by a photodiode. The charge is then stored in a capacitor until readout. CsI is a structured phosphor which produces better conversion leading to improved DQE and lower dose; as such, CsI is typically used in medical applications.[101] Both approaches use amorphous silicon (a-Si) array technology found in laptops. The individual pixels comprise a storage element and a switching element. The sensing element has an associated fill factor which depends on the size of the pixel. The switching device used is typically a thin-film transistor (TFT).

The concept of the image pixel is simple: the pixel is charged by the x-ray photons incident and then read accordingly when the switching device is activated. However, design of the pixel results in various tradeoffs. Not only are there cost consequences for fabrication when designing smaller pixels, but the amount of charge that can be detected is also affected, particularly for indirect designs. For direct designs, the electric field shaping within the photoconductor guides the charge to individual pixels allowing the entire a-Se surface to be available for x-ray conversion.[23, 141] This type of conversion process results in efficient pixels with fill factors approaching 100%.[23] For indirect designs particularly, a smaller pixel pitch results in a smaller fill factor which

improves the resolution of the panel but is more costly to fabricate and less efficient since fewer photons will be detected.

The a-Si array is a 2D rectangular array comprised of pixels where each row of pixels is connected to the same horizontal control line and each column of pixels is connected to the same vertical data line. Once an x-ray exposure is made, the information in the storage elements is read one line at a time such that all the pixels in that row are connected to their corresponding data line. With TFT switches, the readout of the capacitor resets the pixel preparing it for the next charge. The readout proceeds line by line and takes approximately 30-50 msec to complete readout of the full array. A-Si technology suffers from charge carryover or ghosting effects due to charge trapping in the a-Si elements[16, 128] and sensitivity variations in the photoconductor or phosphor.[141] Once the array is read, the signal is amplified by application specific integrated circuits (ASICs) tailored to the specific characteristics of the a-Si array. The noise components of the ASICs must be closely monitored. After the signal is amplified, it is digitized and stored. To maintain a compact profile, the electronics are typically folded beneath the array using a flexible tab package. However, the compact design also leads to thermal drift issues requiring frequent dark current calibrations.

Direct detectors exhibit nearly perfect modulation transfer function (MTF) since there is no phosphor for light spread. The MTF of indirect detectors is comparable to that of CR systems. The noise power spectrum (NPS) of direct detectors is similar to white noise. The light spread in indirect detectors generally improves the NPS by introducing blur into the system, thus noise is reduced compared to direct detectors. The absorption of the phosphor found in indirect detectors results in a better DQE for lower frequencies

but the almost ideal MTF of the direct system results in a better DQE for higher frequencies. This indicates there is a task dependent tradeoff such that direct detectors may exhibit improved performance for high detail and high contrast structures and indirect may have improved performance for low contrast objects in noisy backgrounds like chest radiography.[105] Bacher, et al confirmed this result in an observer study to compare direct and indirect flat panel detector systems when detecting subtle lung nodules.[7] A recent study for chest radiography showed that a reduced dose could be used with an indirect system that achieved equal or superior performance compared to a direct system.[7]

The DQE of flat panel detectors has been found to be better than that of CR systems.[104] Due to the various stages of signal loss in CR systems compared to indirect flat panel detector systems, this result is not unexpected. One study concluded that an indirect flat panel detector could be operated at exposure levels 3.7 times lower than a comparable CR system.[104] Flat panel detectors have inherent dark current noise that CR systems do not possess.[99] Currently, flat panel detectors are more expensive than CR systems but work is being done to reduce the cost while flat panel detector technology continues to improve. Advances under investigation to improve the gain and thus the SNR include replacing discrete photodiodes in indirect designs with a continuous photodiode to increase the pixel fill factor, using amplifier circuits in the pixel for direct or indirect designs and incorporating photoconductive materials with higher signal conversion such as PbI_2 , HgI_2 and PbO in direct systems.[30]

1.6 PHOTON COUNTING DETECTORS

A promising technology beginning to attract more attention in digital radiography is photon counting detectors. X-ray sources used in medical imaging produce bremsstrahlung radiation which has a broad energy spectrum. Previous detectors discussed based on phosphor technology are integrating systems which integrate all energies into a single energy bin. With photon counting detectors, x-ray energy discrimination can be performed such that the low energies enhance the softer tissues while high energies enhance harder tissue like bone. Photon counting detectors possess low noise, linearity and infinite dynamic range[36, 123] while providing the ability to reject scatter, improve SNR and decrease dose.[98] Compositions of GaAs (Gallium Arsenide), Si (Silicon), CdTe (Cadmium Telluride), and CZT (Cadmium Zinc Telluride) as well as others under investigation have been used for photon counting detectors.[98] Several issues with this technology need to be resolved such as energy window optimization or resolution, spatial resolution, choice of detector material, and fabrication complications.[36, 98, 123] Narrow energy window selections will result in quantum limited noise while wider energy windows will result in less energy discrimination or resolution. Spatial resolution depends on the pixel size but is also affected by blurring due to charge sharing between pixels.[123, 126] Charge sharing depends upon the thickness of the material and the applied electric field.[126] Detector materials used need to have good absorption of incident photons and be resilient when exposed to high temperatures and shearing while maintaining minimum leakage which allows for more of the detector to be charged.[74, 123] Fabrication of photon detectors is currently a

challenging task but as electronic circuits continue to be improved, fabrication should become more feasible with minimal spacing between pixels for lower cost.

1.7 COMPUTER AIDED DETECTION

Approximately 30% of lung nodules are not detected during a first reading but can be detected when viewed retrospectively.[66, 85] As previously discussed, perceptual errors by the observer result in a high miss rate and observers are known to have subjective and inconsistent decision criteria.[44] Due to time and cost constraints, having an observer perform a second reading is not always practical; therefore, computer aided detection (CAD) can be used as a second reader by directing the attention of the observer to suspect nodules. CAD involves the segmentation, extraction and identification of potential pulmonary nodule candidates. CAD algorithms start with image enhancement in the form of histogram equalization and filtering. As stated previously, the biggest hurdle to lung nodule detection is overlapping anatomy in chest radiography. Therefore, the first step after initial image enhancement in CAD routines is the suppression of overlying anatomy typically by means of image subtraction techniques that attempt to remove normal structures like ribs and soft tissue. Lung field segmentation using rule-based reasoning or pixel classification is performed to limit the search area.[45] Initial nodule candidates are then determined by various methods including filtering and unsharp masking to enhance the nodules and then template matching or Hough transforms to detect candidates. Specific nodule features such as radius, circularity, diameter, curvature, ellipticity and contrast are then used to minimize the set of false positives. The final detected set of nodules is presented to the observer to act as a second reader. Reducing the number of false positives while detecting true

positives accurately is a difficult task. Using data from multiprojection images to correlate the CAD findings could result in further reductions of false positives.[102, 117] Limited commercial options for chest CAD (Edda Technology and Riverain Technologies) currently exist, but CAD could become a useful tool in clinical settings as techniques/algorithms continue to evolve. CAD as a second reader with a commercially available system has been shown to improve the detection of lung nodules with chest radiography and to be more effective for less experienced radiologists.[61, 70] Work still remains to test the clinical effectiveness of CAD on large data sets.

1.8 APPLICATIONS FOR CHEST IMAGING

Recently, the National Lung Screening Trial (NLST) has shown a 20 percent decrease in death due to lung cancer.[60] The NLST used computed tomography (CT) as the image screening tool. CT limits anatomical obstructions compared to chest radiography; however, in comparison, CT requires a much higher radiation dose. One study reported that the average effective dose from a chest posterior-anterior (PA) exam is 0.039 mSv while the average effective dose of a chest CT exam is 3.2 mSv.[142] The number of CT exams has increased rapidly in the last decade and CT is one of the largest sources of radiation exposure from medical imaging.[12, 18, 32, 51, 81] One study reported that CT and nuclear imaging procedures were performed on 21% of the study population but the exposure was 75.4% of total effective dose.[32] In contrast, 71.4% of the population received radiography exams which comprised only 10.6% of the total effective dose.[32] Dose reduction strategies for CT are being pursued;[77] however, CT exams are a larger financial burden that require more extensive postprocessing techniques compared to chest radiography. Although CT may prove to be an effective screening

tool, a low dose, low cost option would also be beneficial. Lower dose applications currently available that minimize anatomical structure noise are dual-energy[5, 69, 100] and tomosynthesis[28, 29, 136]. Slot-scanning systems have also demonstrated improved detection of subtle lung nodules through reduced scatter. Bi-plane correlation imaging is a recently proposed application for detecting subtle lung nodules.

1.9 SLOT-SCANNING SYSTEMS

Slot-scanning systems incorporate a moving CCD based detector synchronized with a moving beam source that is collimated to produce a narrow fan beam. The collimated beam eliminates the need for an anti-scatter grid while providing better scatter rejection than full field applications with anti-scatter grids. One study of a slot-scan system for chest reported scatter fraction reductions of 22-25% in the lung and 16-18% in the denser regions with an anti-scatter grid while the slot-scan system at the same tube potential demonstrated scatter fraction reductions of 54% and 47-57% respectively, a significant improvement.[111] In the same study, the PA dose from the slot-scan system was 16% higher than the full field chest system. Although the flat panel detector in the full field chest system has a higher DQE, the reduction of scatter in the slot-scan CCD system resulted in an improved SNR.[111, 116, 120] Slot-scan systems using CCDs require careful alignment and synchronization between the CCD detector and the fan beam.[72, 73] Slot-scanning systems have inefficient tube usage and the total imaging time is 1.3 seconds compared to 20 msec for standard PA studies[116]. Recent studies have investigated using flat panel detectors in slot-scan systems. The readout electronics of the flat panel detector are modified using an alternate line erasure and readout (ALER) technique.[72, 73] With ALER, the detector is read in synchronization with the fan beam

instead of line by line.[72, 73] The leading edge line is reset to erase the scatter component while the trailing edge is read to acquire the exposed image.[72, 73] Using this method with an 18 mm slot width, the scatter was reduced by over 86%.[72] Improved scatter rejection results in better image contrast.[72] As Liu, et al emphasizes, the scatter reduction is dependent on the slot width which is more easily altered with digital collimation. One concern with the ALER technique is adequate erasure of the scattered radiation but Liu, et al demonstrated that erasure is successful. A slot-scan system takes longer to acquire the image but only a small portion of the image is being acquired at any given time therefore, patient motion is not a significant factor.[72, 116] With slot-scan systems, there is a tradeoff between tube loading and slot width. A wider slot-width decreases the necessary tube loading at the expense of increased scatter.[72] Determining optimal imaging parameters remains an issue with slot-scan systems.

1.10 DUAL-ENERGY SYSTEMS

Dual-energy systems require a double exposure with different dose techniques which are then subtracted to remove anatomical structures, particularly bone and soft tissue. Dual-energy with CR systems allows the low and high energy images to be recorded concurrently with a single exposure. The CR system is composed of a copper filter between two plates. The first plate records a typical PA chest image, and then the copper filter hardens the beam such that the second plate records the higher energy beam. Since the two images are taken in one exposure, there is no time delay and therefore, no patient motion so the two images can be subtracted cleanly. Dual-energy with flat panel detectors requires two exposures in which, although only separated by milliseconds, patient motion is detectable. The flat panel detector types of dual-energy systems require

post-processing for noise reduction and image registration.[96, 100] When the two images are subtracted, edge artifacts typically exist in the bone and tissue images.[5, 34, 76] The flat panel detector dual-energy systems have better energy discrimination and lower noise due to better image quality than the CR systems[5] but are higher dose. Recent studies of dual-energy systems in conjunction with PA chest radiographs demonstrated improved detection, but the value of the modality for lung nodule detection and type of imaging parameters employed are still under discussion.[69, 100] Flat panel detector systems also provide the ability for dynamic dual-energy studies. Recent advances demonstrated feasibility of dynamic dual-energy flat panel detector systems for use in functional lung imaging and tumor motion.[140] Photon counting detectors composed of CdTe recently developed for use in a dual-energy application demonstrated count rates and noise limits suitable for use in dual-energy radiography applications.[8]

1.11 TOMOSYNTHESIS SYSTEMS

Tomosynthesis is a form of limited angle tomography that provides a reduction in anatomical noise similar to CT at a much lower dose and cost.[28, 136] Tomosynthesis systems incorporate a conventional x-ray tube source, digital detector and a custom tube mover allowing for easy implementation. Most tomosynthesis images are acquired in the conventional PA projection. The high DQE and scanning rate of flat panel detectors have made tomosynthesis practical for clinical use. Imaging time for tomosynthesis is typically one breath hold or about 10-11s and the dose is comparable to conventional chest radiography.[29] Similar to CT, projection images are acquired as the x-ray tube moves, for tomosynthesis, movement occurs along a vertical path. The projection images are then reconstructed to form the final image. The first step of the reconstruction is a

simple shift and add equivalent to simple backprojection.[29] Changing the shift parameter generates slices throughout the entire volume bringing different planes into focus. The shift and add technique is simple, but results in blur that must be minimized through various deblurring techniques including matrix inversion, filtered backprojection and iterative restoration.[29] Although tomosynthesis does not provide the depth resolution of CT, the performance is superior to conventional chest radiography. Recent clinical studies demonstrated improved detection of lung nodules using tomosynthesis compared to chest radiography.[26, 136] Tomosynthesis reconstructions may contain artifacts from the limited angle acquisition and further analysis needs to be performed to ascertain clinical effectiveness in detection of pulmonary nodules.[28, 29, 136]

1.12 BI-PLANE CORRELATION SYSTEMS

A low dose, low cost, fast acquisition modality that may provide a feasible alternative for lung cancer screening without post-processing algorithms is bi-plane correlation imaging (BCI) with stereoscopic display. The use of stereo/BCI has become feasible with flat panel detector systems which provide fast acquisitions necessary for minimal motion artifacts resulting in successful correlation without the use of registration algorithms. Viewing bi-plane correlation images in 3D on a stereographic display will suppress anatomical obstructions. Studies for stereomammography have shown that stereo/BCI of the breast is feasible.[42, 43, 119] Preliminary studies of BCI for chest using phantoms and a small patient subset demonstrated that chest BCI is feasible.[102, 117] The preliminary studies also explored the use of computer-aided detection (CAD) with the correlated images.[88, 89, 102, 117] CAD algorithms as second readers in chest radiography have been shown to improve detection rates, but CAD algorithms often

result in high false positive findings.[13, 61] The angular images from BCI provide correlated data to use in CAD algorithms which improve the false positive rate.^{5,25}

Viewing the bi-plane images stereoscopically provides the radiologist with a visual reduction of anatomical noise. Stereoscopic photography was popular at the turn of the twentieth century and physicians at that time developed techniques for viewing medical images stereoscopically.[42] Viewing the x-ray films required awkward handheld viewing devices and involved difficult alignment of the images.[42] However, stereoscopic imaging was used in radiology departments until CT and MRI systems became available.[42] Stereoscopic vision occurs because the human eyes are approximately 65 mm apart causing horizontal parallax so that the left eye and right eye receive slightly different views resulting in a horizontal angular disparity of points in the retinal images from each eye. Within the visual cortex, these two views are fused into a single view with depth perception. Stereoscopic monitors are designed to display the left image only to the left eye and the right image only to the right eye. Two types of monitors exist for viewing images stereoscopically. Autostereoscopic monitors do not require the use of special glasses or headgear while stereoscopic monitors do require the use of special equipment.

Autostereoscopic monitors use parallax barriers or lenticular lenses. Parallax barriers interleave the left and right eye images on the display. Early systems did this with various types of grid plates that provided vertical strips alternating the left and right images but recent technology uses tiny lenses integrated into the layered liquid crystal displays. Each layer contains small stripes that hide specific pixels such that some are only seen by the right eye and others only by the left eye. However, the observer needs

to remain in a fixed location. Lenticular lens sheets contain lenses that refract left and right images. Recent advances in 3D monitor technology have multiple lenticular lenses at different angles so the observer does not need to remain in a fixed position since the image received depends on the viewing angle.

Stereoscopic displays that require special viewing equipment simultaneously provide left and right images through separate channels and are said to be spatially multiplexed.[42] Analog methods of separating the channels either split the screen into left and right images or uses two monitors to display the left and right images. Then a device with mirrors and optics is attached to the system to deliver the appropriate image to the appropriate eye. The images can be displayed on a single monitor using temporal multiplexing where the left and right images are alternately displayed. These systems require optical shutters in the eyewear to insure that the left image is only shown to the left eye and the right image is only shown to the right eye and the shutters in the eyewear have to be synchronized to the display and require a high refresh rate to avoid flicker.

1.13 OBJECTIVES AND ORGANIZATION

This study explores the feasibility of stereo/BCI systems for detecting subtle lung nodules in human subjects by optimizing system geometry, investigating the effective DQE (eDQE) of a clinical imaging system, characterizing flat panel detectors and stereoscopically viewing bi-plane images in observer studies. The work was undertaken to assess the effectiveness of BCI viewed stereoscopically for detection of lung nodules.

The first part of the study involved a theoretical assessment of system geometry for standard PA chest exams and extension of the DQE to analyze the effective DQE (eDQE) of a clinical chest radiography imaging system. The characterization of a

commercially available CsI flat panel detector was also performed. Initial introduction of flat panel detectors resulted in a simple substitution of the flat panel detector for the analog screen film or CR cassette. Studies have since shown that flat panel detectors improve DQE such that dose can be reduced compared to screen film and CR.[33, 35] However, the optimal system geometry of flat panel detectors has not been sufficiently evaluated. In Chapter Two a theoretical framework was established to assess the tradeoff of different geometries for standard PA acquisitions. The flat panel detector used for the prototype bi-plane correlation system was characterized for image quality in Chapter Three. DQE has been the standard metric used to describe system performance; however, DQE is a detector specific metric.[112] The eDQE has been investigated as a metric to more accurately describe overall system performance.[113] Chapter Four examines the eDQE of a clinical system used for chest radiography.

For the second part, observer studies were performed on bi-plane human subject data viewed stereoscopically. The BCI system acquired a PA image as well as images at oblique angles or ± 3 degrees of PA in the horizontal direction as determined in previous studies.[88, 89, 102, 117] Chapter Five reports the preliminary results of the observer study. After the preliminary study, simulated lesions were added to the normal cases and the order of viewing the images was modified for a second observer study. In addition, a correlated CAD algorithm was used to act as a second reader during the second observer study. Chapter Six reports the results from the second observer study.

CHAPTER 2

Imaging properties of digital magnification radiography

2.1 INTRODUCTION

Flat panel detectors are becoming increasingly prevalent in the imaging market for many applications including those in medicine, veterinary medicine, and manufacturing. Studies are being performed to use these devices in all areas of clinical radiology including diagnostic radiography, fluoroscopy, and mammography, as well as research areas of tomosynthesis and cone beam computed tomography (CT).[78, 79] In most situations, flat panel detectors have simply replaced the current receptor in a system without changing other parameters of the acquisition such as the geometry. Several studies have been performed to show that flat panel detectors offer improved SNR over competing technologies.[6, 21, 38, 49, 127] However, some studies have suggested potential benefits of magnification for various radiology examinations using film or flat panel detectors.[14, 86, 124, 129, 132] In particular, standard clinical practice is to use magnification mammography with film-screen systems for diagnostic follow-up to screening mammography.[25, 52, 68, 75, 92] To date, clinical applications have not taken advantage of the improvements offered by magnification.

The goal of the current work was to examine the effects of geometry by studying the impact of magnification on image quality in radiographic imaging. A theoretical model was developed to investigate how the geometry of image acquisition with a flat panel detector can be optimized in terms of various acquisition parameters such as focal

spot size, pixel size, SID (source-to-image plane distance), and air gap. The image quality for optimization was assessed using standard metrics, MTF, NPS, DQE, and effective DQE (eDQE).[111, 116] Furthermore, the framework was applied to three specific imaging applications, mammography, general radiography (also applicable to mammotomography[79]), and chest radiography, to investigate how these applications can be optimized from a geometrical perspective.

2.2 METHODS

This work uses the traditional cascaded system model of source-object-detector-observer to study optimum geometry. Optimum geometry is determined by examining image acquisition parameters that affect system performance in terms of resolution, noise, SNR, and SNR in the presence of scattered radiation. Traditional image quality parameters such as MTF for resolution, NPS for noise characterization, DQE for SNR, and effective DQE for overall SNR are examined in terms of tradeoffs between image acquisition parameters such as focal spot size, SID, air gap, and pixel size. These image quality parameters are adequately described in Fourier space if the system is assumed to be shift invariant and linear.[127] When possible, these metrics are reduced to scalar figures of merit to characterize the overall system performance.

All image quality characteristics are determined in the frequency domain of the object plane denoted by primes with u' representing the frequency in the object plane and u representing the frequency in the image plane. Thus, if the resolution limit (i.e., the cutoff frequency or highest spatial frequency which can be reliably reproduced) is represented by f in the image plane, then the resolution limit in the object plane is $f' = mf$,

where m is the magnification factor. For simplicity, all model calculations are performed for a single dimension and assumptions made for calculations are equally applicable to the two dimensional case. The linearized-single dimension treatment provides a reasonable approximation for inherent response of a digital radiographic system, as long as the approximation does not extend to spatial frequencies close to the Nyquist frequency where the system response becomes non-stationary, violating one of the requirements of the linear system analysis.

2.2.1 Modulation Transfer Function Model

The modulation transfer function (MTF) as a function of the amplitude of the Fourier transform of the point spread function versus spatial frequency is the most common metric to characterize the spatial resolution of an imaging system.[90, 103, 104, 118] The MTF is often characterized in the image plane. In the object plane, the system MTF, $MTF(u') = MTF(u/m)$, represents the MTF in the image plane scaled by magnification.

In Fourier space, the total MTF for the system results from multiplying the MTFs of the individual system components. Our model includes the resolution of two components, the detector MTF and the focal spot MTF.

The MTF for the detector is derived in the object plane by treating the pixel and the phosphor as two separate elements of the detector. The theoretical phosphor MTF where u' is the spatial frequency in the object plane, assumes the form

$$MTF_{\text{phos}}(u') = \left(\frac{1}{2} \right) \text{erfc} \left[\alpha \ln \left(\frac{u'}{u_o} \right) \right], \quad (2.1)$$

based on the Burgess model for phosphors which has been shown to correspond well with empirical data.[19, 103] For this model, α is the slope and u_0 is the frequency where the MTF is 0.5. The pixel MTF is modeled as a sinc function,

$$\text{MTF}_{\text{pix}}(u') = \frac{\sin(w_{\text{pix}} u')}{w_{\text{pix}} u'} , \quad (2.2)$$

where w_{pix} is the pixel width assuming square pixels. The total detector MTF which combines Eqs. (2.1) and (2.2) is then

$$\text{MTF}_{\text{panel}}(u') = \text{MTF}_{\text{pix}}(u') \text{MTF}_{\text{phos}}(u') . \quad (2.3)$$

Although the source distribution may be complex,[9] the MTF associated with the focal spot blur may be reasonably modeled using a Gaussian distribution as in previous work by Siewerdsen and Shaw[124, 129]

$$\text{MTF}_{\text{fs}} = e^{-\pi \left(\frac{m-1}{m} w_{\text{fs}} u' \right)^2} , \quad (2.4)$$

where w_{fs} is the full width at half maximum (FWHM) of the focal spot and m is the magnification. The presampled system MTF in the object plane can therefore be represented as

$$\text{MTF}(u') = \text{MTF}_{\text{panel}}(u') \text{MTF}_{\text{fs}}(u') . \quad (2.5)$$

Geometric sharpness[129] provides a scalar figure of merit for characterizing the overall resolution across the frequency range. The geometric sharpness can be defined as the integral of the square of the MTF[129]

$$s_{\text{geo}} = \int_0^{f_N} \text{MTF}^2(u') du' , \quad (2.6)$$

where f_N is half the sampling rate and $\text{MTF}(u')$ is the system MTF from Eq. (2.5).

2.2.2 Noise Power Spectrum Model

A quantitative representation of the noise properties of flat panel detectors is commonly provided by the noise power spectrum (NPS) which can be thought of as the variance of image noise across various frequencies.[41, 103, 104, 135] In this work, the theoretical model for the presampled NPS ($NPS_{pre}(u)$) is based on the assumption that the correlated noise component is proportional to the receptor MTF^2 for a deterministic spreading stage which generalizes the model described by Siewerdsen[127] for a cascaded, linear flat panel detector. Thus

$$NPS(u) = \eta * MTF_{panel}^2(u) + NPS_{additive}, \quad (2.7)$$

where η is the scale factor accounting for specific receptor properties,[127] $NPS_{additive}$ represents the additive noise component from the gain stage of the digital detector and is assumed to have a scalar value, and MTF_{panel}^2 is the panel MTF obtained by aliasing the presampled MTF as,

$$MTF_{sam}(u') = MTF_{pre}(u') + MTF_{pre}(2f - u'), \quad (2.8)$$

where f is half the sampling rate. The normalized sampled NPS ($NNPS(u')$) is then obtained by performing a non-linear fit of the model in Eq. (2.7) to experimental data from a previous study.[103, 135]

The model provides the NPS in the image plane, $NPS(u)$. Since NPS is a function of area, the effect of magnification must be considered to account for the difference between the pixel size in the image plane and the effective pixel size in the object plane, thus

$$NPS(u') = \frac{1}{m^2} NPS(u/m) \quad (2.9)$$

represents the NPS in the object plane.[111, 116, 124]

2.2.3 Scatter Rejection Model

Compton scatter is the primary source of scattered photons associated with x-ray imaging and if detected, leads to a loss of contrast and added noise.[129] Increasing the object-image distance not only increases magnification, but also reduces scatter. Air gaps and grids are often used to reduce scatter. In this work, only the air gap technique is considered as it provides equivalent or even potentially superior scatter rejection performance compared to grids without any loss of primary radiation associated with grids.[64, 111]

The effects of scatter on the geometry are described using the effective scatter point source (ESPS) model first developed by Muntz et al.[87] Muntz et al. described scatter rejection from an air gap by defining an effective scatter point source located between the source and the exit surface of the object. In this model, the scatter-to-primary ratio at the image plane (SP) can be calculated as

$$SP = SP_o \left(\frac{x_s}{x_s + g} \right)^2 m^2 = \frac{SF}{1 - SF}, \quad (2.10)$$

where x_s is the distance between the effective scatter source and the object exit plane, SP_o is the scatter-to-primary ratio at the object plane, g is the air gap distance, m is the magnification, and SF is the scatter fraction. Our model was modified such that the effective scatter point source is located between the source and the center of the object.

2.2.4 Detective Quantum Efficiency Model

The DQE is commonly used as an image quality metric for signal to noise exposure efficiency for flat panel detectors.[41, 90, 103, 104, 135] In this study, the DQE

is calculated in the object plane with the system MTF from Eq. (2.5) and the sampled NNPS as described in section II. B. as

$$DQE(u') = \frac{MTF^2(u')}{qEm^2NNPS(u')}, \quad (2.11)$$

where q is the square of the ideal signal-to-noise ratio (SNR^2) per exposure with units of $mm^{-2}\cdot mR^{-1}$ and E is the exposure in units of mR . The m^2 factor accounts for the change in exposure as a function of magnification and cancels the $1/m^2$ factor inherent in the $NNPS(u')$, Eq. (2.9).

This model does not account for x-ray scatter effects that introduce extra noise into the image. To describe this effect, the effective DQE as proposed by Samei et al.[111, 116] is used,

$$eDQE(u') = t(1-SF)DQE(u'), \quad (2.12)$$

where t is the transmission of primary x-rays through the extra detector elements prior to reaching the detector, and SF is the scatter fraction that reaches the detector [where $SF = SP/(SP + 1)$].

2.2.5 Observer Model

While DQE and eDQE provide generic descriptions of SNR, they do not reflect the effects of a specific signal on object detectability. This can be achieved using the Hotelling SNR^2 which includes a signal term.[107] The Hotelling SNR^2 efficiency is the Hotelling SNR^2 per unit exposure defined as

$$F = 2\pi \int_0^{f_N} S^2(u')eDQE(u')u' du', \quad (2.13)$$

where $eDQE(u')$ is the effective DQE as defined by Eq. (2.12), and $S(u')$ is the Fourier transform of the nodule model.

The nodule was modeled using the designer profile defined by Samei and Burgess[20, 107] calculated using the Hankel transform

$$S_{\text{designer}}(u') = J_{n+1}(2\pi Ru') / (2\pi Ru')^{n+1}, \quad (2.14)$$

where $J_{n+1}(2\pi Ru')$ is a first order Bessel function, R is the diameter of the nodule, and n is an exponent defining the shape of the nodule. Values of n between 1 and 2 represent reasonable lesion approximation.

2.2.6 Model Input Parameters

Pixel sizes were varied within a 50-200 micron range. For each pixel size, the nominal focal spot sizes of 0.1, 0.3, and 0.6 mm were used. For each combination of pixel size and focal spot size, magnification values from 1 to 3 were considered. The initial MTF and NNPS experimental data were obtained at 28 kVp with exposure of 32.8 mR and a q of 53300 photons/mm²-mR,[135] 74 kVp with exposure of 0.27 mR and a q of 255855 photons/mm²-mR,[103] and 120 kVp with exposure of 0.24 mR and a q of 259231 photons/mm²-mR.[104] The MTF data were fitted to the Burgess model of Eq. (2.1) which was then assumed to have fixed α and u_0 values for model MTF calculations associated with each technique. The NNPS data were used to perform a nonlinear fit to the generic model in Eq. (2.7) which was then assumed to have fixed η and NPS_{additive} components. These assumptions were made as the thickness of the phosphor was not considered as a variable parameter in the model. Table 2.1 summarizes the input parameters for MTF and NNPS calculations.

Table 2.1: Input parameters for MTF and NNPS calculations

Energy (kVp)	Exposure (mR)	q (photons/mm ² -mR)	α	u_0	η (mm ²)	NPS _{additive} (mm ²)
28	32.8	53300	0.6894	4.3821	0.1943×10^{-4}	0.0360×10^{-4}
74	0.27	255855	0.6060	1.6044	0.2860×10^{-4}	0.0567×10^{-4}
120	0.24	259231	0.6060	1.6044	0.7068×10^{-6}	0.2819×10^{-6}

Table 2.2 summarizes input parameters for scatter calculations. The desired field size used was 120 cm². The tissue thickness (assumed uniform), x_s , and SP_0 values for 28 kVp were obtained from work done by Krol et. al.[64] while those for 74 kVp and 120 kVp were derived using a linear fit to data from Sorensen and Floch.[132] The SID was assumed fixed and the air gap distance was varied by moving the object. Two values for SID were used, 1 m and 2 m. The designer nodule was used with a diameter of 1 mm and an exponent of 2.

Table 2.2: Input parameters for scatter calculations

Application	Energy (kVp)	Tissue Thickness (cm)	x_s (cm)	SP_0
Mammography	28	6.2	16	1.00
General Radiography	74	8	15.78	2.01
Chest Radiography	120	8	13.79	2.32

2.3 RESULTS

From the multiple combinatorial set of model results for all the influencing parameters, the following results considered the effects of each of the factors, focal spot size, pixel size, scatter fraction, and SID, on magnification and the corresponding effects on the MTF, NPS, and DQE.

2.3.1 Effects of Magnification on MTF

The focal spot MTF degraded with magnification while the detector MTF improved with magnification. Representative results shown in Figure 2.1 demonstrate that the improvement of the MTF depended on the tradeoff between focal spot size and pixel size. A large focal spot (0.6 mm) resulted in little or no resolution improvement with the use of geometric magnification. Since the focal spot blur dominated the system sharpness, reducing the effective pixel size did not compensate for the loss of resolution. A focal spot of 0.3 mm and pixel sizes of 50, 100, and 150 microns showed an

improvement in resolution for lower frequencies but not for higher frequencies suggesting a task dependent tradeoff for this combination (i.e., depending on the characteristics of the features that need to be imaged, different parameters may be optimal). A 0.3 mm focal spot with a 200 micron pixel size showed an improved MTF for all magnification values although there was an optimum magnification. Magnification with a 0.1 mm focal spot resulted in improved MTF out to very high frequencies regardless of pixel size; specifically for large pixel sizes as the resolution of systems with large pixel sizes and small focal spots were dominated by the pixel size. Magnification in such systems resulted in a smaller effective pixel size thus increasing the overall system resolution.

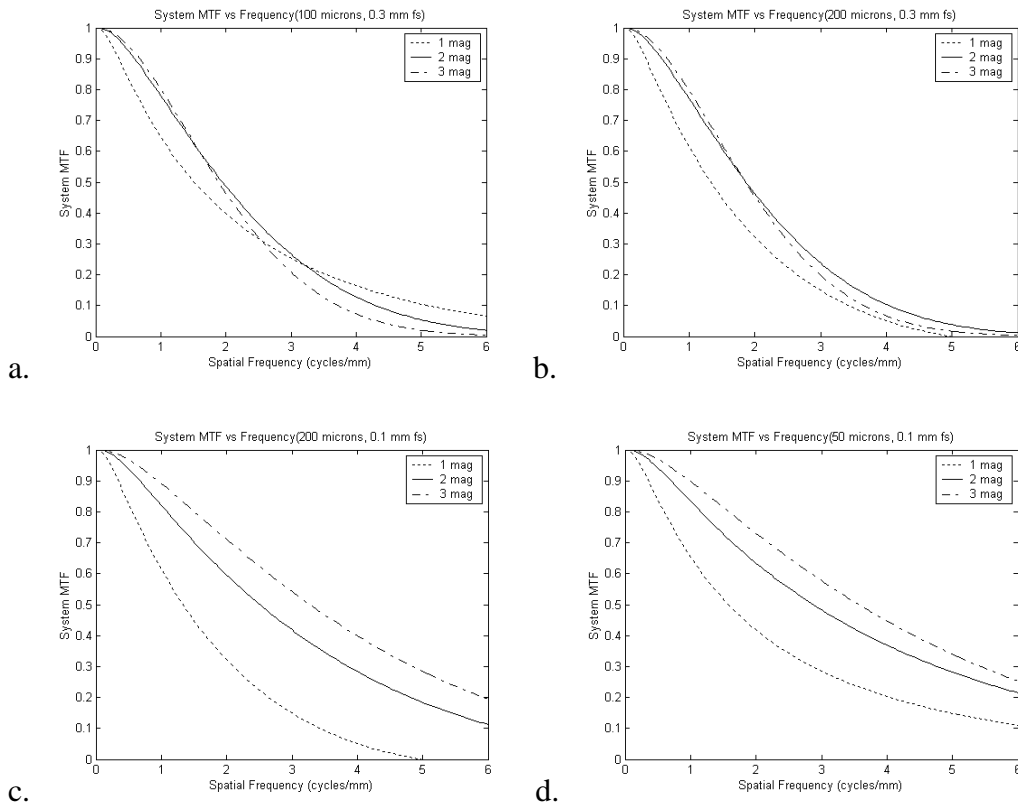


Figure 2.1: System MTF as a function of frequency for three magnifications. a. 100 micron pixel and 0.3 mm focal spot. b. 200 micron pixel, and 0.3 mm focal spot. c. 200 micron pixel and 0.1 mm focal spot. d. 50 micron pixel and 0.1 mm focal spot.

The geometric sharpness was used as an overall figure of merit for spatial resolution averaging across frequencies. Figure 2.2 provides a composite graphic for identifying the optimum magnification as a tradeoff between pixel size and focal spot size. Note the shape of the curves differ for each focal spot size indicating that the maximum benefit from magnification varies as a function of focal spot and pixel size. If focal spot blur does not dominate the spatial resolution (0.1 mm focal spot), magnification provides improvement for all pixel sizes. As focal spot blur begins to dominate spatial resolution (0.3 mm focal spot), the improvement from magnification reaches a maximum in the range of 1.3-1.5. For 0.6 mm focal spot, the focal spot blur dominates the spatial resolution of the system such that magnification provides minimal improvement between 1.1-1.2.

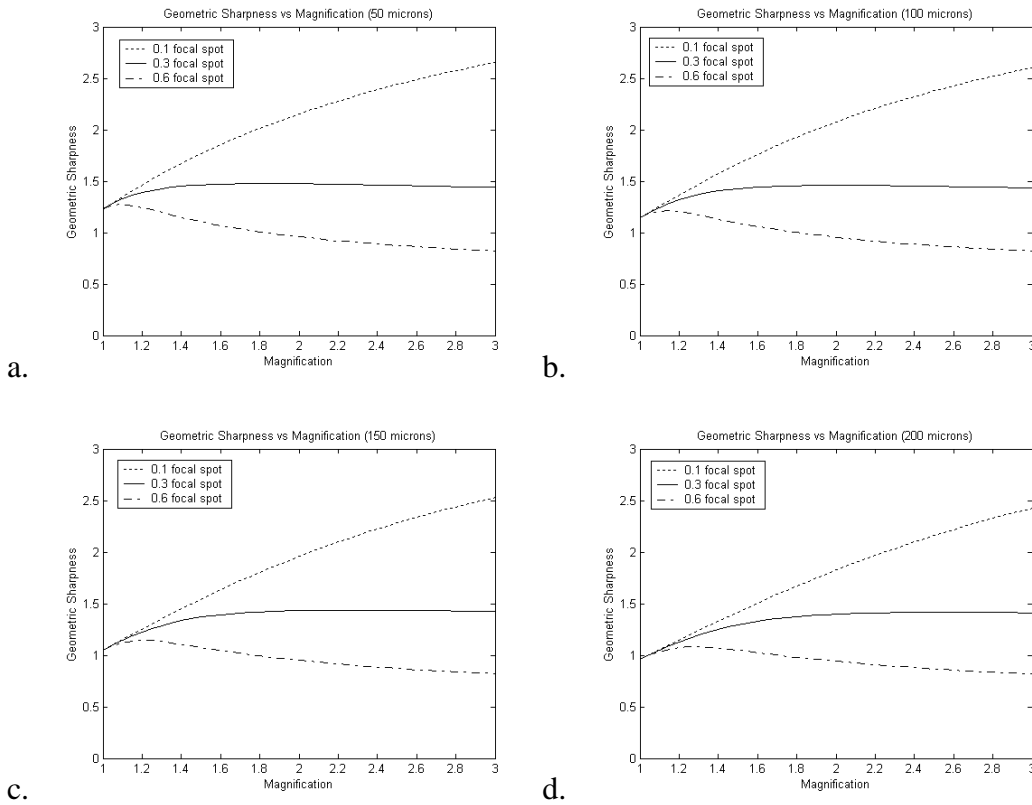


Figure 2.2: Geometric sharpness as a function of magnification for three focal spot widths and four pixel sizes.

As an implicit assumption of this study, the MTF did not change with beam quality and thus the results shown are representative of all the radiographic imaging applications considered in this study.

2.3.2 Effects of Magnification on NPS

Figure 2.3 shows that NNPS decreased with increased magnification for lower frequencies primarily due to the $1/m^2$ factor used to estimate the NNPS in the object plane. The magnification factor can be seen on the y-axis in the difference of the NNPS(0) points which are orders of magnitude apart.

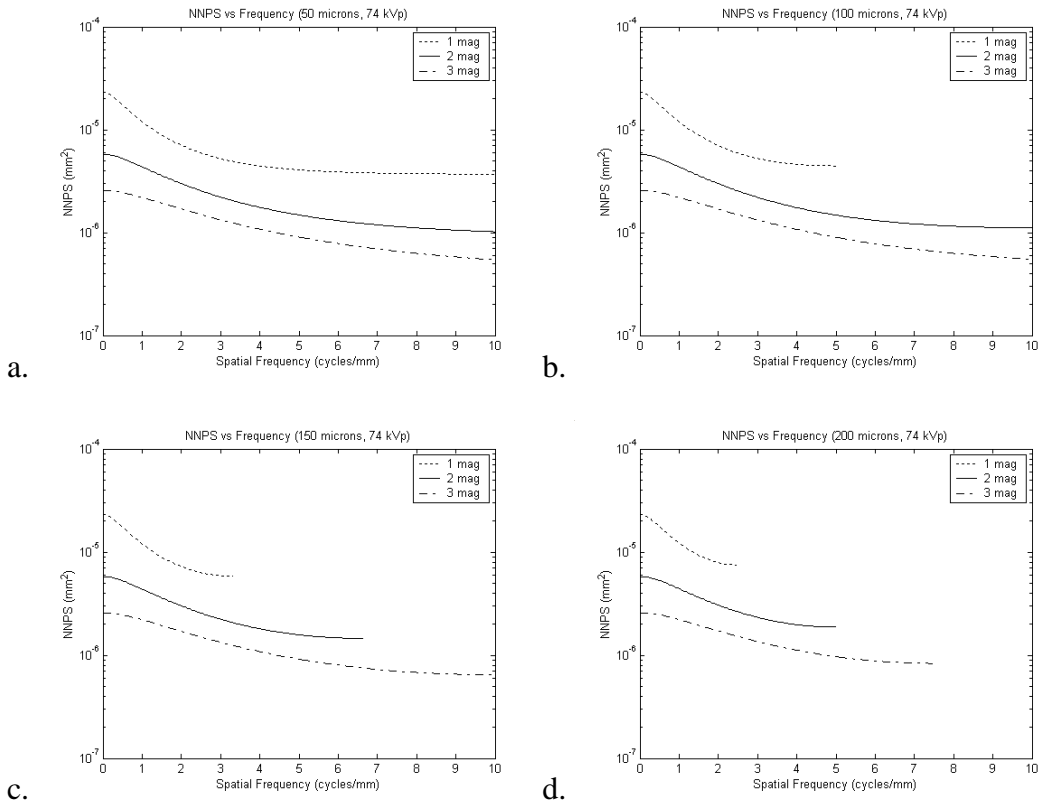


Figure 2.3: Semilog plot of NNPS as a function of frequency for three magnifications and four pixel sizes for 74 kVp.

Magnification also increases the cutoff frequency as shown in Figure 2.3. Notice the aliasing at higher frequencies, evident by the curves beginning to curve upwards in the vicinity of the cutoff frequency. Furthermore, for smaller pixel sizes, the NNPS is higher at higher frequencies. This effect is a result of magnification. Since magnification decreases effective pixel size in the object plane, the frequency shift parallels an improvement in resolution. Improved spatial resolution means less blurring which results in increased noise.

The results shown in Figure 2.3 at 74 kVp are representative of NNPS figures at other techniques which show similar magnification dependencies.

2.3.3 Effects of Magnification on DQE

Figure 2.4 reports the effects of geometric magnification on the DQE for the combinations of parameters previously defined. Results match experimental results of Samei et. al. For small focal spot sizes (0.1 mm), magnification improves the DQE across all frequencies. A noticeable improvement occurs at higher frequencies since magnification shifts the cutoff frequency. For mid-range focal spot sizes (0.3 mm), the effect of magnification is varied. Magnification improves the DQE for larger pixel sizes (150 and 200 microns) but only marginally at lower frequencies for smaller pixel sizes (50 and 100 microns). Also of note is that a crossover point occurs for 0.3 mm focal spot size. For large focal spot sizes (0.6 mm), magnification provides no improvement in the DQE as larger focal spot sizes introduce system blurring.

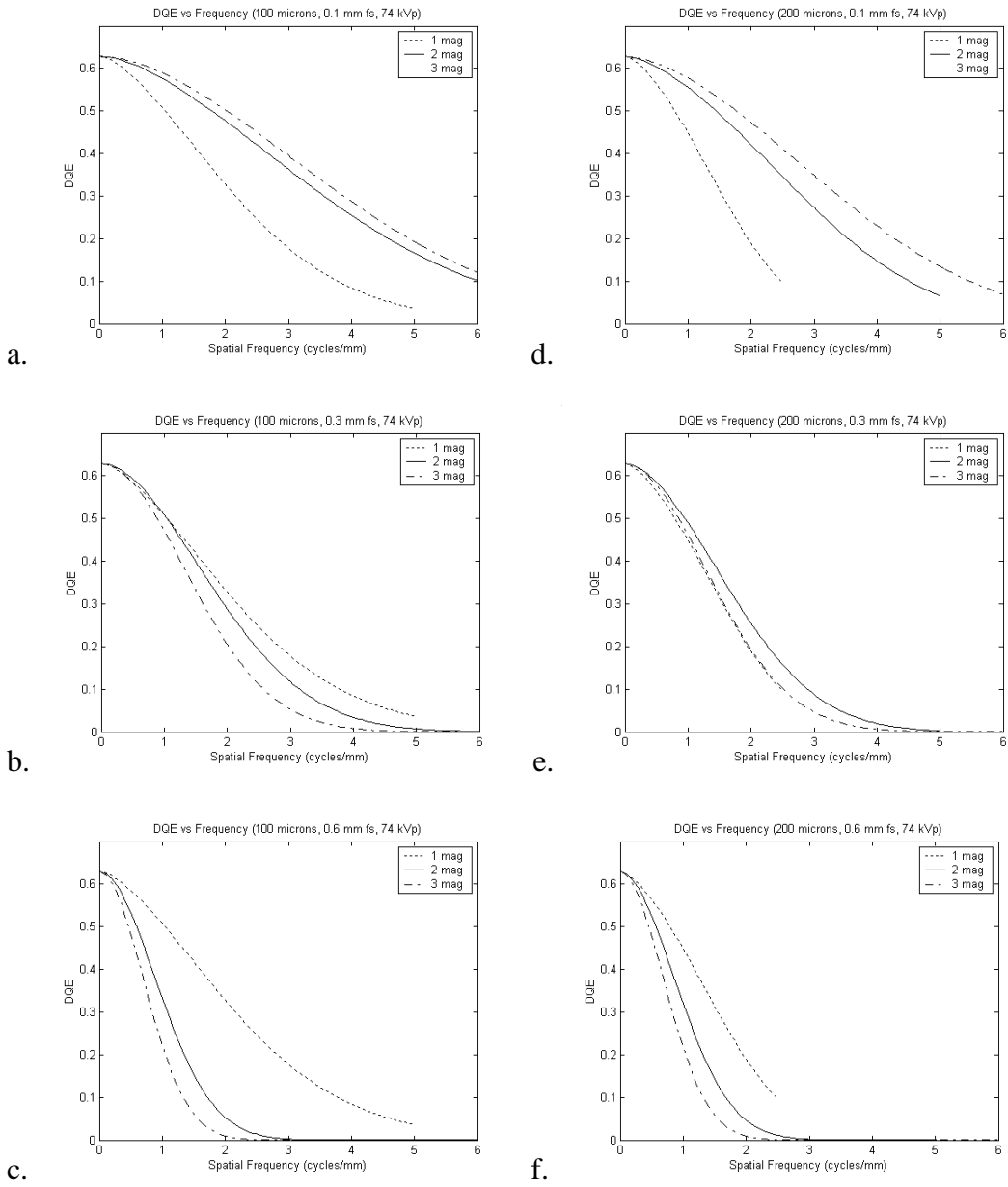


Figure 2.4: Plots of the DQE as a function of frequency for 74 kVp, three magnifications and two pixel sizes, 100 micron (a., b., c.) and 200 micron (d., e., f.).

Figure 2.5 shows the eDQE results. Since the eDQE accounts for scatter in the system, the eDQE values are lower than the DQE values. Magnification and larger SID values improve the eDQE since magnification introduces an air gap which reduces

scatter. The scatter reduction and thus the eDQE improves for the same magnification when a larger SID is used. The magnification shows an optimum value around 1.5.

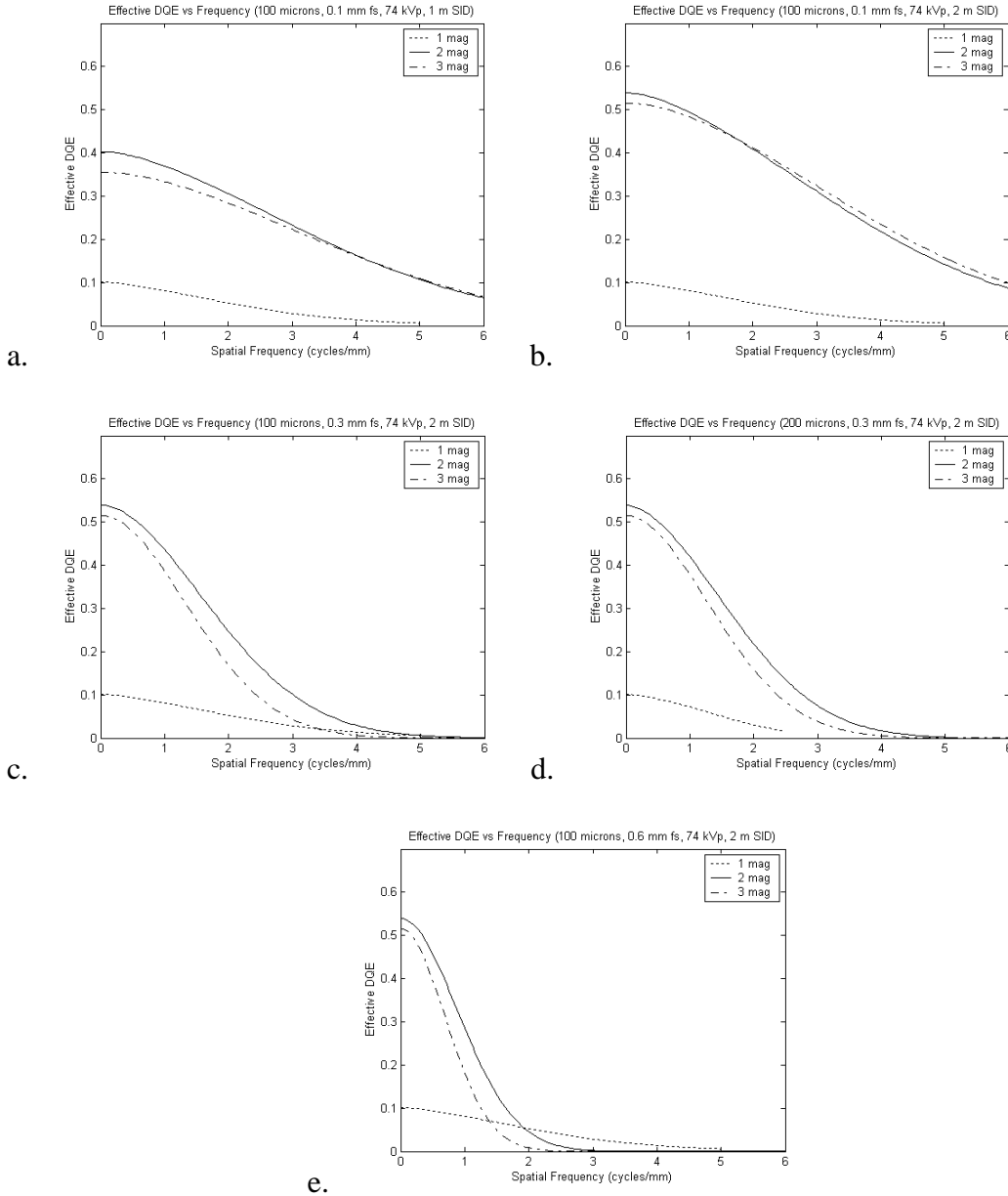


Figure 2.5: DQE_{eff} as a function of frequency for 74 kVp. a. shows the results for SID of 1 m and b. for SID of 2 m for 100 micron pixel and 0.1 mm focal spot. c. 100 micron pixel and d. 200 micron pixel for 0.3 mm focal spot and SID of 2 m. e. shows 100 micron pixel, 0.6 mm focal spot and SID of 2 m.

While the absolute DQE and eDQE values change with kVp and thickness, the results show generally similar dependencies for other applications, as evident in representative results of Figure 2.6.

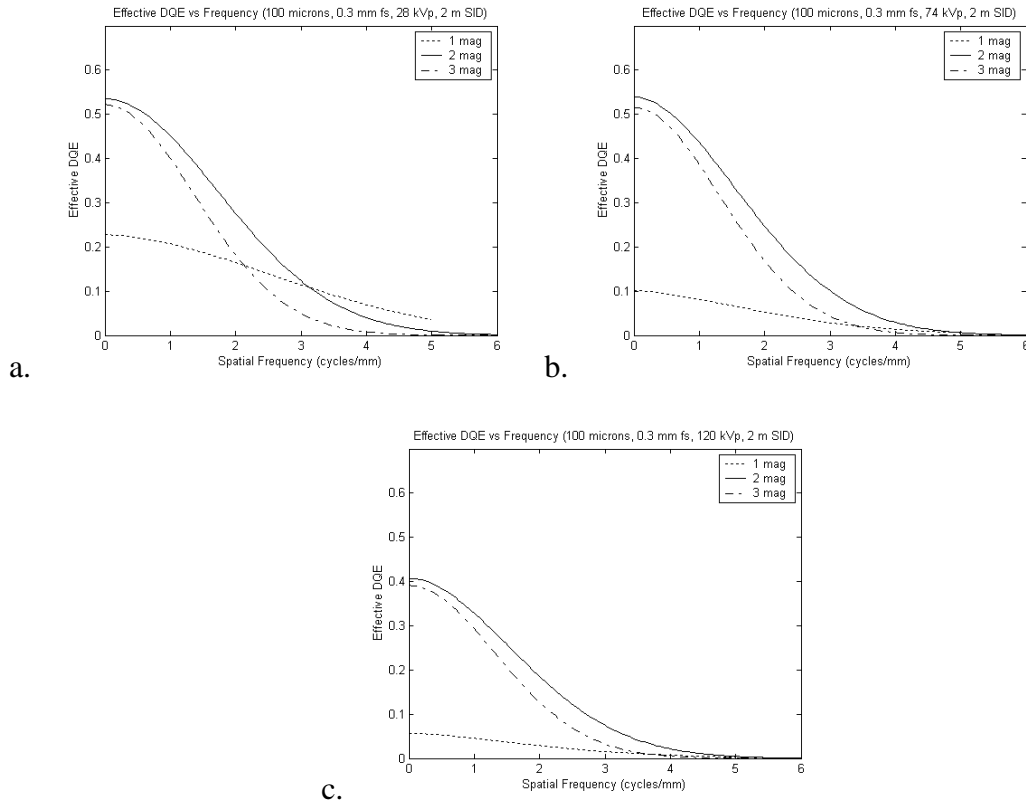


Figure 2.6: DQE_{eff} as a function of frequency for a 100 micron pixel, 0.3 mm focal spot, and 2 m SID. a. mammography (28 kVp). b. general radiography (74 kVp). c. chest radiography (120 kVp).

2.3.4 Effects of Magnification on Observer Model

Figure 2.7 shows the F metric results for a designer nodule of 1 mm. Figure 2.8 is a plot of the peak magnification value obtained in the F metric graphs for all three applications studied. Figure 2.9 plots the improvement observed with magnification as $F_{\text{opt}}/F_{1.1}$ where F_{opt} is the value of F at the optimal magnification and $F_{1.1}$ is the value of F with magnification of 1.1 for all three applications. The peak magnification varies

between 1.45 and 2.1 depending on focal spot, pixel size, SID and application. In general, a smaller focal spot results in a higher optimum magnification. However, for a given focal spot size, the optimum magnification is constant for an SID of 1 m and higher x-ray energies (74 kVp and 120 kVp). For lower x-ray energies (28 kVp), and an SID of 1 m, the peak magnification for a given focal spot only varies for larger pixel sizes.

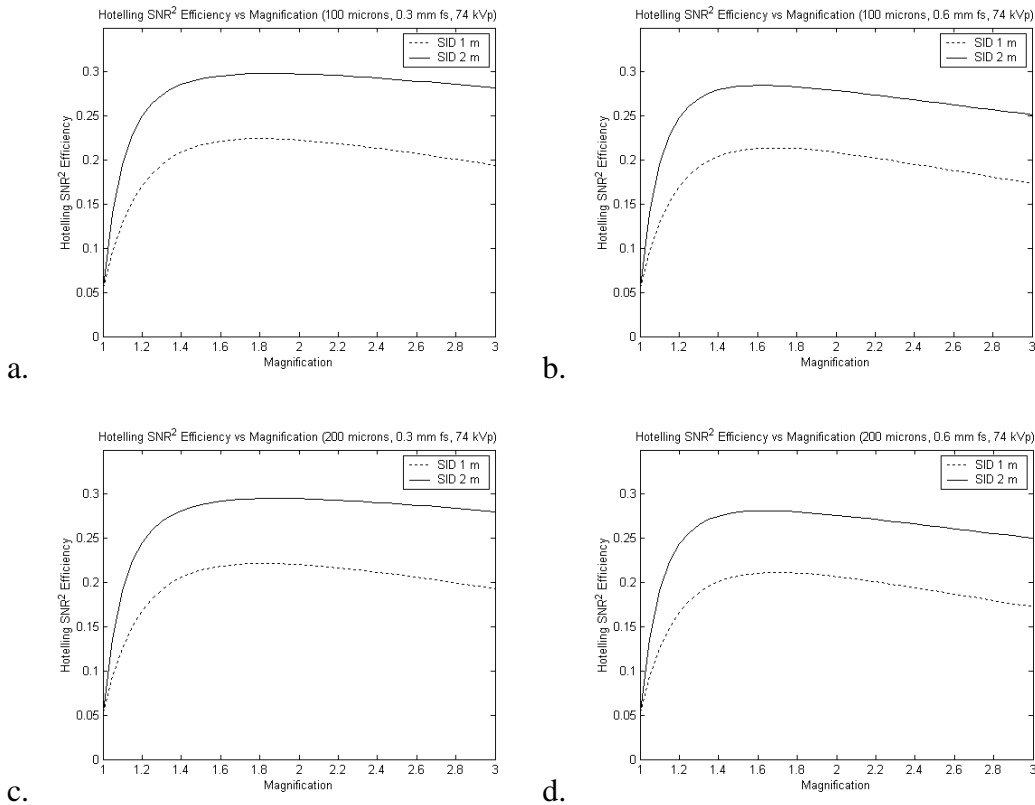


Figure 2.7: Plots of Hotelling SNR² efficiency for a 1 mm nodule and SID of 1 m and 2 m. a. 100 micron pixel and 0.3 mm focal spot. b. 100 micron pixel and 0.6 mm focal spot. c. 200 micron pixel and 0.3 mm focal spot. d. 200 micron pixel and 0.6 mm focal spot.

Optimal geometry improves the Hotelling SNR² efficiency from approximately 1.15 times to 1.95 times depending on the focal spot size, pixel size, SID, and x-ray energy. For all applications studied, magnification provided greater F improvement for a 2 m SID than a 1m SID. For mammography, F improved from approximately 1.15 times

to 1.35 times. For general radiography (and mammotomography), optimal geometry improved F by approximately 1.45 - 1.8 times while for chest radiography, F improved from approximately 1.5 - 1.95 times. For all applications studied, the most improvement was seen to occur for a 50 micron pixel, 0.1 mm focal spot, and 2 m SID.

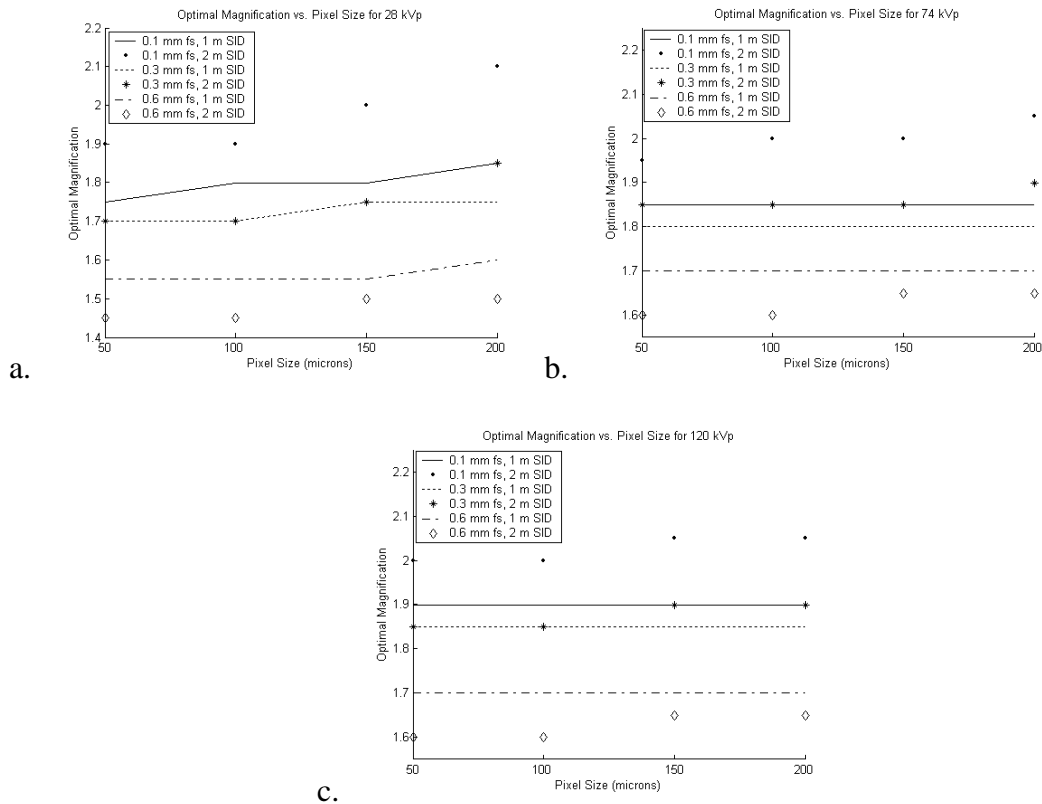


Figure 2.8: Plots of optimal magnification vs. pixel size for three focal spots and two SIDs. a. mammothography (28 kVp). b. general radiography (74 kVp). d. chest radiography (120 kVp).

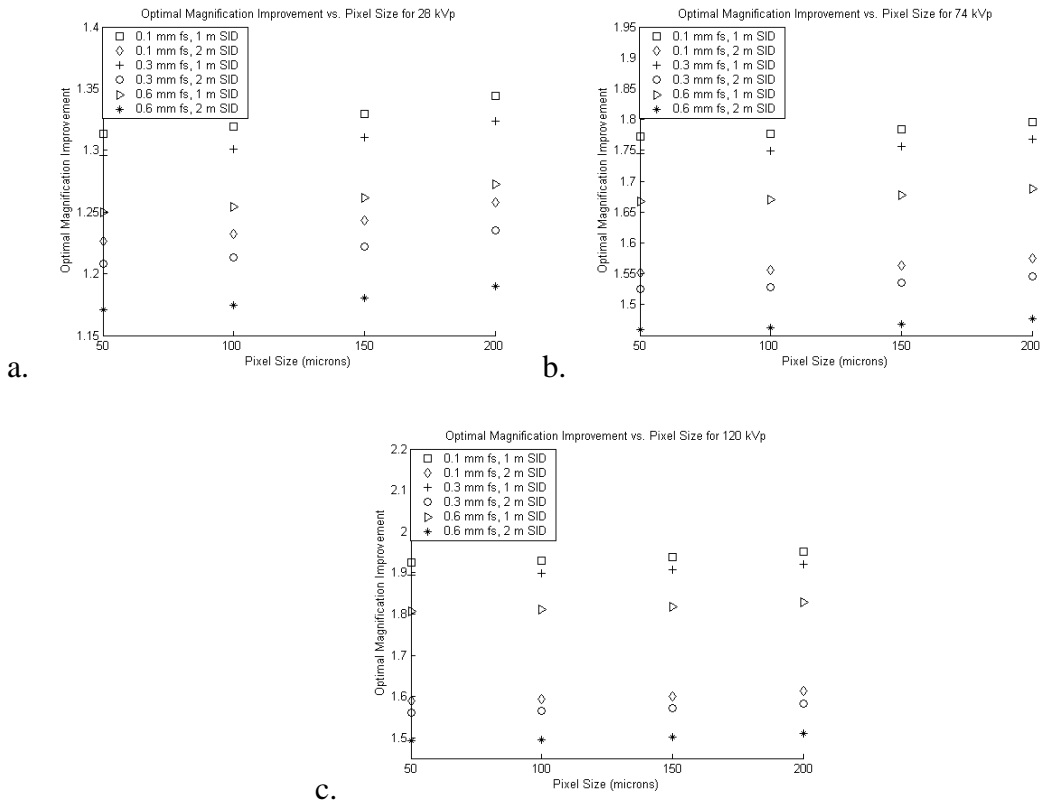


Figure 2.9: Plots of optimal magnification improvement (in terms of SNR^2) vs. pixel size for three focal spots. a. mammography (28 kVp). b. general radiography (74 kVp). c. chest radiography (120 kVp).

2.4 DISCUSSION

The last decade has seen the improvement of imaging technology by the incorporation of flat panel detectors in imaging systems. However, geometry of image acquisition has not been adequately optimized to take advantage of improved characteristics of flat panel detectors. In this work, the effects of geometric magnification have been examined theoretically in terms of the tradeoffs between resolution, noise, and scatter when imaging with flat panel detectors. Improvements from magnification were shown by studying how parameters such as pixel size, focal spot width, scatter rejection, and SID affect the MTF, NPS, and DQE. The model was applied

to three specific applications, mammography, general radiography (also applicable to mammatomography[79]), and chest radiography. Although similar to the study performed by Shaw, et. al.,[124] the goal of this work was to develop a general model for flat panel detectors that can be applied to a wider range of radiographic applications while accounting for scatter rejection.

In general, geometric magnification increased the cutoff frequency of the system. The MTF was seen to improve with magnification for lower frequencies but a crossover point occurred for most geometries, where the focal spot blurring became more dominant. The improvement in the MTF was particularly noteworthy for systems with larger pixel sizes and smaller focal spot widths since the effective pixel size in the object plane was reduced by magnification, thus reducing the overall resolution of the system.

The noise in the system was also seen to diminish with magnification. The NPS increased slightly with improved resolution. Higher magnification reduced noise aliasing leading to reduced noise at high spatial frequencies.

In general, the DQE results show little improvement with magnification. However, accounting for scatter rejection led to an improvement in the effective DQE of the system, eDQE, toward an optimum magnification. The effective DQE would be expected to increase with increased scatter rejection; however, as reported by Sorensen and Flock,[132] a reverse trend occurs between magnification of 1.5 and 2. Sorensen and Flock surmised the trend was due to the effective scatter point source becoming closer to the x-ray source as the object was moved closer to the source. Thus, there was actually a decrease in scatter rejection for higher magnifications (or larger air gaps).

The results of the study indicate that eDQE is improved with magnification which indicates that exposure can be reduced with magnification without compromising image quality. As exposure and dose in x-ray imaging procedures are generally correlated (though not linearly), the findings suggest that a reduction of dose is feasible when magnification imaging is employed without a loss of image quality.

The Hotelling SNR^2 efficiency improved with optimal magnification, but results varied depending on the parameters used. Comparison of the F value at the optimal magnification and the F value at magnification of 1.1 shows that the optimal magnification can improve image quality by as much as 1.95 times. Different applications demonstrate different optimal parameters which if employed can improve image quality.

The optimum magnification varied depending upon the focal spot size, pixel size, x-ray energy, and SID. For all applications, large focal spots did not benefit from increased scatter rejection (larger SID). For a mid-range focal spot size, the benefits of increasing the SID varied depending on the application (x-ray energy). All applications benefited from increased scatter rejection (larger SID) when the focal spot size was small. Furthermore, larger pixel sizes generally exhibited higher optimum magnification values.

Increased magnification has three important practical implications. First, increased magnification requires an increase in the size of the detector to accommodate the magnified field-of-view. Image receptors have conventionally been made in sizes corresponding to the body part being imaged. Magnified imaging requires a change in that paradigm. Secondly, a small focal spot size reduces the flux capability of the source which makes magnification beneficial. Consequently, the receptor may be required to be

operational at higher sensitivities and lower instrumentation noise levels to accommodate lower detector exposures. Therefore, a flat panel detector having increased sensitivity provides advantages when used with magnification. Finally, the size of the acquired image will be magnified. This would require display software functionality to enable “true-size” display of the images. We believe the current state of the detector and display technologies can readily accommodate these implications enabling the advantages of magnified x-ray imaging to be realized.

Future directions for this study include examining the effects of different phosphor thicknesses as well as direct detection flat panel imagers. In addition, the frequency component of the scattered radiation was limited to the DC term as the first approximation; future studies could examine all frequency components. Furthermore, the tissue thickness was assumed to be uniform which is generally not the case in clinical practice and can be examined in future studies.

2.5 CONCLUSION

Geometric magnification does take advantage of increased sensitivity of flat panel detectors and should be more carefully considered for optimizing imaging systems. Our results show that geometrical magnification can improve image quality by as much as 1.95 times assuming that the detector can be operated in a quantum limited range. The particular task should be considered for such optimization and the tradeoffs examined to assure that the optimum magnification is achieved to take advantage of the improvements offered from geometric magnification.

CHAPTER 3

Physical evaluation of a high frame rate, extended dynamic range flat panel detector for real-time cone beam computed tomography applications

3.1 INTRODUCTION

Flat panel detectors with clinical applications have become available in areas such as general radiography[49], fluoroscopy[133], mammography[4], cardiology[47] and computed tomography.[31] Flat panel detectors have demonstrated promising advantages in the areas of acquisition time, clinical throughput, improved DQE, linear response, dynamic range, size and flexibility. The focus of applications for flat panel detectors has primarily been in replacing existing technology. However, new applications are now being considered. The size and flexibility of flat panel detectors combined with increased frame rates and extended dynamic range will allow for future technologies including computed tomography angiography. The purpose of this study was to characterize a high frame rate, extended dynamic range prototype flat panel detector by examining the image quality parameters in terms of linearity, MTF, NPS, DQE, and lag.

3.2 METHODS

Data for this study was taken using an amorphous silicon indirect (CsI) flat panel detector manufactured by Varian Medical Systems, Inc. The detector used was a prototype from the 4030CB series of detectors and was specifically designed to perform

at high frame rates with extended dynamic range. The pixel size of the detector was 194 μm with an active matrix size of 2048x1536. Within a central region of 2048x64, binning of 4x4 was used to achieve faster frame rates for the study resulting in an effective pixel size of 776 μm and an active matrix size of 512x16. Exposures of 2.5 seconds were taken using the RQA5[56] technique at 78 kVp with 21 mm added Al, resulting in sequences obtained using a Bitflow RUN-PCI-12-M frame grabber. The sequences were used to extract individual frames for measurement. Frame rates of 100, 500 and 750 frames per second (fps) were used together with exposures in the range of 0.001 to 0.289 mR per frame. Before acquisition, the flat panel detector was allowed sufficient time to reach thermal equilibrium.

The flat panel detector was calibrated according to directions from the manufacturer. For each frame rate, a series of 128 flat-field images were obtained together with a series of 128 dark current images. These images were combined using a histogram technique to determine the variation of response for each pixel. The calibration files were comprised from this response, and applied real-time on a frame-by-frame basis during acquisition. Dark current calibration was performed before each acquisition. Between each acquisition, a time delay was applied to insure that lag from previous acquisitions would not affect the current acquisition.

Exposures were measured with a calibrated ionization chamber placed halfway between the focal spot and the detector. Placement of the chamber was such that scattered radiation from the source did not affect the measurement. The inverse square law was then used to determine the exposure at the surface of the flat panel detector.

The exposure value determined from the inverse square law was scaled based on frame rate and active exposure time per frame as

$$E = \left(\frac{E_s}{r * T} \right) * \left(\frac{\frac{1}{r} - t_d}{\frac{1}{r}} \right), \quad (3.1)$$

where E_s is the exposure at the surface of the flat panel detector as measured and determined from the inverse square law, r is the frame rate, T is the total exposure time for the sequence, and t_d is the time length during each frame acquisition during which the flat panel detector was insensitive. T was 2.5 seconds for all acquisitions, and t_d was set to 41.65625 μ s per manufacturer.

3.2.1 Linearity

Linearity was characterized at the RQA5 technique using a flat-field technique. Data sequences of 2.5 seconds were obtained for frame rates of 100, 500 and 750 fps and exposures including low, mid and high ranges. The mean pixel count per frame was determined for a 256x12 region of interest (ROI) and then averaged for all frames to obtain a plot of average pixel count versus exposure.

3.2.2 Modulation transfer function

The presampled modulation transfer function (MTF) was measured using an edge technique as described by Samei, et. al.[109] The basic protocol involved the placement of an opaque edge directly on the detector at a slight angle to the horizontal scanning direction of the flat panel detector. The edge used was composed of a 2 mm thick, 5x10 cm² W slab. A previous study[118] determined the optimal algorithm for calculating the MTF from data acquired using an edge technique. The angle of the edge was determined

from a Radon transformation. The edge spread function (ESF) was determined by reprojecting the 2D image data into pixel bins of 0.5 pixel width for a 10.6 mm region on either side of the edge. The line spread function (LSF) was determined by smoothing and differentiation using a central difference algorithm. The normalized Fourier transformation of the LSF produced the presampled MTF.

The MTF measurements were made for frame rates of 100, 500 and 750 fps in sequences of 2.5 seconds using the IEC RQA5 technique at a tube potential of 250 mA. The presampled MTF was calculated for each frame in the sequence and then averaged to obtain the reported presampled MTF.

3.2.3 Noise power spectrum

The normalized noise power spectrum (NNPS) was determined by using a routine from a previous study.[118] Measurements were obtained from flat-field images taken from sequences of 2.5 second exposures using the IEC-defined RQA5 radiographic technique and tube currents of 10 mA, 20 mA, 40 mA, 80 mA, 160 mA and 250 mA. Each frame of the sequence was divided into three subarrays of size 128x128. The data from each subarray were corrected for nonuniformity, scaled and Fourier transformed resulting in the NNPS. The NNPS for each subarray was combined to obtain an average NNPS for each frame. The NNPS from each frame was then combined to obtain the average NNPS for a particular frame rate.

The average NNPS per frame was then corrected for lag using the first frame lag formulation developed by Granfors and Aufrichtig[48]

$$lag_1 = \frac{S_{final} - S_{after}}{S_{final} - S_{initial}}, \quad (3.2)$$

where S_{initial} and S_{final} are the signal levels at equilibrium with and without exposure and S_{after} is the signal in the first frame after exposure has ceased. The first frame lag was used to correct the NNPS in the following manner,

$$NNPS_{\text{lag}} = \frac{NNPS}{(1 - \text{lag}_1)^2}, \quad (3.3)$$

where NNPS is the measured NNPS described previously.

3.2.4 Detective quantum efficiency

The detective quantum efficiency (DQE) was calculated using the form[125]

$$DQE(f) = \frac{MTF(f)^2}{NNPS_{\text{lag}}(f) * E * q}, \quad (3.4)$$

where E is exposure, q is the ideal SNR^2 per exposure, $MTF(f)$ is the modulation transfer function described previously, and $NNPS_{\text{lag}}$ is the NNPS with lag correction described in the previous section.

3.2.5 Temporal properties

The temporal lag of the detector occurs due to inefficiency in charge collection between different frames¹¹. The temporal lag may be defined in terms of n th-frame lag, Lag_n given by the ratio of the image signal in frame n , Sig_n to that in the frame immediately following a radiographic exposure (frame zero):

$$Lag_n = \frac{Sig_n}{Sig_0}, \quad (3.5)$$

We characterized the lag of the detector by its temporal MTF. Therefore, the information about Lag_1 was contained in the MTF at the Nyquist frequency whereas information about longer-term image retention, i.e. Lag_n for large values of n , was reflected in the

MTF at very low frequencies. Two methods were used to determine the MTF. In the first method, the detector was exposed to a 500 ms impulse of x-rays. In the second method, the detector was exposed for a longer period of 6.4 seconds. The detector was read-out for approximately 20 secs in both cases. The falling edge was extracted from the resultant profiles combining data from multiple pixels. Its average profile was differentiated using the central-difference algorithm to generate the falling LSF. The LSF was flipped about its peak value to make it symmetric. This was done to exclude that part of the LSF which may have been affected by the temporal behavior of the x-ray tube and the generator, thus minimizing that impact. Fourier transform techniques were then used on the resultant LSF to determine the MTF using techniques similar to those outlined earlier. For data acquisition, an effective frame rate of 95.59 was used, corresponding to a Nyquist frequency of 47.79 fps.

3.3 RESULTS

3.3.1 Linearity

Figure 3.1 shows the response of the flat panel detector using a linear fit with a zero intercept constraint and R^2 value of 0.9998. Figure 3.1a. shows the linear response for all exposures while Figure 3.1b. is a zoomed view of the lower exposures. The results indicate that the detector is linear across exposures with data corresponding to different frame rates lining up well according to their exposure values.

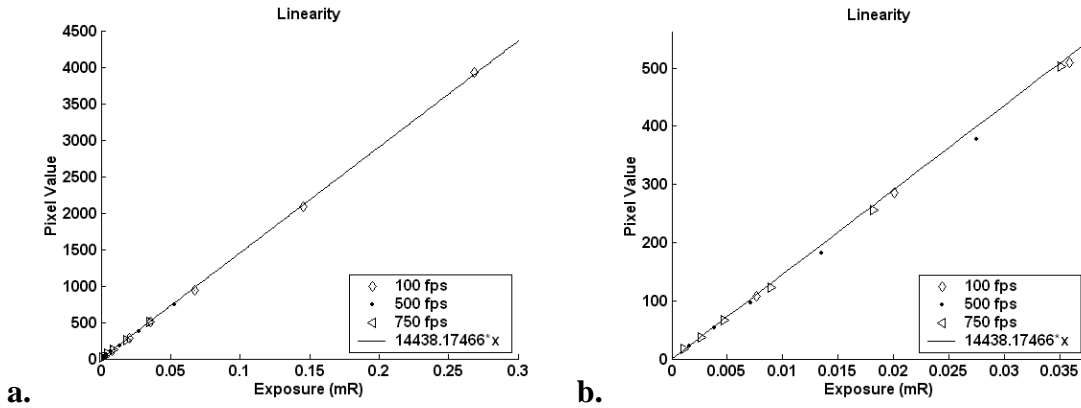


Figure 3.1: Linearity as a function of exposure (mR) for all exposures (a) and for lower exposures (b).

3.3.2 Modulation transfer function

Figure 3.2 shows the results for the presampled spatial MTF for frame rates 100, 500, and 750 fps as obtained using the edge technique described in an earlier section.

The MTF is shown to be independent of frame rate yielding a 0.1 value at 0.92 cycles/mm

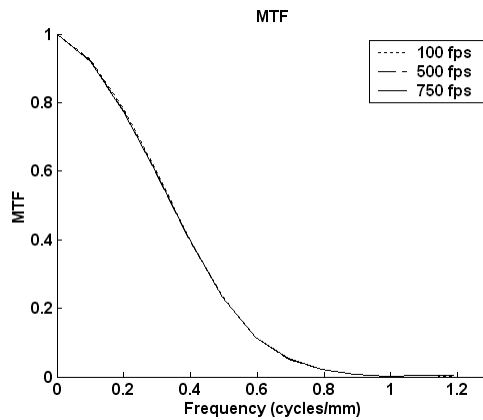


Figure 3.2: Presampled spatial MTF as a function of frequency for frame rates 100, 500, and 750.

3.3.3 Noise power spectrum

Figure 3.3 displays the $NNPS_{lag}$ results for each frame rate and range of exposures. The NNPS was only measured in the horizontal direction as the size of the active region did not provide enough data for measurement in the vertical direction. At a constant mA, as the frame rate is increased, the period of time that each frame is exposed decreases. This is demonstrated in the $NNPS_{lag}$ results since the $NNPS_{lag}$ improves as a function of frame rate. Thus, the increased frame rate can be viewed as an equivalent decrease in exposure.

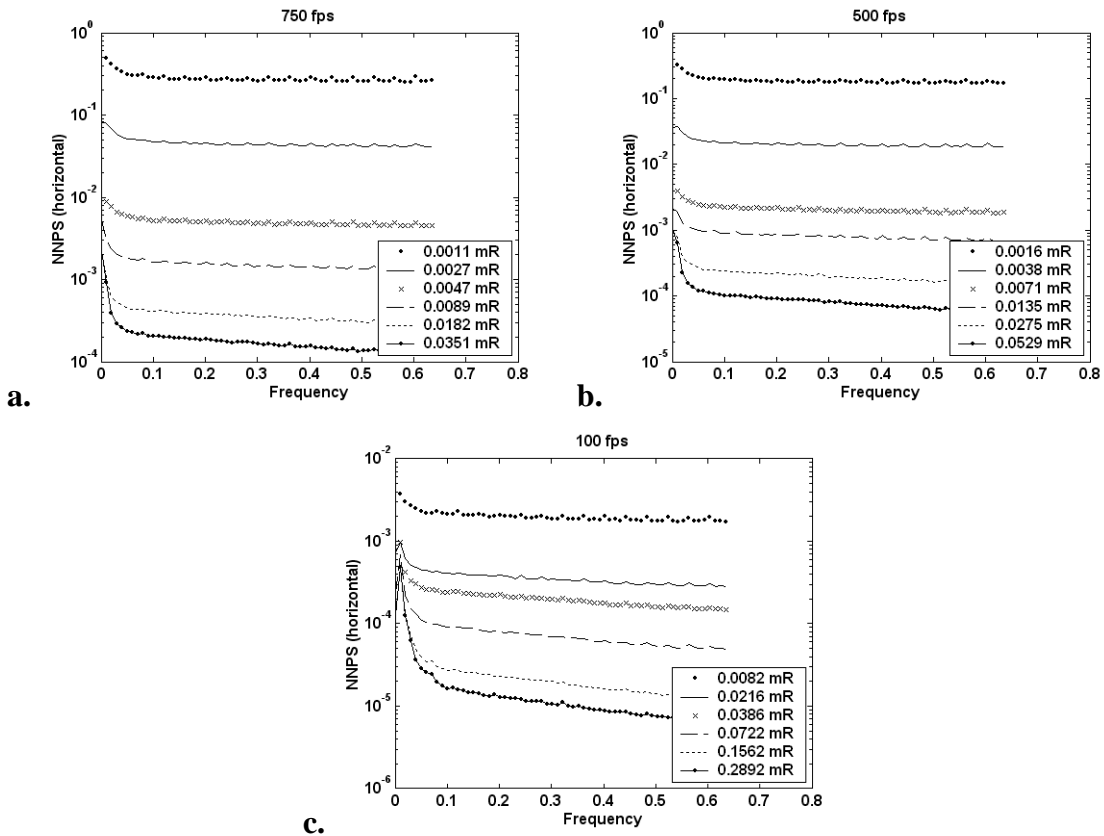


Figure 3.3: $NNPS_{lag}$ in units of mm^2 versus frequency in units of cycles/mm for exposures ranging from 0.001 to 0.289 mR for frame rates 750 fps (a), 500 fps (b), and 100 fps (c).

3.3.4 Detective quantum efficiency

Figure 3.4 shows the results for the DQE calculations for exposures ranging from 0.001 to 0.271 mR using an ideal SNR^2 value of $264626 \text{ \#/mm}^2\text{-mR}$ as per International Electrotechnical Commission (IEC) standard 6220-1[56]². The $\text{DQE}(0)$ values were approximately 0.8, 0.6, 0.4 and 0.22 for exposures of 0.144, 0.065, 0.035, and 0.008 mR per frame. Increasing the frame rate results in a decrease in the equivalent exposure as indicated by the symbols, O, +, and * in the graphs. For example, the maximum exposure for 750 fps is approximately 0.0346 mR as indicated with the O symbol. The $\text{DQE}(0)$ at that exposure is approximately 48% which is consistent for that exposure in the graphs for 500 fps and 100 fps. The DQE increases with increasing exposure and appears to converge to approximately 80% for higher exposures. The results indicate that DQE has an exposure dependence for lower exposures which is likely due to the electronic noise in the system.

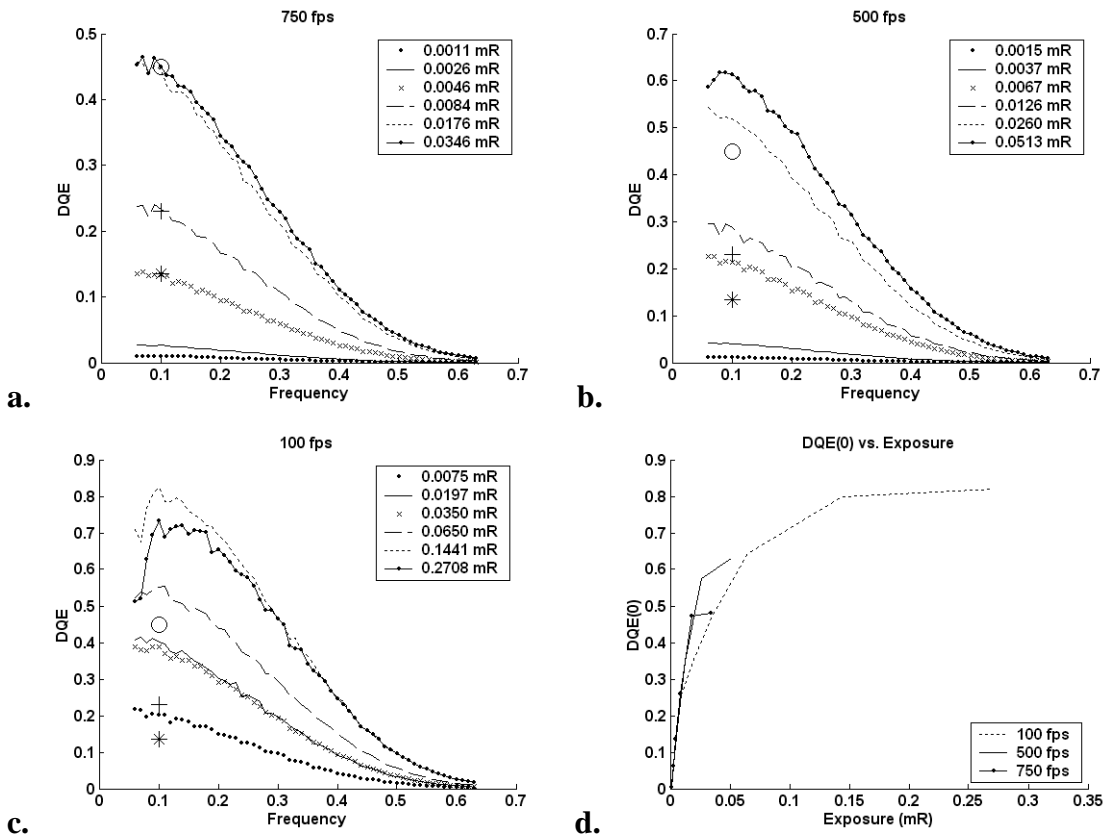


Figure 3.4: DQE versus frequency in units of cycles/mm for exposures ranging between 0.001 and 0.271 mR per frame for frame rates of 750 fps (a), 500 fps (b), and 100 fps (c). Figure d. is a plot of DQE(0) as a function of exposure for frame rates 100, 500 and 750 fps.

3.3.5 Temporal properties

Figure 3.5 (a) shows the variation of image intensity as a function of frame-time in the condition in which the detector was exposed to x-rays for 6.4 secs. Figure 3.5(b) shows the LSF after differentiating the temporal falling edge and making it symmetric about its peak value. Figure 3.6 shows the temporal MTF up to the Nyquist frequency. The data demonstrates a less than perfect MTF ($MTF < 1$) at all frequencies and a notable low frequency drop indicative of a long-term lag. The slight increase close the temporal

Nyquist frequency is most likely due to aliasing inherent in MTF calculation without oversampling.

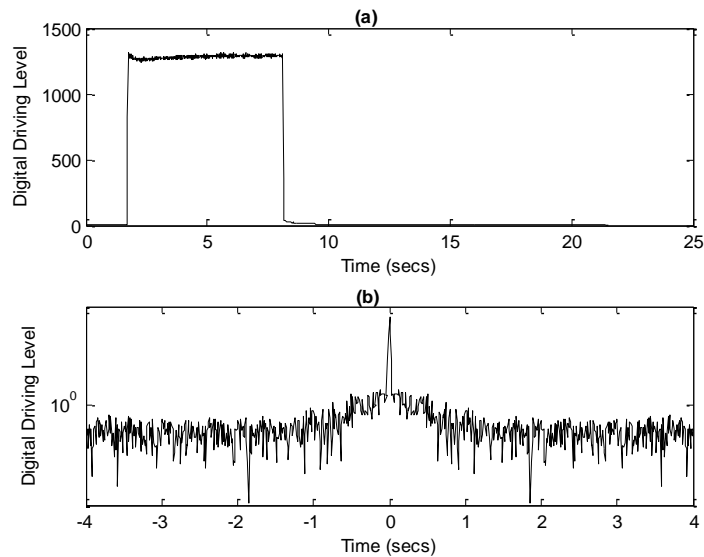


Figure 3.5: (a) Profile of the LSF generated by exposing the detector for a long duration. (b) Profile of falling LSF determined by differentiating the extracted falling edge.

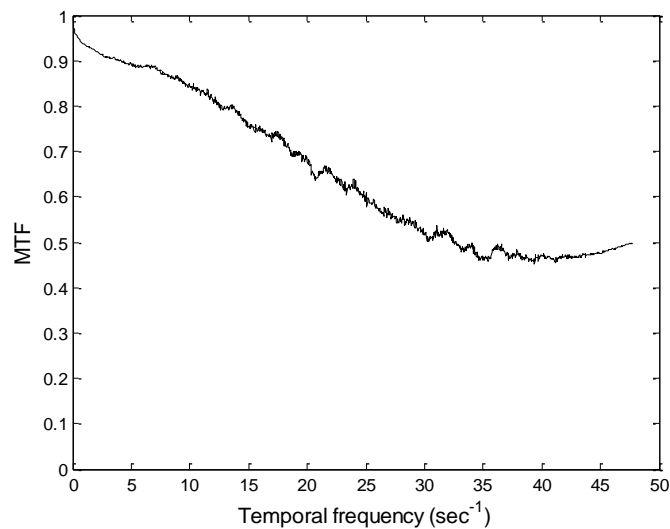


Figure 3.6: The temporal MTF of falling LSF determined by using the long-exposure technique. The MTF was determined by exposing the detector with x-ray for a long duration of time.

3.4 DISCUSSION

While flat-panel systems are becoming common in radiographic applications, the transition to real-time fluoroscopy and CT application has been slow primarily due to increased instrumentation noise considerations at low exposures involved. In this study we evaluate a high frame-rate fluoroscopic panel for potential CT applications. The panel demonstrated excellent spatial resolution response independent of the frame rate. However, as expected, noise was notable at exposures below approximately 0.15 mR/frame, leading to a decrease in the DQE below this limit. The DQE results were consistent across frame rates and only dependent on the exposure per frame.

The first frame lag technique used to calculate $NNPS_{lag}$ is prone to aliasing since exposure is not synchronized with the period of time during which the frame can be exposed. This may result in partially exposed frames and thus it may be difficult to determine exactly the first frame after which exposure has ceased. Using the frame after a partially exposed frame may result in inaccurate determination of the first frame lag affecting the calculation of $NNPS_{lag}$ and thus DQE. Averaging several sequences of data would compensate for this effect.

The temporal MTF describes the transfer of information at various temporal frequencies, thus quantitatively describing the temporal blurring that results from image lag. The temporal MTF indicates low high-frequency response. This indicates the spreading in the response of the detector to an impulse of x-ray exposure to frames immediately following the frame at which the exposure was cut-off, i.e. $Lag_1 > 0$. There is also a steep drop at very low-frequencies. This is largely due to slow decay-component of

lag experienced by the detector i.e. the detector may still be experiencing the effect of the exposure a long time after the exposure was cut-off. This is also sometimes termed as “ghosting”. The temporal MTF of the detector under study indicates that this effect was present until approximately 1 second after the exposure was cut-off. It may be noted that this phenomenon is analogous to a drop in the MTF due to veiling glare in the spatial domain. Although easy, the measurement of the temporal MTF by the method described here has its own drawbacks. The method does not determine the pre-sampled MTF. The Nyquist frequency of the sampling rate was equal to the inherent Nyquist frequency of the detector at the given frame rate. The results are, therefore, prone to errors due to aliasing. Also, the method does not exclude the effect of temporal response of the x-ray tube and the generator although care was taken while truncating the LSF to minimize this effect.

The system configuration parameters, 4x4 binning, and electronic gain available in the prototype flat panel detector used for this study resulted in an flat panel detector that is not very sensitive at low exposures and thus a lower DQE is seen. Improvements in the flat panel detector have been made by the manufacturer since the beginning of this study. These improvements include binning and electronic gain options that would improve the sensitivity of the flat panel detector and thus the DQE.

3.5 CONCLUSION

This study characterized a prototype flat panel detector specifically designed for technologies requiring high frame rates and extended dynamic range. The system is shown to be linear. The MTF is shown to be independent of frame rate. Furthermore, the NNPS and DQE results are consistent with current flat panel detectors. The temporal

MTF indicates both short-term and longer-term image retention between frames; however, a detailed analysis of its relevance to imaging applications was not investigated. The preliminary results indicate that the clinical use of this prototype flat panel detector is feasible.

Future work includes examining the image quality parameters of different binning combinations and different dynamic ranges. Faster frame rates will also be available for study as technology improves. In addition, parameters specific to computed tomography applications will also be investigated.

CHAPTER 4

Effective DQE (eDQE) for monoscopic and stereoscopic chest radiography imaging systems with the incorporation of anatomical noise

4.1 INTRODUCTION

Chest x-ray (CXR) is the most common modality for imaging the lungs; however, anatomical noise results in a high miss rate.[102, 107, 130] Bi-plane correlation imaging (BCI) has been shown to offer improved detection of lung lesions and has been proposed as an alternative to chest radiography; however, the advantages have not been fully qualified.[102, 117] Traditionally the metrics of modulation transfer function (MTF), noise power spectrum (NPS), and detective quantum efficiency (DQE) primarily report a detector response and not the system response under clinical conditions.[17, 57-59, 95, 112-115] Generalized metrics such as the effective DQE (eDQE) have been proposed which incorporate many system performance aspects.[17, 111, 113-116] Measurement of the eDQE requires an application specific phantom to emulate scatter and magnification effects of a clinical condition. Previous studies of the eDQE have used a generalized geometrical chest phantom consisting of acrylic slabs and aluminum separated by an air gap to simulate the lung field.[113, 115] Such phantoms do not include anatomical structures, an ever present element of chest imaging.

Flat panel detectors used in chest radiography systems have been shown to have improved signal-to-noise ratio (SNR) over competing technologies.[6, 21, 38, 49, 127]

This chapter is based on a paper by Sarah Boyce and Ehsan Samei, "Effective DQE (eDQE) for monoscopic and stereoscopic chest radiography imaging systems with the incorporation of anatomical noise", submitted for review, Medical Physics, 2013.

However, clinical imaging systems which employ flat panel detectors have been retrofitted without change to the system geometry which may not take advantage of the improved SNR. Studies have indicated that magnification may provide benefits for the detection performance in chest radiography.[14, 86, 124, 129, 132] However, that advantage has not been substantiated in anatomical backgrounds.

The goal of the current work was to use anthropomorphic chest phantoms in a clinical imaging system to compare single view CXR and BCI with stereoscopic viewing (stereo/BCI) modalities. The phantom provided an approximation of scatter and magnification for an average adult and a large adult by the addition of fat layers. This study further examined two geometries to compare typical clinical geometry where the patient is adjacent to the detector versus a geometry where the center of the patient is placed to achieve approximately 50% magnification. Iso-dose conditions were used to evaluate imaging metrics including effective MTF (eMTF), effective normalized NPS (eNNPS), eDQE, and detectability index.

4.2 MATERIALS AND METHODS

A standard table mounted radiography system previously used in the radiology department at the Duke Medical Center was retrofitted to mount the x-ray tube for horizontal translation.[22] This allowed for acquisition of images at the standard posterior-anterior (PA) iso-centric location as well as angles of ± 3 degrees off iso-center. The source to image distance was 2 meters and no antiscatter grid was used. The focal spot size was 0.6 mm. A 40 x 30 cm flat panel detector with a 14-bit image on a 2048x1536 matrix size and a pixel pitch of 0.194 mm (4030CB, Varian Medical Systems, Inc.) was used for the study. The image data were corrected for gain, offset, and

defective pixels automatically as per manufacturer instructions which produced the raw image data used for the study. The performance of the flat panel detector was evaluated previously.[16]



Figure 4.1: An anthropomorphic chest phantom (left) with realistic lung vessel structures (right).

An anthropomorphic chest phantom seen in Figure 4.1 (Kyoto Kagaku Co.,Ltd) was used for this study. The phantom was used in two size configurations to represent adult and large adult body habitus. To assess the effects of magnification on system performance, the phantoms were imaged with two different geometries. For the first geometry, the phantoms were placed adjacent to the detector cover plate. For the second geometry, the phantoms were placed at a distance to produce approximately 50% magnification from the center of the phantom. Table 4.1 shows the phantom sizes and maximum magnifications from the tube side of the phantom. The phantom width is the measurement from front to back at the ribs. A geometrical chest phantom was used with two sizes for comparison purposes.

Table 4.1: Phantom Size and Magnification Distance

Phantom	Width (cm)	Magnification with Phantom at Receptor Cover Plate	Magnification with Phantom Center at ~50% Magnification
Adult	20	1.12	1.66
Large Adult	27	1.18	1.69
Geometrical	28	1.11	N/A
Large Geometrical	33	1.12	N/A

4.2.1 System Response Function

System linearity was measured using an established procedure with the phantom placed in close proximity to the x-ray tube to account for beam hardening effects.[112, 113, 115] Exposures were measured free-in-air in the lung projected area then inverse square corrected to obtain exposures at the detector plane. A calibrated ionization chamber (MDH Model 1015, 10X5-6 ionization chamber, Radcal, Monrovia, CA) was used to capture exposure values.

4.2.2 Effective Modulation Transfer Function

The resolution of an imaging system is commonly determined using the modulation transfer function (MTF).[90, 103, 104, 118] For this study, the MTF was measured using an opaque edge test device placed at a slight angle to the vertical scan direction with the tube at iso-center. For logistical reasons, the edge was placed 4.5 cm away from the phantom on the tube side. Placement of the edge on the tube side of the

phantom allowed for maximum magnification effects. The edge was placed so that it projected over the lung field. Since the phantom and magnification were included in the measurement, the measurement captures the eMTF for the system. The adult and large adult phantoms were placed at the detector cover plate, and at a distance to establish approximately 50% magnification from the center of the phantom (see Table 4.1). Computation of the eMTF was performed in the object plane using established techniques.[109, 112, 113, 115] The eMTF from three repeat images was averaged to obtain the final result.

4.2.3 Effective Noise Power Spectrum

The noise power spectrum (NPS) provides a quantitative representation of the noise properties of clinical systems.[41, 103, 104, 135] Measurements were taken with the adult and large adult phantoms placed at the detector cover plate and at a distance which provided approximately 50% magnification from the center of the phantom. Using the phantoms in the measurement allows for the determination of the effective normalized NPS (eNNPS) for the clinical system. The nominal dose E_0 used was determined by manufacturer defined flat panel detector target dose recommendations. Beam quality of 120 kVp was used, and images were obtained at two iso-dose settings corresponding to E_0 and $3.2E_0$ for the adult phantom as shown in Table 4.2. The dose remained constant for both geometries studied. Five repeat images were obtained. The eNNPS was calculated in the object plane using an established technique.[27, 40, 113, 115]

Table 4.2: Exposure Condition

Exposure	Incident (mR)	@ receptor (mR)
$\sim E_0$	~ 11.372	~ 3.83
$\sim 3.2E_0$	~ 36.2	~ 12.2

The eNNPS was determined for single view CXR and stereo/BCI modalities with the anthropomorphic phantoms. For comparison, the eNNPS was also determined for the geometrical phantom[113, 115]. The single view CXR eNNPS was determined using the iso-centered PA image as obtained from the clinical imaging system. Consecutive regions of interest (ROIs) sized 128x128 were selected in the left and right lung fields for eNNPS analysis. Figure 4.2(a) provides an example of an ROI used for analysis.

Five nonconsecutive ROIs chosen from the left and right lung field and sized 32x32 were used for analysis of the eNNPS for the stereo/BCI modality. The results were averaged across five repeat images for both oblique angles. For stereo/BCI, the images used for eNNPS analysis were obtained using methods of error propagation in counting statistics for multiple independent measurements assuming the viewer focuses on the plane of the lesion.[62] The stereo/BCI eNNPS was determined by correlating the two oblique views obtained at ± 3 degrees of center. The equation shows how the stereo/BCI image used for the eNNPS calculation was obtained numerically from the image captured by the clinical system,

$$BCI_{ROI} = \frac{\sum_1^n ROI_i^{+3}(j,k) + \sum_1^n ROI_i^{-3}(j,k)}{n} - \frac{(ROI_i^{+3}(j,k) + ROI_i^{-3}(j,k))}{2}, \quad (4.1)$$

where BCI_{ROI} represents the final ROI used for the eNNPS calculation, ROI_i^{+3} and ROI_i^{-3} represent the original ROIs for the oblique views at ± 3 degrees of center, n is the number of images and j,k represent the pixel at position j,k . In the formulation, stereo/BCI was assumed to incorporate noise for the two oblique views as an averaging operator. Figure 4.2(b) shows an example of the resultant image used for eNNPS analysis.

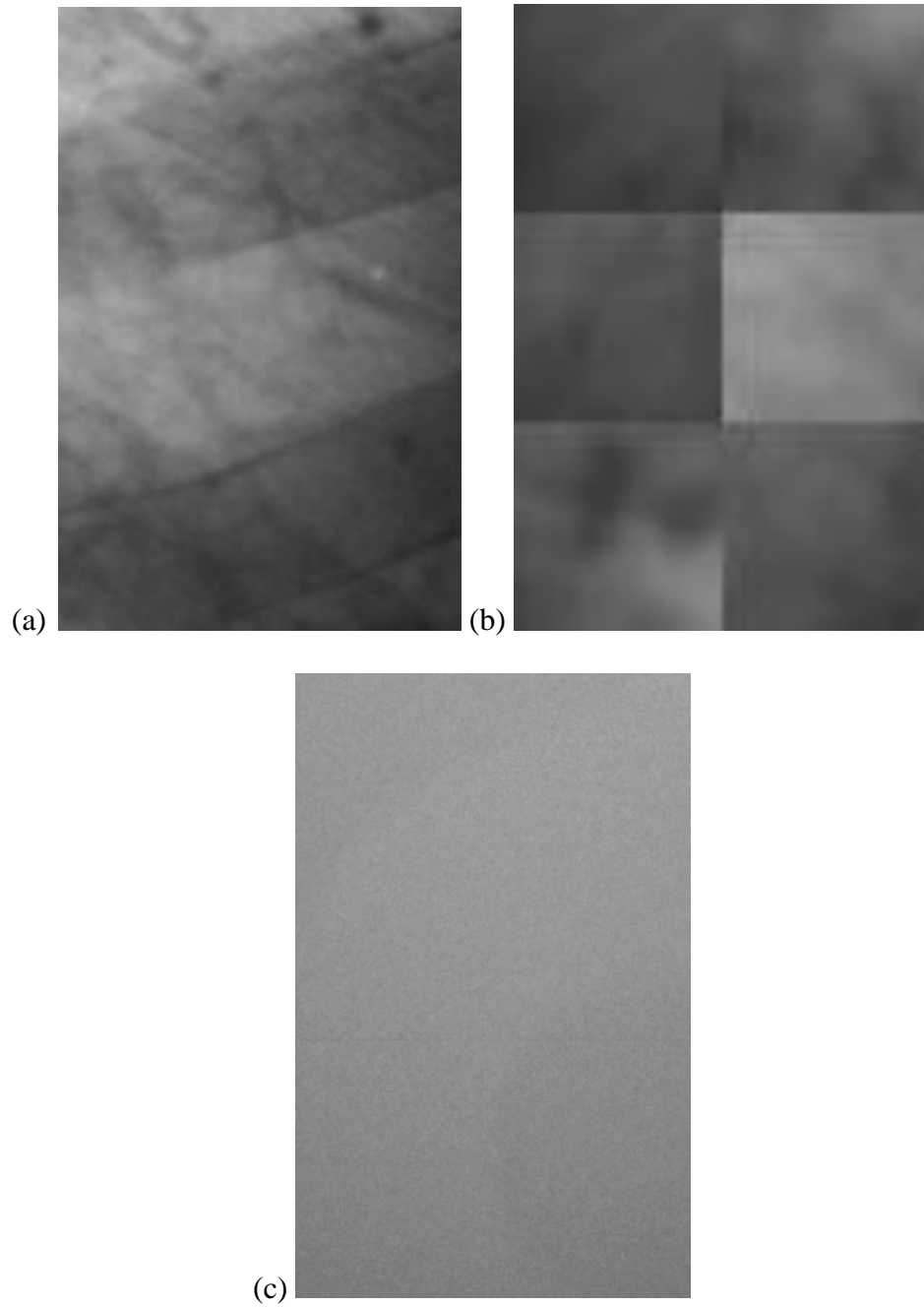


Figure 4.2: Examples of ROIs used for eNNPS calculations for single view CXR (a), stereo/BCI (b) and geometrical phantom (c).

4.2.4 Scatter Measurement

A beam stop technique was used to determine the scatter response of the clinical system.[37, 111, 115] The beam stop array was placed adjacent to the phantoms. The scatter measurement was determined for the adult phantom and the large adult phantom with the phantoms placed adjacent to the detector cover plate and with the phantoms at approximately 50% magnification from the phantom center. The scatter response was determined in the lung field. For comparison, scatter measurements were also taken with the geometrical phantom. A 120 kVp technique with a high exposure setting was used to capture the scatter images for analysis.

The transmission fraction was determined using wide beam geometry and a technique of 120 kVp. The ratio of average exposure with and without phantom present was calculated to obtain the transmission fractions for the adult and large adult phantoms.

4.2.5 Effective Detective Quantum Efficiency

The efficiency of imaging detectors is commonly measured by the DQE.[41, 90, 103, 104, 135] The eDQE has been proposed as a measurement of a complete imaging system in a clinical setting.[17, 113, 115] In this study, the eDQE was calculated in the object plane using the system eMTF and eNNPS as well as the transmission and scatter fractions determined as described in the previous section. The eDQE was calculated in the object plane using an established definition,[17, 113, 115]

$$eDQE(f') = \frac{(1 - SF)^2 \cdot eMTF^2(f')}{q \cdot m^2 \cdot E \cdot \frac{1}{m^2} \cdot eNNPS(f') \cdot TF}, \quad (4.2)$$

where m is the magnification, $f'=mf$ is the frequency in the object plane, SF is the scatter fraction, TF is the transmission fraction, q is the square of the ideal signal-to-noise ratio

(SNR²) per exposure with units of mm⁻²-mR⁻¹, and E is the exposure in units of mR inverse-squared to the detector plane. The m² factor accounts for the change in exposure as a function of magnification and cancels the 1/m² factor for the eNNPS calculation.

4.2.6 Observer Model

The Hotelling SNR² which includes a signal term describes the effects of a specific signal on object detection.[17, 107] The Hotelling SNR² efficiency is the Hotelling SNR² per unit exposure defined[17, 107] as

$$F = 2\pi \int_0^{f_N} S^2(u') eDQE(u') u' du', \quad (4.3)$$

where eDQE(f') is the effective DQE as defined by Eq. 4.2, and S(u') is the Fourier transform of the nodule model defined by Samei and Burgess[20, 107] and calculated using the Hankel transform

$$S_{\text{designer}}(u') = J_{n+1}(2\pi R u') / (2\pi R u')^{n+1}, \quad (4.4)$$

where J_{n+1}(2πRu') is a first order Bessel function, R is the diameter of the nodule, and n is an exponent defining the shape of the nodule. For this study, a 10 mm lesion was used with the task function normalized to unity.

4.3 RESULTS

4.3.1 System Response

The clinical system with the phantoms placed in proximity to the x-ray source was found to have a linear relationship between pixel value and exposure given by Q=3338.2E+188.22. Before analysis, the data were offset corrected to obtain a zero intercept.

4.3.2 Resolution

Figure 4.3 provides a comparison of the vertical eMTF for the adult and large adult phantoms when placed at the receptor and when placed at approximately 60% magnification from the back of the phantom.

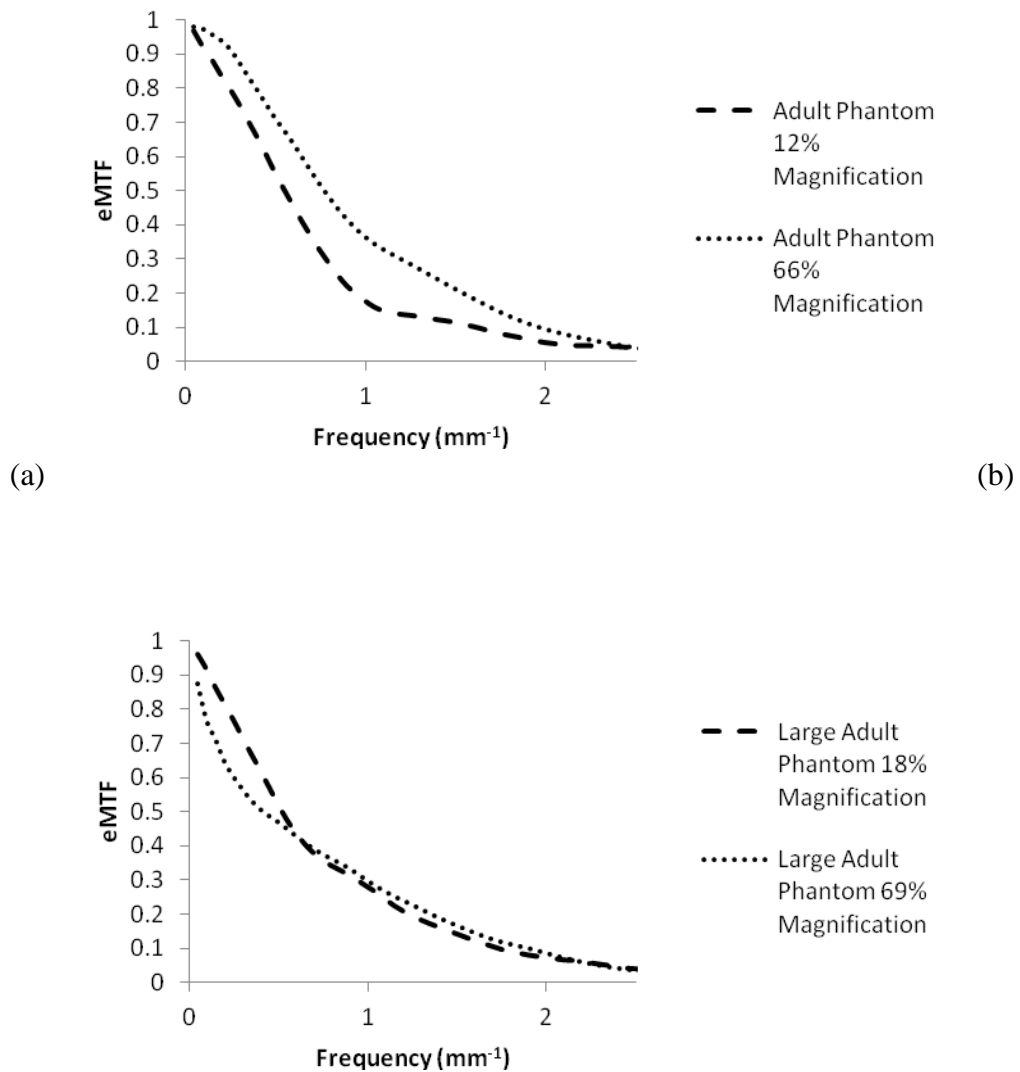


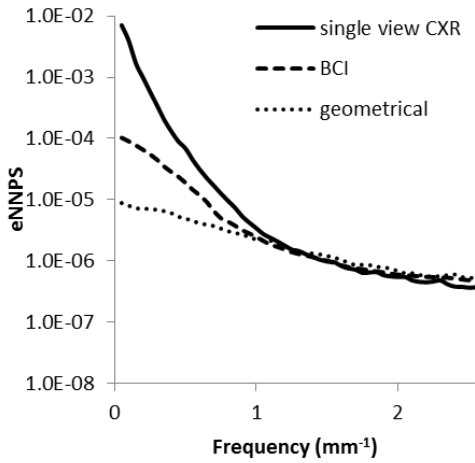
Figure 4.3: eMTF for adult (a) and large adult (b) phantoms at two different magnifications.

As expected from previous calculations using a theoretical model,[17] the magnification for the adult phantom improves the resolution of the system. The large phantom eMTF results indicate that the improvements from magnification are not realized due to the blurring effect of the focal spot. As determined in a previous study, magnification benefits depend on tradeoffs between system parameters and there is an optimum magnification for each system.[17] These results were obtained with the edge located on the tube side of the phantom to maximize the blurring effects of objects on the posterior side.

4.3.3 Noise

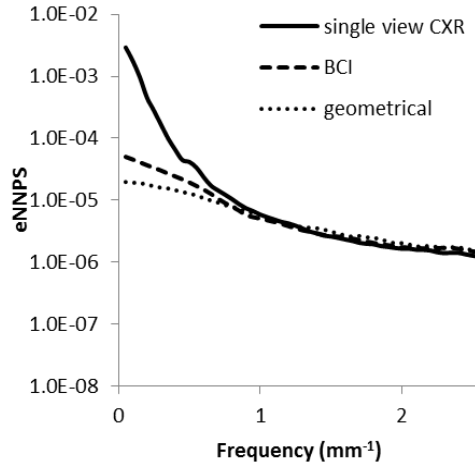
Figure 4.4 shows the results for the noise calculations of the clinical system for two geometries and two iso-dose conditions with E_0 chosen as the nominal dose for the adult phantom. The geometric magnification was defined from the back (tube side) of the phantom to represent maximum magnification effects.

Adult Phantom

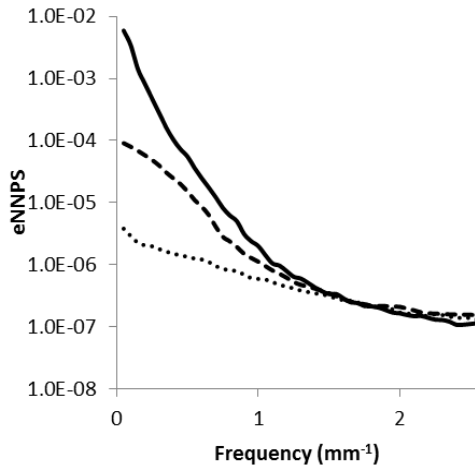


(a)

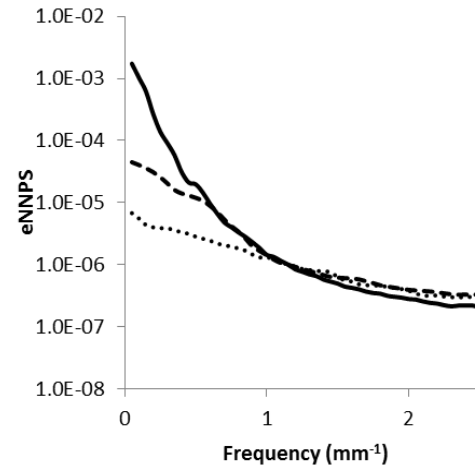
Large Adult Phantom



(e)



(b)



(f)

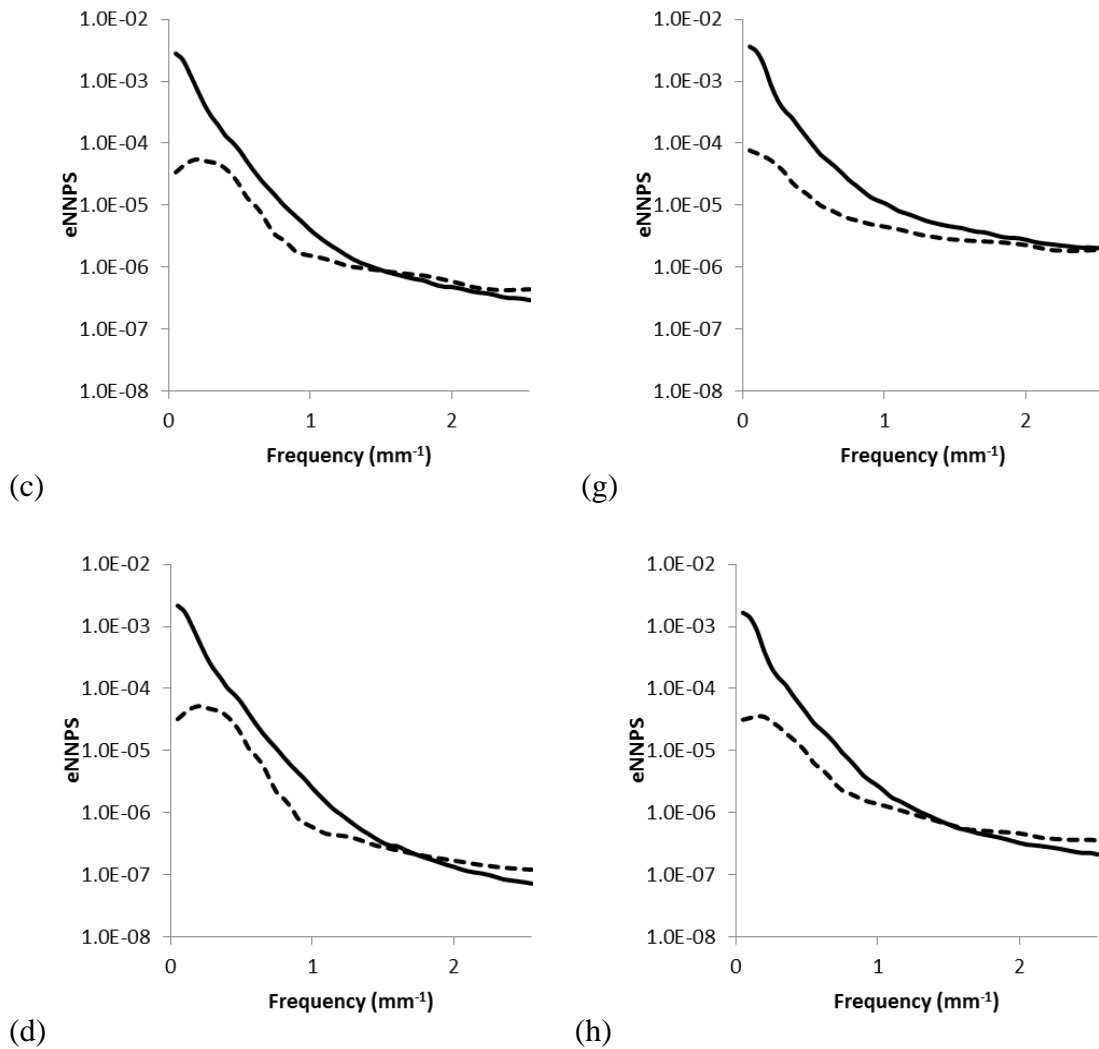


Figure 4.4: CXR, stereo/BCI and geometrical phantom results for eNNPS: adult phantom at $E=E_0$ (a), adult phantom at $E=3.2E_0$ (b), adult phantom 50% magnification at $E=E_0$ (c), adult phantom 50% magnification at $E=3.2E_0$ (d), large adult phantom at $E=E_0$ (e), large adult phantom at $E=3.2E_0$ (f), large adult phantom 50% magnification at $E=E_0$ (g), large adult phantom 50% magnification at $E=3.2E_0$ (h).

At lower frequencies, for all conditions, the eNNPS for CXR and stereo/BCI is degraded compared to the geometrical phantom. This is expected since the CXR and stereo/BCI have more anatomical noise at lower frequencies. Also, at lower frequencies, for all conditions, the eNNPS for CXR is degraded compared to stereo/BCI since

stereo/BCI uses correlation by the averaging operator to suppress the anatomical noise. At higher frequencies where quantum noise is the primary noise component, similar results are obtained for the eNNPS for CXR, stereo/BCI and geometrical phantom.

For all conditions, the eNNPS is improved with increased dose minimally at lower frequencies but noticeably at higher frequencies. Since lower frequency noise is dominated by anatomical noise, increasing dose does not improve detection. However, at higher frequencies, since quantum noise is the dominant noise feature, increasing dose does provide an improvement. Note that for the geometrical phantom which does not include large anatomical structures, the improvement in noise is more pronounced at lower frequencies.

Under iso-dose conditions, increased magnification did not improve the eNNPS which remained unchanged for the adult phantom and was degraded for the large adult phantom. Increasing the distance from the receptor introduces a larger air gap and thus reduces the quanta detected.

For all conditions, comparing results between phantoms, at higher frequencies, the eNNPS for the large adult is generally degraded compared to the adult phantom. This is expected since the large phantom absorbs more photons resulting in fewer detected photons which is reflected in higher quantum noise.

4.3.4 Scatter

Table 4.3 provides a summary of the transmission fractions and scatter fractions obtained using the beam stop method.

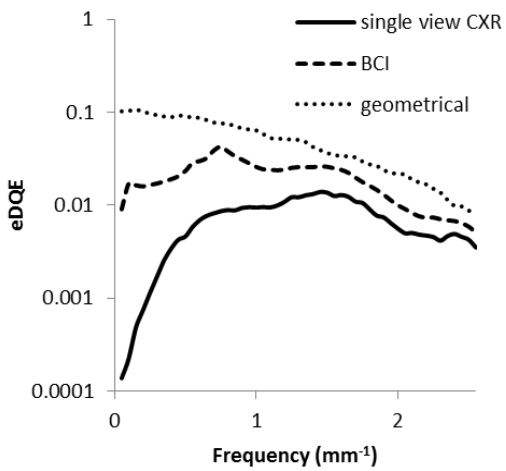
Table 4.3: Scatter and Transmission Fractions

Phantom	Scatter Fraction (%)	Transmission Fraction (%)
Adult at 12% magnification	54.2	16.5
Adult at 66% magnification	32.4	16.5
Large Adult at 18% magnification	69.3	12.2
Large Adult at 69% magnification	48.4	12.2

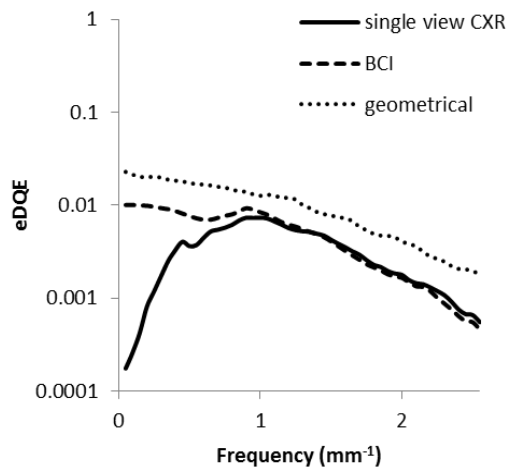
As expected, the scatter fraction increases with the larger phantom. The scatter fraction decreases with increasing magnification since increasing magnification introduces a larger air gap which reduces scatter. For the adult phantom, magnification reduces scatter by 40% and for the large adult phantom, magnification reduces scatter by 30%.

4.3.5 eDQE Results

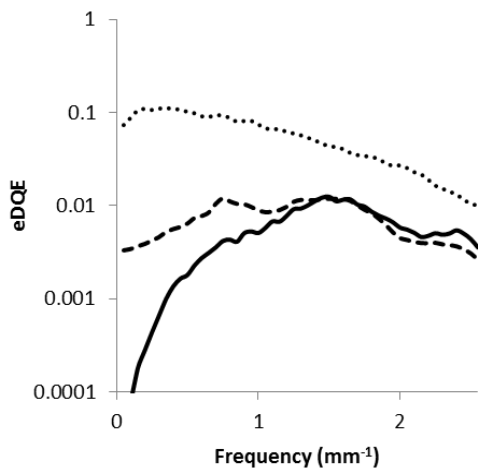
The eDQE results can be seen in Figure 4.5.



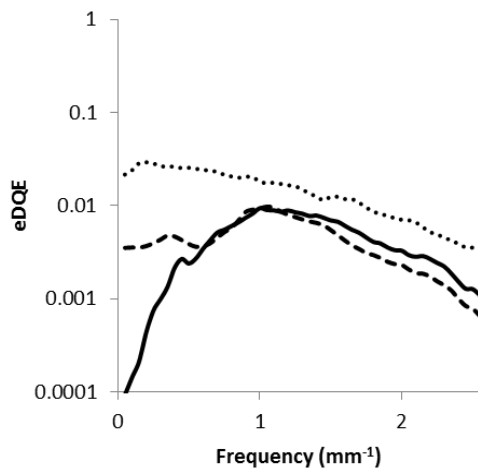
(a)



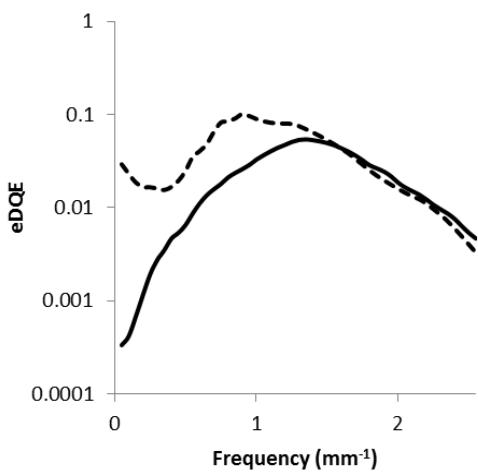
(e)



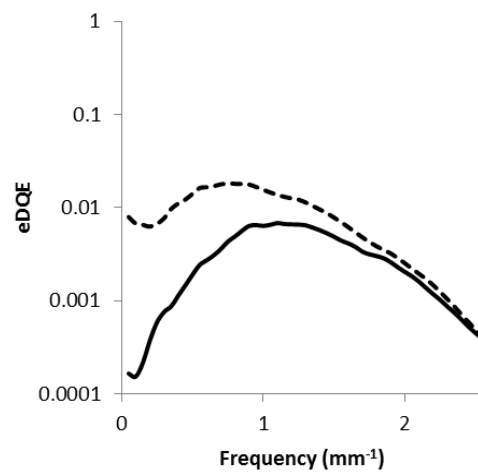
(b)



(f)



(c)



(g)

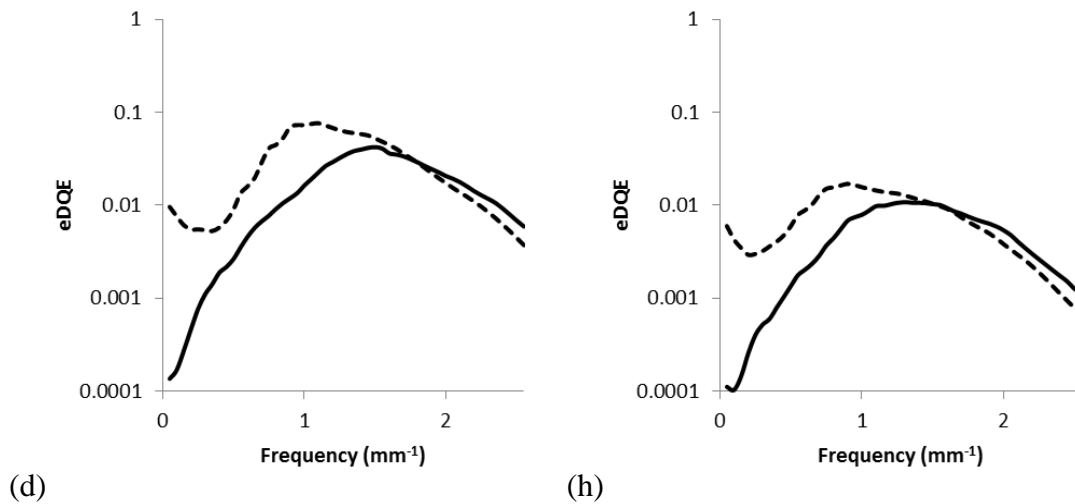


Figure 4.5: CXR, stereo/BCI and geometrical phantom results for eDQE: adult phantom at $E=E_0$ (a), adult phantom at $E=3.2E_0$ (b), adult phantom 50% magnification at $E=E_0$ (c), adult phantom 50% magnification at $E=3.2E_0$ (d), large adult phantom at $E=E_0$ (e), large adult phantom at $E=3.2E_0$ (f), large adult phantom 50% magnification at $E=E_0$ (g), large adult phantom 50% magnification at $E=3.2E_0$ (h).

For all conditions, $eDQE(0)$ for stereo/BCI is ~ 100 times higher compared to single view CXR since anatomical structures are suppressed in stereo/BCI. The $eDQE$ for the geometrical phantom is higher at all frequencies compared to stereo/BCI and single view CXR. For all conditions, the geometrical phantom exhibits ~ 10 times higher $eDQE(0)$ compared to stereo/BCI and ~ 1000 times higher $eDQE(0)$ compared to single view CXR. This result is expected since the geometrical phantom does not contain large anatomical structures which obstruct detection at lower frequencies and absorb quanta which also reduce the $eDQE$ at higher frequencies.

For the adult phantom, for stereo/BCI, E_0 dose results in ~ 5 times better $eDQE(0)$ compared to $3.2E_0$. For the large adult phantom, $eDQE(0)$ is relatively unchanged. These results indicate a task dependent tradeoff as indicated by previous theoretical results.[17]

For the adult sized phantom, for stereo/BCI and CXR, at increased magnification, eDQE(0) results in ~5 times improvement. For the adult phantom, magnification also improves eDQE at higher frequencies for stereo/BCI and CXR. For the large adult, results are similar with and without magnification for stereo/BCI and CXR.

4.3.6 Observer Model Results

The Hotelling SNR^2 efficiency for observer model results for a 10 mm lesion can be found in Table 4.4.

Table 4.4: Hotelling SNR^2 per unit entrance exposure calculated to the detector plane under various noise conditions

Phantom	Exposure	Geometrical	Single View CXR	Stereo/BCI
Adult	$\sim E_0$	0.3559	0.0005	0.0301
12% magnification	$\sim 3.2E_0$	0.2520	0.0002	0.0110
Adult	$\sim E_0$	N/A	0.0011	0.0967
66% magnification	$\sim 3.2E_0$	N/A	0.0005	0.0318
Large Adult	$\sim E_0$	0.0757	0.0006	0.0335
18% magnification	$\sim 3.2E_0$	0.0717	0.0003	0.0117
Large Adult	$\sim E_0$	N/A	0.0006	0.0264
69% magnification	$\sim 3.2E_0$	N/A	0.0004	0.0198

As expected, the geometrical phantom has the highest detectability index since there was no anatomy present. For the adult size, the detectability index for the geometrical phantom is ~10 times better than stereo/BCI. For the large adult size, the detectability index for the geometrical phantom is ~2 to ~7 times better than stereo/BCI. The detectability index for the geometrical phantom is ~1000 times better than single

view CXR for the adult size and ~100 times better for the large adult size. For all conditions, the detectability index for stereo/BCI is ~100 times better than CXR. The results indicate that increasing the dose does not improve the detectability index.

At iso-dose, for the adult phantom, the detectability index is ~3 times better for stereo/BCI with increased magnification. For the large phantom, for E_0 dose, increased magnification did not improve the detectability index for stereo/BCI, but magnification does improve detectability for the $3.2E_0$ dose setting.

4.4 DISCUSSION

Chest radiography has been shown to be limited by anatomical noise resulting in a high miss rate.[102, 107, 130] As a 3D modality, stereo/BCI may suppress the effects of anatomic noise on the detection of subtle lung lesions.[102, 117] Traditionally, the metrics of MTF, NPS and DQE pertain to the imaging detector only. Proposed metrics of eMTF, eNNPS and eDQE capture information for the entire clinical imaging system.[17, 113, 115] The introduction of flat panel detectors has resulted in improvements to imaging technology; however, the geometry of systems incorporating these devices has not been changed from film cassette systems. Theoretically, geometric magnification has been shown to improve the image metrics of eDQE and the detectability.[17, 124, 129] In this work, a clinical imaging system was evaluated in terms of the metrics of eMTF, eNNPS and eDQE as well as the detectability of a 10 mm lesion. CXR and stereo/BCI were investigated at two magnifications under iso-dose conditions with anthropomorphic chest phantoms representing an average adult and a large adult.

The eMTF was found to improve with magnification for the adult phantom but did not improve for the large adult phantom due to focal spot blurring. The eNNPS was

improved at lower frequencies for stereo/BCI compared to single view CXR as expected since stereo/BCI suppresses large anatomical structures. The eNNPS did not improve with magnification.

Stereo/BCI resulted in a higher eDQE than single view CXR. As seen in Table 4.3, scatter fractions improved with increasing magnification as expected by the introduction of an air gap with magnification. The reduction in scatter translated to improved eDQE with magnification at higher frequencies. Effective DQE was not seen to improve with increasing dose. Stereo/BCI resulted in marked improvement in the detectability index compared to single view CXR. Magnification further improved the detectability index; however, increasing dose did not improve the detectability index.

Confirming theoretical results from a previous study[17], the improvement in eDQE as a result of magnification and lack of improvement in eDQE as a function of dose indicate that magnification can be employed without increasing dose while maintaining image quality. The previous theoretical study[17] indicated tradeoffs with image quality based on system parameters. That tradeoff was seen in this study with the large phantom since results did not improve with magnification while results for the adult phantom did improve with magnification. Varying parameters such as focal spot size and pixel size may also affect system performance results. Those parameters were not varied in this study; however, a large focal spot of 0.6 mm was used with promising results for detection with stereo/BCI and magnification.

The noise component of this study for stereo/BCI was generalized to be an averaging operator as a simplified model of the human visual system. This model assumes the human visual system is linear and that the observer is focused on the plane of

the lesion. In reality, the noise in stereoscopic vision is a more complex issue that could be investigated in the future. All anatomical noise was assumed to be detrimental to detection for stereo/BCI and single view CXR. However, when viewing images, the observer can see “through” some anatomical structures and thus those structures are not fully detrimental to detection. Furthermore, anatomical features may actually aid the observer in defining what is considered normal thereby having a positive effect on detection.

Accommodating current imaging systems to capture images for the stereo/BCI modality requires introduction of additional hardware and software for a tube movement apparatus as well as synchronization with the x-ray tube. These modifications were not too complex or expensive compared to other options such as computed tomography; therefore, retrofitting existing systems is feasible. To incorporate higher magnification, larger detectors will be necessary to accommodate the larger field-of-view from magnified images. Typically, detectors are sized according to the body part to be imaged but magnification will require larger detectors operating with lower instrumentation noise levels which will also increase the cost of the clinical system. Correspondingly, larger monitors will be necessary to provide realistic image display of the magnified images. Stereoscopic monitors will be needed to display the stereo/BCI images. Recent technology improvements have provided stereoscopic monitors that are not as cumbersome to use compared to previous generations and therefore possibly more effective for radiological interpretation.

4.5 CONCLUSION

The stereo/BCI modality and geometric magnification could improve detection of subtle lung nodules and should be considered in clinical system development. Increased dose did not appear to improve detectability. Clinical system parameters may vary the success of detection and should be carefully considered during system development.

CHAPTER 5

Preliminary evaluation of bi-plane correlation (BCI) stereoscopic imaging for lung nodule detection

5.1 INTRODUCTION

Although lung cancer is consistently the leading cause of death due to cancer in the United States[3], a viable screening method has been elusive.[54] Chest radiography is inherently limited by overlapping structures which may hide cancerous nodules making them undetectable.[110] A recent study performed by the National Lung Screening Trial (NLST) using computed tomography (CT) showed a 20 percent reduction in death due to lung cancer mortality.[60] However, CT is controversial due to the higher radiation doses required, higher cost and the large number of indeterminate nodules.[1, 55, 82, 131] The speed of acquisition available with flat panel imaging technology has made bi-plane stereoscopic systems feasible. Stereoscopic mammography has shown promising results for identifying nodules in the breast.[43] It is natural to explore whether stereoscopic chest imaging may also provide a cost effective, time sensitive imaging technique for lung nodule detection.

In our lab, we developed a bi-plane correlation (BCI) imaging system that generates images for stereoscopic viewing.[22] The stereoscopic images may be used to determine if a BCI stereoscopic system is a viable option for lung nodule detection.

Overlapping anatomical structures are minimized in the stereoscopic view providing more accurate nodule detection. Three images are acquired, two at oblique angles and a third at the PA position. Total dose is equivalent to a standard PA chest radiography procedure[80] and the images are acquired in one breath hold, less than 10 seconds. This study investigates whether using stereoscopic visualization provides superior lung nodule detection compared to standard PA image display.

5.2 METHODS

The BCI system shown in Figure 5.1 was used to acquire image data containing lung nodules as well as normal cases from human subjects under institutional review board approval. After requesting permission from the referring physician, the study coordinator recruited subjects referred for CT exams. The study coordinator initially identified subjects with primary or metastatic cancer for positive cases as well as those without abnormality for normal cases. Clinical co-investigators reviewed the subject clinical notes to verify general good health, the presence or absence of cancer and the absence of acute pulmonary abnormalities. Pregnant women were excluded as well as students or patients of any key personnel in the study. Once the study coordinator and clinical co-investigators reviewed the clinical notes and confirmed the subject was a candidate for the study, the study coordinator approached the subject for potential recruitment. If the subject agreed to participate and was competent to give consent the study coordinator arranged for image acquisition. The images were acquired using a Varian Medical Systems, Inc PaxScan 4030CB system which has an imaging area of 40x30 cm with an image matrix size of 2048x1536 pixels and pixel size of 194 microns. A source-to-image distance of 183 centimeters, and full resolution mode at 1 frame per

second were used for image acquisition as determined in a previous study.[17] The raw image data was offset and gain corrected as instructed by the manufacturer. Data were acquired without an anti-scatter grid which is not standard for current chest radiology exams.



Figure 5.1: BCI acquisition system[22]

Human subjects consisted of men and women to comprise a data set of 60 total subjects. Three images were acquired, one at the posterior-anterior (PA) position and two at oblique angles of ± 3 degrees of PA (Figure 5.2). The system geometry used was studied in previous works which determined the optimal operating angles for acquisition.[102, 117] The x-ray tube moves along the horizontal axis to acquire the 3 images. The subject data was acquired with effective tube current adjusted accordingly for patient thickness at the chest. Total effective dose was equivalent to standard chest radiography procedures as estimated from data presented by Mettler, et. al[80]. Raw image data was post-processed using histogram equalization and filtering. Prior to the study, the window/level was adjusted for optimal viewing on the stereoscopic display and the observers were not allowed to change the window/level during the study.

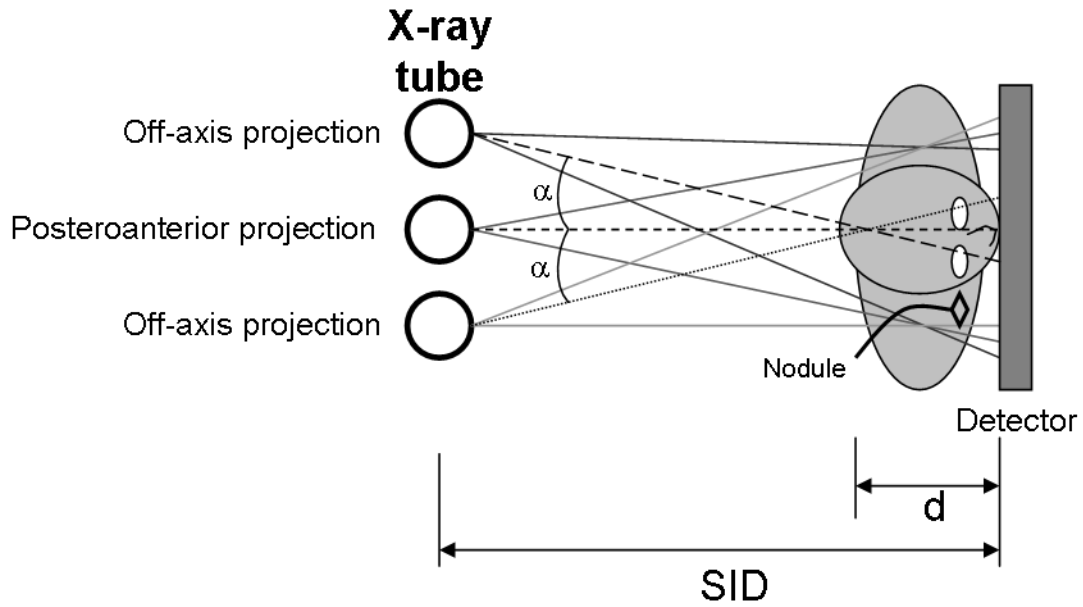
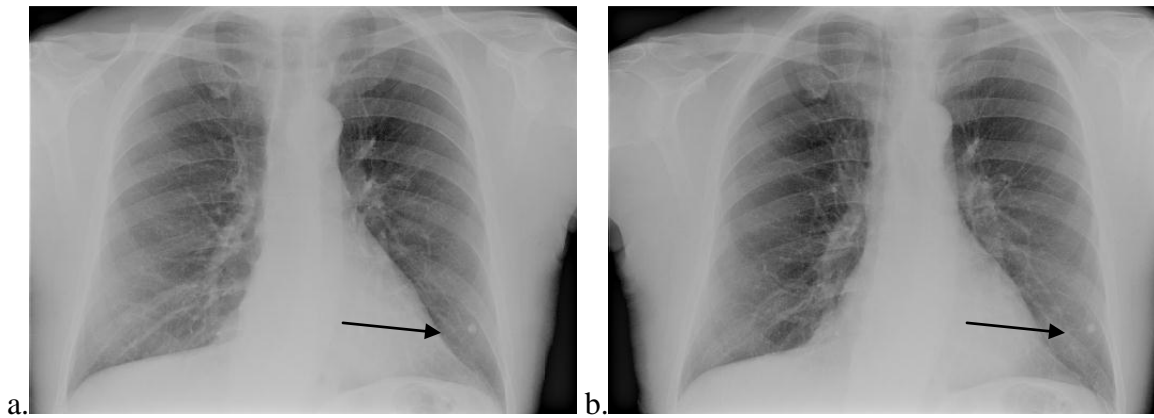


Figure 5.2: BCI acquisition geometry where the angle $\alpha = 3^\circ$ as measured from the center of the beams.

Examples of processed images are shown in Figures 5.3a-b. Figure 5.3a is shifted 3 degrees to the left of PA and Figure 5.3b is shifted 3 degrees to the right of PA. The arrow indicates a lesion which is zoomed in Figures 5.3c-d. Figure 5.3d shows that the lesion appears to be obscured by a rib but in Figure 5.3c the lesion is unobstructed.



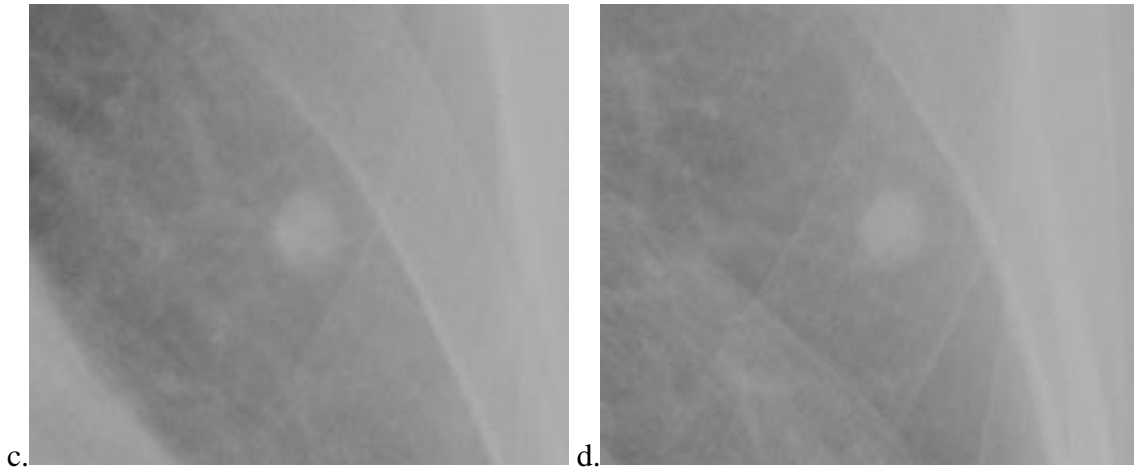


Figure 5.3: Sample images (a-b) and zoom images of lesion (c-d)

For the observer study, four radiologists who specialize in chest radiography, each with over 7 years of experience were asked to view the PA image and BCI image of each subject on a stereoscopic display. The stereoscopic display used was a prototype 5 megapixel medical display (Dome C5iGRAY by Planar Systems, Inc., Beaverton, OR). Two of the monitors are mounted as shown in Figures 5.4 and 5.5 with an approximate 110° separation and a semitransparent mirror bisecting the angle. As illustrated in Figure 5.5, the image from the top monitor is reflected off the mirror while the image from the bottom monitor is transmitted through the mirror. Cross-polarized lenses are required such that each eye only sees an image from one monitor. The left eye receives the image from the bottom monitor and the right eye receives the image from the top monitor. The human visual system effectively sums the two views often referred to as binocular summation. The monitors were calibrated geometrically by visual alignment of a matrix of dots and squares on a flat background.

The PA image was displayed on both monitors simultaneously, thus appearing as a flat image similar to standard chest radiographic image display. The oblique images at

+/- 3 degrees were displayed simultaneously, one on each monitor. Then, with the cross-polarized glasses provided which pass the right and left view to only the right and left lens respectively, a 3D image was displayed. The radiologists were trained to view the BCI stereoscopic image before proceeding with the full study. For each subject in random order and using a sequential reading method, the radiologists viewed the PA image monoscopically and provided a score and then immediately viewed the BCI stereoscopic image of the same subject and provided a score on a scale of 0-100 with zero representing the absence of lesion and 100 representing certainty of a lesion.



Figure 5.4: Stereoscopic viewing system

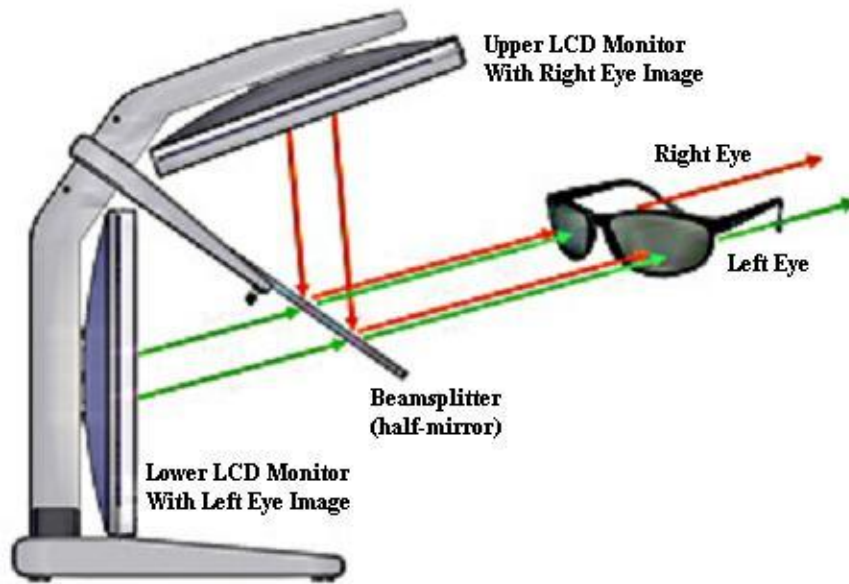


Figure 5.5: Schematic of stereoscopic image formation[94]

The cases considered positive were independently determined by CT data acquired the same day as the BCI data. All nodules identified using CT were considered to be positive lesions for a total of eight confirmed nodules. Performance was evaluated by comparing the scores of the PA viewing and the BCI stereoscopic viewing to the CT results. Receiver operating characteristic (ROC) analysis was performed for each radiologist and across all radiologists. The ROC analysis considered the left and right lung as separate entities. Evaluation of the stereoscopic view compared to the PA view was based on three figures of merit which were sensitivity, positive predictive value (PPV) index and false positives per subject.[102]

5.3 RESULTS

The system and observer study performed for the BCI stereoscopic images showed a reduction in the total number of false positives of 35% compared to the PA images. The reduction in false positives led to an increase of 20% in the PPV index with

the BCI images having a PPV of 0.31 and the PA images having a PPV of 0.26.

Sensitivity for the BCI images was 71% compared to 86% for the PA images, a reduction of 15%. The ROC curves for each radiologist can be seen in Figures 5.6a-d and the average of the ROC curves can be seen in Figure 5.6e. The ROC curves show that BCI improved performance of the fourth radiologist and generally performed similarly to viewing the PA image alone. Radiologists commented that viewing the stereoscopic image took some adjustment but by the end of the study, most were comfortable with the 3D image view.

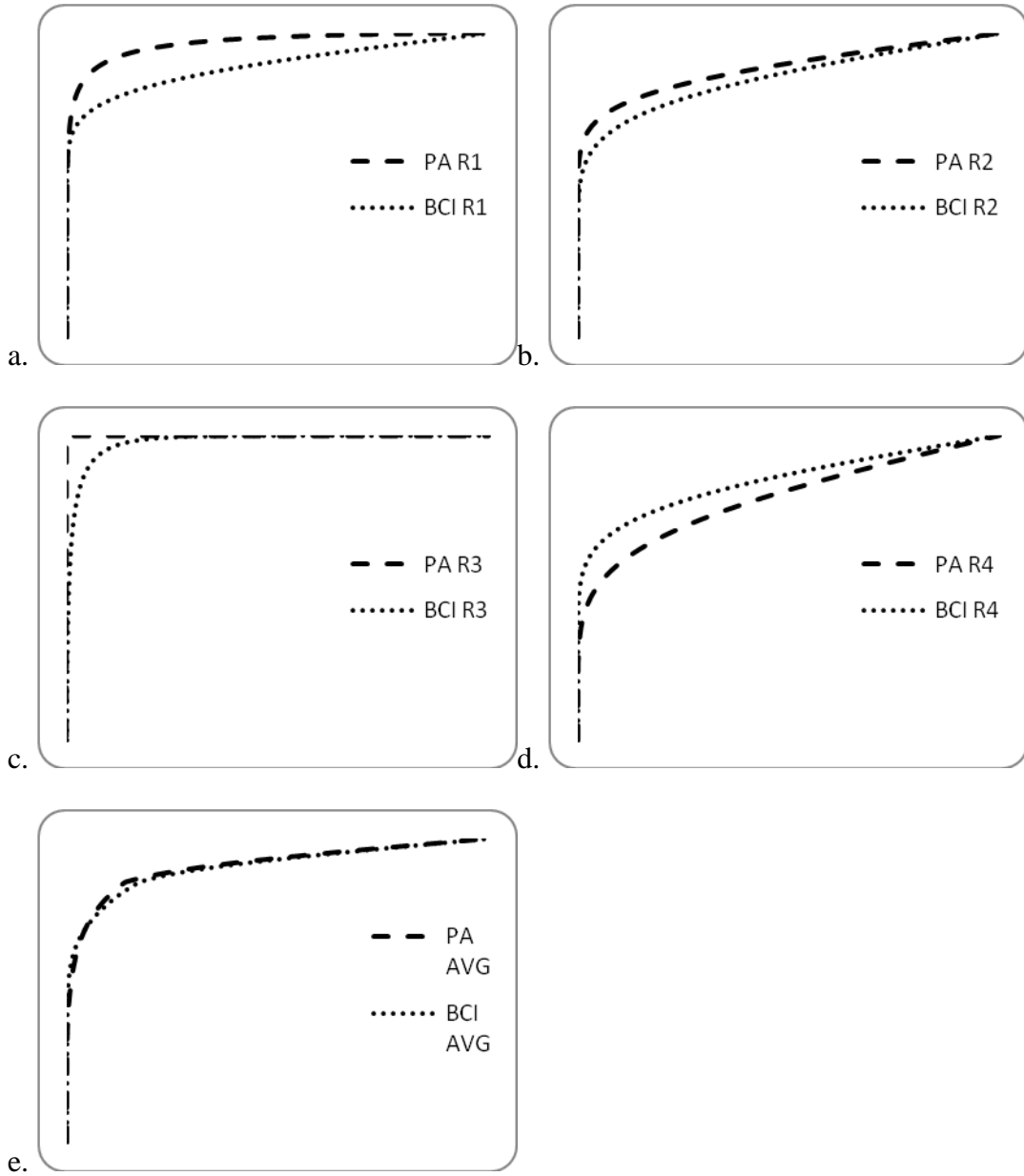


Figure 5.6: ROC performance of PA study as dashed lines and BCI study as dotted lines for 4 radiologists (a-d). and e. Average of ROC curves

Table 5.1 lists specific values of observer performance statistics. As can be seen, all readers except one experienced a reduction in the number of false positives perceived.

Table 5.1: Observer Performance Statistics

	FPs PA	FPs BCI	area PA	area BCI	Sensitivity PA	Sensitivity BCI	PPV PA	PPV BCI
Reader 1	25	12	0.972	0.909	100%	71%	0.22	0.29
Reader 2	23	10	0.902	0.877	86%	57%	0.21	0.29
Reader 3	8	13	1	0.983	100%	100%	0.47	0.35
Reader 4	12	9	0.831	0.877	57%	57%	0.25	0.31
Average	1.1 per subject	0.7 per subject	0.926	0.912	86%	71%	0.26	0.31

5.4 DISCUSSION

Recently, the NLST reported that screening high risk individuals with CT is associated with a 20% reduction in lung cancer mortality, and a 6% decrease in overall mortality.[60] However, the dose and frequency of CT in asymptomatic individuals needs to be considered. Stereomammography has generated positive results leading to the current effort of a newly proposed BCI stereoscopic system for use as a system for lung nodule detection. The proposed system provides advantages over CT in that the dose is notably lower. One study reported that the average effective dose from a chest PA exam is 0.039 mSv while the average effective dose of a chest CT exam is 3.2 mSv.[142] Although efforts towards CT dose reduction have shown a 67% decrease in dose without affecting lung nodule detection, optimal acquisition parameters and adequate detection are still debated.[65]

Samei, et al demonstrated that anatomic noise prevents detection of subtle lung lesions more than radiographic noise.[108, 110] For a reader to distinguish a lesion in a background of anatomical noise, the lesion needs to be an order of magnitude larger than

the same lesion on a quantum limited background.[110] Another report determined that anatomical obstructions result in a 71% miss rate.[130] Viewing bi-plane images stereoscopically provides the radiologist with a visual reduction of anatomical noise. Stereoscopic photography was popular at the turn of the twentieth century and physicians at that time developed techniques for viewing medical images stereoscopically.[42] Viewing the x-ray films required awkward handheld viewing devices and involved difficult alignment of the images.[42] However, stereoscopic imaging was used in radiology departments until CT and MRI systems became available.[42] The introduction of flat panel detectors and stereoscopic display systems has provided improved technology for viewing stereoscopic image pairs as 3D images. Although CT provides superior data for 3D visualization, stereoscopic imaging provides a 3D visualization that minimizes anatomical noise compared to chest radiography at a reduced cost and dose compared to CT.

Preliminary studies have been performed with phantom and human subject data to assess how correlating suspect lesions from multiple views of a standard CAD algorithm may eliminate false positives.[88, 89, 102, 117] One of those studies of BCI for lung nodule detection demonstrated a sensitivity of 62.5%, 1.5 false positives per image and a 0.885 PPV index.[102] The BCI reduced sensitivity by 20% compared to single view CAD but also reduced false positives by 94% yielding a 140% improvement in the PPV.[102] A multiprojection CAD scheme for chest was used in a study of phantom and human subject data.[117] Compared to single view CAD at a sensitivity of 65%, the multiprojection correlated CAD reduced false positives by 79% in the phantom study and 78% in the human subject study.[117] Advantages of multiprojection CAD have been

demonstrated successfully on small data sets. Applying CAD to the subject data from this study with stereoscopic visualization may prove beneficial.

The current study indicated promising results for a BCI system in that it compares comparably to chest radiography and established proof of principle for the new imaging modality. However, the number of subjects was small and cannot fully establish the effectiveness of detecting lung nodules with BCI stereoscopic imaging. Further research is proceeding to use the BCI stereoscopic system in conjunction with the PA image as a supplemental tool for nodule detection. The lesions in the study were considered obvious lesions that were easily detected by standard chest radiography; therefore, full benefits of BCI stereoscopic imaging were not exploited. Future endeavors should include more subtle lesions to examine improved detection compared to chest radiography. The BCI stereoscopic score was probably biased by requesting the observer to score the PA image first; thus, resulting in similar ROC curves between PA images and BCI stereoscopic images. To more accurately determine the benefits of the BCI stereoscopic system, the design of the observer study will be improved so the effectiveness of BCI stereoscopic imaging is more deterministic. A larger data set is also needed to completely verify the validity of the new system. Advantages of using multiprojection correlated CAD results in a reader study should also be explored. As a previous study showed, this study further demonstrated the variability of observers when viewing stereoscopic images[46] and future work should include a stereoscopic depth acuity test for the readers.

CHAPTER 6

Observer study of a bi-plane correlated (BCI) stereoscopic imaging system for lung nodule detection

6.1 INTRODUCTION

The leading cause of death due to cancer in the United States is lung cancer which results in almost one third of total deaths from cancer.[3] Unfortunately, there is no standard-of-care lung cancer screening program like there is for breast cancer. Therefore, most lung cancers are detected either incidentally on radiologic studies performed for other purposes or in symptomatic patients. Lung cancer screening has not yet garnered widespread support.[54] Chest radiography is the most common form of imaging of the lung, but detecting subtle lung nodules with chest radiography is limited by contrast to noise ratio (CNR), perceptual errors and anatomical noise resulting in a high rate of “missed” lung nodules or cancer.[102, 130] The CNR has been improved by the introduction of flat panel detector imaging systems.[101, 104] If anatomical noise could be suppressed by a modality such as BCI, lung cancer screening could be more effective.

Recently, the National Lung Screening Trial (NLST) has shown a 20 percent reduction in mortality due to lung cancer in a cohort of patients screened with low-dose computed tomography (CT).[2, 60] Although, CT may prove to be an effective screening correlation imaging (BCI). The use of bi-plane correlation imaging has become feasible

This chapter is based on a paper by Sarah J. Boyce, H. Page McAdams, Qiang Li, Lacey Washington, Jared Christensen, Danielle Seaman, Juliana Bueno Melo, Erica Berg, Emily Eads, Laura Heyneman, Quan Zhou, Kingshuk Roy Choudhury, and Ehsan Samei, “Observer study of a bi-plane correlated (BCI) stereoscopic imaging system for lung nodule detection”, submitted for review, Medical Physics, 2013.

with flat panel detector systems which provide fast acquisitions necessary for successful correlation without the use of registration algorithms. Viewing bi-plane correlation images in 3D on a stereoscopic display will reduce anatomical obstructions. Studies for stereomammography have shown that bi-plane correlation imaging of the breast can be beneficial[42, 43] Preliminary studies of BCI for chest using phantoms and a small patient subset demonstrated that chest BCI is feasible.[102, 117] The preliminary studies also further explored the use of computer-aided detection (CAD) using the correlated images.[101, 117] CAD algorithms as second readers in chest radiography have been shown to improve detection rates, but those algorithms often result in high false positive findings. However, the number of false positives may be reduced with the use of geometrical correlated data from the BCI.[13, 61, 101, 117]

This study explores the feasibility of a prototype BCI system for detecting subtle lung nodules in human subjects. The system acquired the PA image as well as oblique images at ± 3 degrees off of PA in the horizontal direction. Image acquisition took place within a 10 second single breath hold, and the total dose was equivalent to standard PA chest radiography. The data from sixty human subjects was obtained and scored by radiologists using a stereoscopic display. In addition, a correlated computer-aided detection (CAD) algorithm was used to act as a second reader during the observer study.

6.2 METHODS

6.2.1 Image data

Image data from human subjects was acquired with institutional review board (IRB) approval using a prototype x-ray system previously described by Chawla, et al.[22] The flat panel detector used in the system was a 4030CB developed by Varian Medical

Systems, Inc. which produced a 40x30 cm 14-bit image on a 2048x1536 matrix size with a pixel pitch of 0.194 mm. The image data were corrected for gain, offset, and defective pixels automatically within the system producing the raw image data used for the study. The physical evaluation of the system was performed in a previous study.[16] The x-ray tube used with the system was retrofitted from a standard table mounted radiography system previously used in the radiology department at the Duke Medical Center. The x-ray tube was mounted to translate horizontally to acquire images at the standard PA center as well as angles of ± 3 degrees of center. The source to image distance was 2 meters and no antiscatter grid was used which is not in accordance with standard chest x-ray practice. Figure 6.1 shows the BCI acquisition geometry.

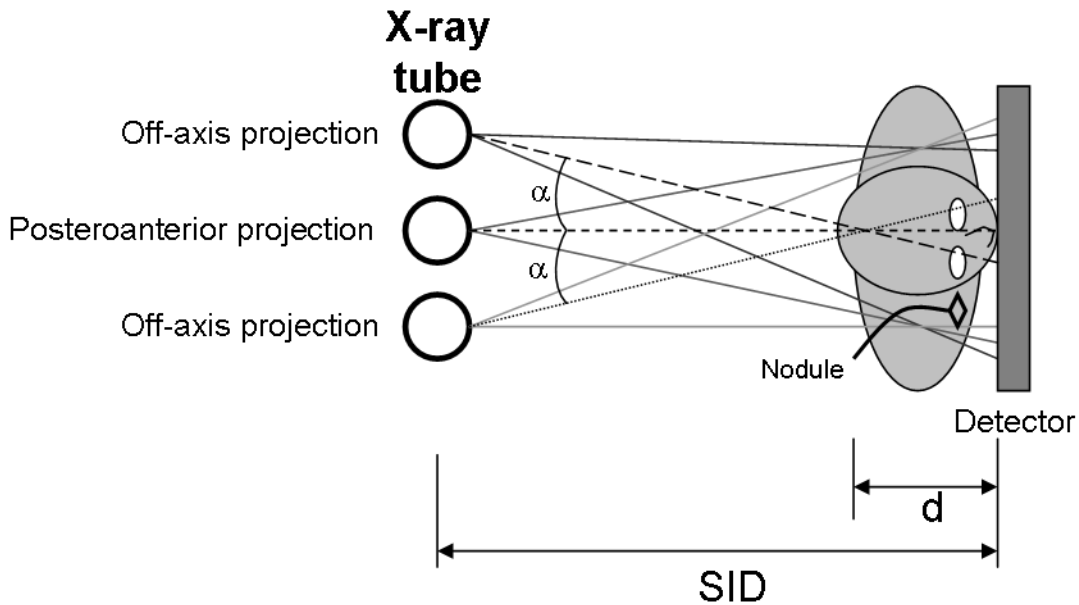


Figure 6.1: BCI acquisition geometry where the angle $\alpha = 3^\circ$ [15]

Images were acquired from 60 human subjects referred for CT exams between April 2007 and Sep 2008. The BCI exam was performed after the CT exam on the same day. A 120 kVp tube voltage was used and the tube current varied from 1-5 mAs depending on the patient thickness (d in Figure 6.1). Using current standard-of-care guidelines for lung nodule CT, a chest radiologist (HPM) with more than 15 years of experience viewed the CT images and identified candidate lesions larger than 5mm. If a nodule was identified from the CT image, the nodule was considered to be a true lesion such that eight lesions sized 5-18 mm in 6 subjects were determined to be true lesions. Other cases free of lesions or with lesions smaller than 5 mm were considered normal.[15]

6.2.2 Image Processing

As previously mentioned, the acquisition system performed gain, offset and defective pixel corrections of the data internally resulting in the raw image data set. However, the different views of the same subject had different ranges leading to mismatches in stereoscopic viewing. These data range differences between images for the same case were due to two main factors. First, the acquisition system stored a single calibration file for the PA image and thus the oblique images were slightly miscalibrated since the x-ray tube was at an angle with respect to the detector. Secondly, even at slight angular differences, the depth of tissue exposed was different resulting in variable energy received by the detector. To minimize different data ranges, the raw image data histograms were adjusted so that the images were within the same data range as per the following equation,

$$I = \left(\frac{I_{\max} - I_{\min}}{P_{\max} - P_{\min}} \right) (L - P_{\min}) + I_{\min} , \quad (6.1)$$

where I is the final image, I_{\max} and I_{\min} are the maximum and minimum values of the final image, p_{\max} and p_{\min} are the maximum and minimum values of the thresholding histogram, and L is the logged image mapped to 14-bit data. The thresholds of the histogram were chosen to include essential anatomy and to exclude the direct exposure area to the detector (the area over the shoulders).

Additional imaging processing was performed with a custom software tshow, Henry Ford Health System. The software performs detail contrast enhancement (DCE), edge restoration, noise reduction and gray scale rendition.[39] DCE was performed to enhance high spatial frequency structures while maintaining low frequency components

of the image. An unsharp mask method with a 20 mm FWHM kernel and a gain of 1.5 was used. Edge restoration was performed using the MTF model by Barrett and Swindell[39] with values of 1.23 cycles/mm at 0.5 MTF and 1.5 as the 1/MTF gain factor of the model. Noise reduction was performed with a classical Butterworth filter with a cutoff frequency of 2.5 cycles/mm and an order of 2.0. Grey scale rendition was performed using an emulation of commercial Hurter and Driffield curve.

6.2.3 Lesion Simulation

Due to the limited data set of true lesions, simulated lesions were incorporated into normal (i.e. nodule free) subject images. The goal was to strengthen the statistics of the study without acquiring additional human subject data, a time extensive task. The simulated nodules were based on a 3D algorithm developed for CT by Li, et al.[71] The simulated nodule was designed to be asymmetric in shape and to emulate features of real lesions including diminishing edges. The simulated nodule was demonstrated to be indistinguishable from real lesions in an observer study.[71] The 3D lesion from the study by Li, et al. was based on a 2D mask defined as a contrast-profile equation initially proposed for chest radiography by Samei[106] and reformulated by Burgess.[20] Therefore, the 2D simulated lesions used were well established as representing real lesions for the purpose of this observer study.

For the simulation, lesion diameters were chosen to be 12-14 mm but due to the diminishing edge effect of real lesions, the lesions appeared somewhat smaller. The peak contrast chosen for the simulated lesions was based on a previous work which found the peak contrast-to-diameter ratio to be approximately 0.00816/mm.[110] The PA image was used to select random locations for placement of the simulated lesions such that the

simulated lesions in the oblique views were not obstructed. A shift and add technique was then used to place the same simulated lesion in the oblique angle views. The lesion was shifted in the horizontal direction to match the acquisition geometry such that the pixel shift was given by

$$p_{\text{shift}}(d) = \frac{d}{2} \tan(\alpha) \frac{1}{p}, \quad (6.2)$$

where d is the patient thickness in cm, α is the oblique angle in degrees, and p is the pixel pitch in cm. As per a previous study[16] that determined the flat panel detector to be linear, the lesion was added to the logarithmic image as

$$I = c(gE + o) \text{ or } \log(I) = \log(c) + (\log(g) + \log(E)) \quad (6.3)$$

where I is the image, c is the contrast, g is the gain of the flat panel detector, E is energy and o is the offset of the flat panel detector which was zero. The simulated lesions were placed in the images and then shown to a radiologist who scored them from 1-5 for subtleness with one being least subtle. The contrast values of the simulated lesions were modified for each image until most scores were 3 or 4. The final contrast values ranged from 0.005/mm to 0.015/mm. We believe the resultant variation in these values compared to 0.00816/mm was due to scatter in the images since an antiscatter grid was not used during data acquisition.

6.2.4 Computer Aided Detection Scheme

CAD lesion selection was performed using a fusion CAD scheme for lung nodule detection.[50] The study performed conventional CAD steps including the identification of candidate lung nodules, segmentation of nodules with dynamic programming, extraction of 33 features from nodule candidates and reduction of false positives.[50] In

addition, the CAD scheme used correlation information from the oblique views to register candidates from all three views and reduce false positives by selecting only nodules present in at least two views.[50] The sensitivity of the fusion CAD scheme employed for this observer study was 65% with 1.9 false positives per case.[50] By comparison, the conventional CAD scheme reported 11.3 false positives per image at 65% sensitivity.[50]

6.2.5 Observer Study

Four experienced radiologists (LW, JC, LH, QZ) with over 10 years of experience and four radiology fellows (DS, JBM, EB, EE) viewed the BCI images on a Dome EX Display which is a stereoscopic display developed by Planar Systems, Inc. The Dome displays were mounted as shown in Figure 6.2. The radiologists performed the observer study in 2 readings separated by enough time such that likelihood of any recall of a particular subject was minimized. Two image viewing protocols were used. In the first protocol, the radiologist viewed and scored the PA image from the BCI acquisition. In the second protocol, the radiologist viewed the PA image immediately followed by the stereoscopic image pair but only scored the stereoscopic pair. In the second protocol, after viewing and scoring the stereoscopic image, the observer was shown the CAD results in the stereoscopic display and another score was rendered.

The same subject was only viewed once per reading necessitating 2 separate reading sessions for each radiologist. The image data set was randomized across the two readings such that the PA only scoring scenario and the stereoscopic scoring scenario were not included in the same reading. The PA image and stereoscopic paired data were viewed on the same stereoscopic display, but the PA image was seen on both monitors

simultaneously as a monoscopic flat image similar to chest radiography. Viewing the PA image on the same monitor provided the same viewing environment since the stereoscopic viewing glasses decrease the image brightness.



Figure 6.2: Stereoscopic viewing system

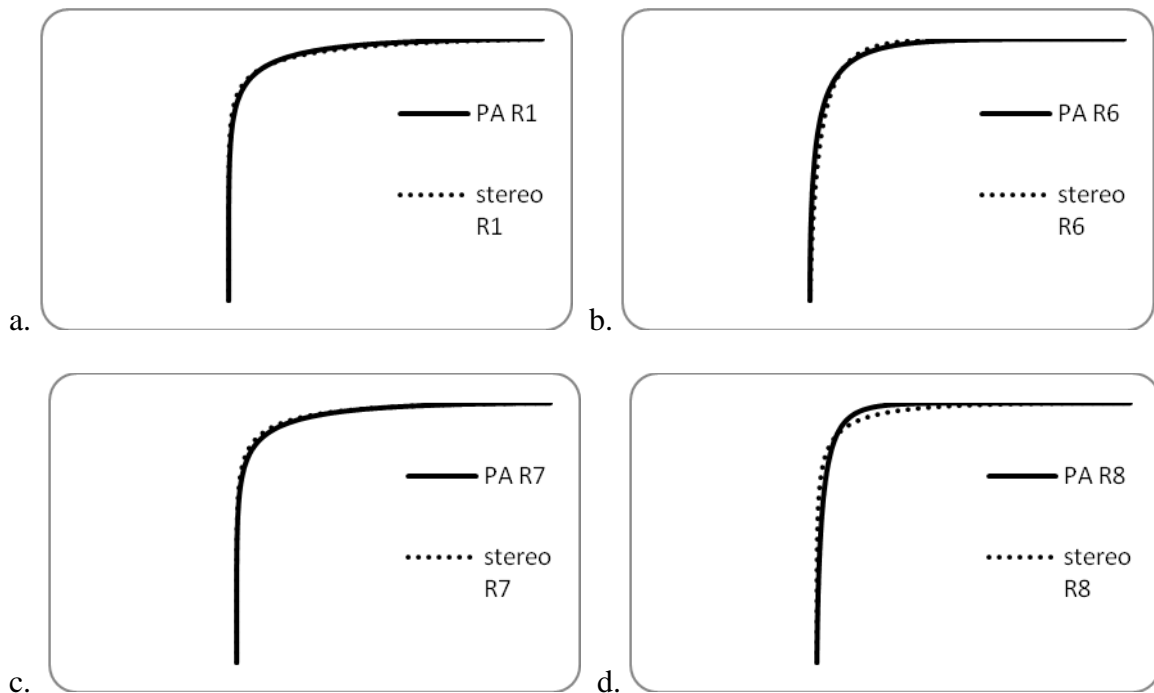
6.2.6 Statistical Analysis

The scores provided by the radiologists were used as the confidence ratings in the receiver operating characteristic curve (ROC) analysis. Scoring was based on a scale of 0-100 with zero indicating the absence of lesion and 100 indicating certainty of the presence of a lesion. The area under the curve (AUC) was used as an overall measure of reading accuracy of each reader. We performed a multi-reader, multi-case (MRMC) ROC analysis of variance of the AUC values, using the DBM MRMC 2.1, Beta Version 2 software developed by Berbaum, et. al.[10, 83] The methodology assumed that confidence ratings arose from separate normal distributions depending on whether the

case was positive or negative. A type I error rate of $\alpha = 0.05$ was used for testing the hypothesis.

6.3 RESULTS

For radiology fellows, the MRMC analysis estimated a 2.8% improvement in AUC for lesion detection (p -value=0.005). The 95% confidence interval was (0.9%, 4.8%). For experienced radiologists, the MRMC analysis indicated no significant difference between monoscopic and stereoscopic modalities (p =0.13). The 95% confidence interval was (0.4%, 3.2%). The ROC curves showing the results for standard monoscopic PA and stereoscopic views are shown in Figure 6.3. The ROC curves for the experienced radiologists demonstrate equivalency between the two viewing methods while the ROC curves for the less experienced radiologists indicate that stereoscopic viewing aids in detection compared to monoscopic viewing.



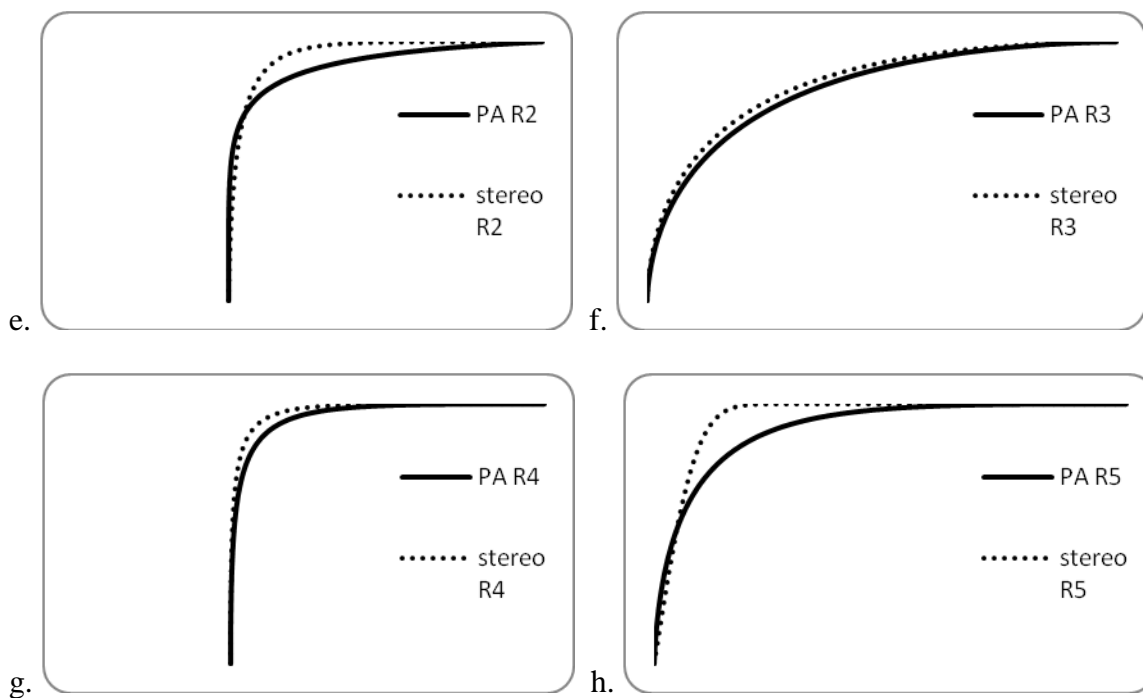


Figure 6.3: ROC curves for 8 radiologists, dashed lines are for stereoscopic while solid lines are for monoscopic. Figures a.- d. are results for experienced radiologists while e. – h. are results for inexperienced radiologists.

Table 6.1 lists statistics for the ROC results for the false positives (FPs), AUC, sensitivity and positive predictive value (PPV) for monoscopic and stereoscopic viewing techniques. The number of false positives listed are the total for all cases for each radiologist with the average being the average number of false positives per case. Although the difference in the two viewing techniques was not statistically significant, there was an 13.1% (3.11/3.58) decrease in the number of FPs and 28% improvement in sensitivity for inexperienced. For both groups, this corresponds to a 5% increase in the PPV.

Table 6.1: Observer Performance Statistics

Reader #	FPs PA per subject	FPs BCI per subject	AUC PA	AUC BCI	Sensitivity PA	Sensitivity BCI	PPV PA	PPV BCI
Experienced Readers								
1	0.28	0.3	0.958	0.958	89%	89%	0.76	0.75
6	0.68	0.3	0.96	0.957	95%	90%	0.59	0.75
7	0.48	0.3	0.959	0.963	92%	92%	0.66	0.76
8	0.08	0.12	0.972	0.969	74%	84%	0.90	0.88
Inexperienced Readers								
2	0.3	0.43	0.956	0.975	79%	90%	0.73	0.68
3	1.2	1.13	0.82	0.841	87%	93%	0.42	0.46
4	0.28	0.3	0.957	0.975	87%	92%	0.76	0.76
5	0.28	0.23	0.908	0.946	72%	79%	0.72	0.77
Average for experienced	0.32	0.26	0.962	0.961	87%	89%	0.68	0.72
Average for inexperienced	0.52	0.52	0.910	0.934	81%	89%	0.68	0.73

Results for the stereoscopic CAD viewing did not improve the detection results and were identical to the stereoscopic without CAD. Radiologists commented that the stereoscopic viewing took some adjustment. In particular, one experienced radiologist noted not being comfortable with the stereoscopic images until the middle of the reading.

6.4 DISCUSSION

Lung cancer screening has been a much debated topic for decades. Historically, screening with standard chest radiography has not proven beneficial.[54, 91] The NLST demonstrated that CT provides a possible screening tool for lung cancer;[2, 60] however,

CT is considered a monetarily expensive high dose modality. Results from the chest stereoscopic study performed here indicate a lower dose and lower cost alternative may be feasible compared to CT since the three images were obtained at a combined dose equivalent to a single chest PA. We are guarded in this assertion as the level of improvement was modest (~6% in PPV). Whether this level of improvement is clinically significant is subject to debate. However, considering the novelty of the technology, and lack of reader experience to interpret the data suggests that the level of improvement may be underestimated. Additional investigation with enhanced reader training is warranted to establish the advantage of chest stereoscopy in a more concrete form.

The data set used for this study was relatively small with few true lesions requiring the addition of simulated lesions. Achieving a balance between positively present and not present at all was a difficult task which may have affected the results. The task may have been too easy since several of the sensitivity values were above 90%. This may not indicate all of the advantages of using stereoscopic viewing. Having a larger data set without simulated lesions may be beneficial to the results with stereoscopic viewing. Having a standard moving grid in the acquisition system may also improve the image quality and therefore improve detection. The CAD scheme did not prove beneficial. Further refinement of the CAD algorithm may improve the results.

Stereoscopic visualization was often used in radiography before CT was available, but stereoscopic systems in use at that time were cumbersome.[42] Technology advances have made stereoscopic visualization much more practical. Flat panel detectors allow for fast acquisition and 3D monitors are now readily available. The stereoscopic mirror technology used for the monitor in this study necessitated observers

to adjust their vision to a “sweet spot” in the center of the visual plane. Monitors that provide a stereoscopic view from any angle may make the visualization task even less cumbersome and more comfortable to observers than the mirror based technology used in this study.

The design of the observer study used in this research may have biased the standard chest PA results. By providing the observer with the PA image immediately prior to the stereoscopic image allowed the observer to make decisions based on the PA image. Therefore, the stereoscopic image provided more of a second supplemental reading rather than an independent reading. A different design may be to have one viewing of the standard PA images only, then at a later date, a second viewing of the stereoscopic images only. That type of study was not feasible with the data set available since most of the images were augmented with simulated lesions such that each image would have been viewed twice in the same reading. Furthermore, the aims of that type of study design would establish a different role for BCI as an independent imaging modality. In this study, a more conservative approach was taken by testing BCI as an adjunct modality to PA.

As with any new radiographic viewing technique, the training time becomes a consideration. The observers did not demonstrate comfort with the stereoscopic view until well into the study. Although the study was randomized to balance the lack of training, more thorough training over time and consistent use in the clinic may increase the benefits of stereoscopic visualization.

The current study indicated that stereoscopic visualization as an adjunct modality to single view chest x-ray may improve the detection of subtle lung nodules for

radiologists trainees while reducing FPs for all radiologists. To further establish effectiveness, future endeavors should include a more robust data set, an unbiased observer study design, more extensive training for observers, and the latest technology of stereoscopic monitors available. Multiview chest radiology could provide further benefits as seen from a multiview study for breast.[137]

CHAPTER 7

Conclusion

The introduction of this dissertation described the challenges involved in detecting subtle lung nodules. In spite of advances in technology, detection of subtle lung lesions is still problematic due to the complicated structure of anatomical noise prevalent in the lung field. Stereoscopic imaging was used in radiology departments before CT and MRI systems more available. CT has been demonstrated to be the best tool for identifying subtle lung lesions; however, CT is a higher dose and higher financial cost modality since CT requires sophisticated equipment and software as well as longer reading times compared to other modalities. In addition, chest CT results in higher exposure to the breast compared to posterior-anterior imaging which protects the breast tissue. Exposure to the sensitive breast tissue is of particular concern for children and young adults since the breast tissue in those age groups is especially sensitive to radiation exposure. This dissertation explored using stereo/BCI as an alternative to lung lesion detection. Stereo/BCI is a lower dose and cost modality compared to CT while providing better protection of radiation exposure to the breast tissue. Stereo/BCI requires modest modifications to existing chest x-ray systems, but does not require additional software to manipulate the images for viewing and should not increase reading time for radiologists. A stereo/BCI modality may provide improved detection compared to chest radiography since such a modality visually suppresses anatomical noise.

Flat panel detectors and improvements in 3D monitors have made the use of a stereoscopic modality like stereo/BCI feasible and less cumbersome than previous generations of stereoscopic technology. The optimal geometry of systems which employ

flat panel detectors has not been sufficiently investigated. A theoretical study found that the focal spot size was the leading cause of resolution degradation. The eDQE was used as a better overall system metric which accounts for scatter and magnification in system design. By using magnification which introduced an air gap thus lowering scatter to the detector, the eDQE was seen to improve with the use of geometrical magnification.

Theoretical results indicated that detection could benefit by incorporating geometrical magnification of approximately 1.5 without increasing the dose to the patient. The study demonstrated tradeoffs in system design dependent upon the desired task of the system. However, incorporating geometrical magnification will require larger detectors resulting in a possible increase in system cost. Future directions for the theoretical framework would include a frequency dependent scatter model and direct detection receptor model.

The geometrical magnification study performed in Chapter 2 was a theoretical study while Chapter 4 examined the effects of magnification for stereo/BCI and single view chest radiography using a clinical imaging system. Employing anthropomorphic chest phantoms provided a better approximation to clinical system performance under real clinical settings. Stereo/BCI and single view chest x-ray were compared for an average adult phantom and a large adult phantom at two magnifications under iso-dose conditions. Stereo/BCI was ~100 times higher than single view CXR at low frequencies for all conditions. The results demonstrated that magnification improves detection for both modalities without an increase in dose for the adult phantom but not for the large adult phantom. Similarly, the low frequency eDQE was seen to improve with magnification corresponding to an improvement in the Hotelling SNR^2 detectability index. These results were consistent with the theoretical findings which indicated

tradeoffs in system design depending on the desired task. The clinical assessment could also be formalized with a frequency dependent scatter approximation as well as formal magnification optimization and examination of effects of focal spot size.

Stereo/BCI and single view CXR were further compared to a geometrical phantom. In the absence of anatomy, the eDQE was seen to improve by a factor of ~10 compared to stereo/BCI and a factor of ~1000 compared to single view CXR indicating that anatomy does affect the detection of subtle lung nodules. The eDQE(0) for the geometrical phantom was approximately 10% while the eDQE(0) for the object free study was approximately 60% indicating that the introduction of scatter affects the eDQE. The assumptions made for the object free study may indicate maximum performance rather than realistic performance but the difference indicates a need for clinical setting assessment.

Our study assumed that all anatomy is detrimental to lesion detection which may indicate worst case rather than realistic results. Observers can see “through” certain anatomy and therefore the affect of certain anatomy can be null. Other anatomy may help to define what is normal versus abnormal and actually have a positive affect on the detection of lesions. However, the study indicated that anatomy does affect overall system performance. Future work could investigate a more sophisticated model to fully characterize anatomical noise by examining the specific affects of different anatomical structures on detection.

To further examine the benefits of stereo/BCI in detection of subtle lung nodules, a human subject study was performed. A clinical x-ray system was modified to have horizontal tube translation such that images could be obtained at the PA (iso-center)

position as well as oblique angles at ± 3 . The images were processed for optimal viewing and displayed on a stereoscopic monitor for radiologists to score in terms of lung nodule detection. The human subject data obtained consisted of only a few abnormal cases necessitating the addition of simulated lesions to the human subject data set. A correlated CAD component was also included. The images were shown to eight radiologists on a stereoscopic monitor for scoring the presence of subtle lung nodules. The radiologists were asked to score the PA image, the monoscopic image followed by the stereoscopic image and the stereoscopic CAD image. The total number of false positives was reduced by $\sim 13\%$ for the monoscopic followed by stereo/BCI modality. For the radiology fellows, the AUC for lesion detection was further improved by 2.8% while the CAD component did not prove beneficial. The observer studies gave consistent results and demonstrated an improvement with stereo/BCI.

The study indicated the performance of stereo/BCI as an adjunct rather than a standalone modality; therefore, full benefits of stereo/BCI may not have been realized. Also, the high sensitivity results for the study indicate that the detection task may have been too easy which again may not indicate the full benefit of stereo/BCI. The data set was not robust and the simulated lesions could have been more subtle and more obscured by anatomy to better demonstrate the effects of anatomical suppression through stereoscopic visualization. Observer training may also improve the effectiveness of a modality such as stereo/BCI. The stereoscopic view has a much different look and feel than a monoscopic view and adjusting to this difference may require more extensive training over a longer period of time. The stereoscopic monitor used for this study would be too cumbersome for clinical practice. Current stereoscopic monitor technology uses

only one monitor providing the ability to see stereoscopically from specific directions without glasses. Such a monitor would be better accepted in a clinical environment and should be investigated for use with a modality like stereo/BCI.

The studies presented did not use an antiscatter grid for image acquisition although antiscatter grids are used in chest x-ray systems. An antiscatter grid would not have been perpendicular to the images acquired at the oblique angles and thus not representative of scatter rejection achieved for the PA images in the study or chest x-ray systems used clinically. By not incorporating a grid, the scatter component for all the images was similar. The incorporation of a scatter rejection method would prove beneficial for the performance of stereo/BCI. Air gaps have comparable scatter rejection potential as antiscatter grids. The phantom study incorporated an air gap which resulted in a 20% reduction in scatter. However, use of an air gap necessitates larger detectors. The size of flat panel detectors has almost doubled since their introduction into the marketplace while the cost has remained nearly constant. The flat panel detectors can be expected to continue increasing in size; however, the cost versus benefit should be examined in future endeavors.

Additional data acquisition at ± 6 degrees would allow the observer to pan through three stereoscopic image pairs. This would provide the observer with the ability to simulate movement and thus a better visual removal of the anatomy. Since work has shown that increasing dose does not necessarily improve detection, these additional views may be obtained without an increase in the total dose. Assessing the additional stereoscopic views may require an increase in the reading time but the benefits could negate the additional reading time.

Although the work presented here was for chest, other studies have found stereomammography beneficial in the detection of lesions in the breast. Therefore, future work could include an examination of the use of stereoscopic visualization for other radiology techniques.

REFERENCES

1. *Healthcare spending and the Medicare program*. 2010 January 17, 2011]; Available from: <http://www.medpac.gov/documents/Jun10DataBookEntireReport.pdf>.
2. Aberle, D.R., Adams, A.M., Berg, C.D., et al, *Reduced Lung-Cancer Mortality with Low-Dose Computed Tomographic Screening*. N Engl J Med, 2011. **365**(5): p. 395-409.
3. ACS, *Cancer Facts and Figures 2010*. American Cancer Society, Atlanta, GA, 2010.
4. Albagli, D., et al. *Performance of advanced a-Si/CsI-based flat panel x-ray detectors for mammography*. in *Medical Imaging 2003: Physics of Medical Imaging, Feb 16-18 2003*. 2003. San Diego, CA, United States: The International Society for Optical Engineering.
5. Alvarez, R.E., J.A. Seibert, and S.K. Thompson, *Comparison of dual energy detector system performance*. Med Phys, 2004. **31**(3): p. 556-65.
6. Antonuk, L.E., et al., *Initial performance evaluation of an indirect-detection, active matrix flat-panel imager (AMFPI) prototype for megavoltage imaging*. Int J Radiat Oncol Biol Phys, 1998. **42**(2): p. 437-54.
7. Bacher, K., et al., *Image quality and radiation dose on digital chest imaging: comparison of amorphous silicon and amorphous selenium flat-panel systems*. AJR Am J Roentgenol, 2006. **187**(3): p. 630-7.
8. Barber, W.C., Nygard, E., Wessel, J. C., Malakhov, N., Wawrzyniak, G., Hartsough, N. E., Gandhi, T., Beck, T. J., Taguchi, K., Iwanczyk, J. S., *Large area photon counting x-ray imaging arrays for clinical dual-energy applications*. 2009 IEEE Nuclear Science Symposium Conference Record, 2009: p. 3029-3031.
9. Barrett, H.H. and W. Swindell, *Radiological imaging : the theory of image formation, detection, and processing* 1981, New York: Academic Press. 2 v. (xxiii, 693).
10. Berbaum, K. *Medial Image Perception Library, DBM MRMC Description*. 2006 [cited 2012 May 2012]; Available from: <http://perception.radiology.uiowa.edu/Software/ReceiverOperatingCharacteristicROC/DBMMRMC/tabid/116/Default.aspx>.
11. Berlin, L., *Accuracy of diagnostic procedures: has it improved over the past five decades?* AJR Am J Roentgenol, 2007. **188**(5): p. 1173-8.

12. Berrington de Gonzalez, A., et al., *Projected cancer risks from computed tomographic scans performed in the United States in 2007*. Arch Intern Med, 2009. **169**(22): p. 2071-7.
13. Bley, T.A., et al., *Comparison of radiologist and CAD performance in the detection of CT-confirmed subtle pulmonary nodules on digital chest radiographs*. Invest Radiol, 2008. **43**(6): p. 343-8.
14. Boone, J.M., et al., *Scatter/primary in mammography: comprehensive results*. Medical Physics, 2000. **27**(10): p. 2408-16.
15. Boyce, S., et al., *Preliminary Evaluation of Biplane Correlation (BCI) Stereographic Imaging for Lung Nodule Detection*. Journal of Digital Imaging, 2013. **26**(1): p. 109-114.
16. Boyce, S.J., Chawla, A., Samei, E., *Physical evaluation of a high frame rate, extended dynamic range flat panel detector for real-time cone beam computed tomography applications*. SPIE Physics of Medical Imaging 2005, 2005. **5745**: p. 591-599.
17. Boyce, S.J. and E. Samei, *Imaging properties of digital magnification radiography*. Medical Physics, 2006. **33**(4): p. 984-996.
18. Brenner, D.J. and E.J. Hall, *Computed tomography--an increasing source of radiation exposure*. N Engl J Med, 2007. **357**(22): p. 2277-84.
19. Burgess, A.E., *An empirical equation for screen MTFs*. Med Phys, 1978. **5**(3): p. 199-204.
20. Burgess, A.E., Li, X., Abbey, C. K., *Nodule detection in two-component noise: toward patient structure*. Proc of SPIE, 1997. **3036**: p. 2-13.
21. Chaussat, C., et al., *New CsI/a-Si 17"x17" x-ray flat-panel detector provides superior detectivity and immediate direct digital output for general radiography systems*. Proceedings of SPIE - The International Society for Optical Engineering, 1998. **3336**: p. 45-56.
22. Chawla, A., Boyce, S., Samei, E., *Design of a New Multi-projection Imaging System for Chest Radiography*. Nuclear Science Symposium Conference Record, IEEE, 2007: p. 2996 - 2999.
23. Chotas, H.G., J.T. Dobbins, 3rd, and C.E. Ravin, *Principles of digital radiography with large-area, electronically readable detectors: a review of the basics*. Radiology, 1999. **210**(3): p. 595-9.

24. Cowen, A.R., A.G. Davies, and S.M. Kengyelics, *Advances in computed radiography systems and their physical imaging characteristics*. Clin Radiol, 2007. **62**(12): p. 1132-41.
25. Diekmann, F., et al., [*Comparing the visualization of microcalcifications with direct magnification in digital full-field mammography vs. film-screen mammography*]. Rofo, 2002. **174**(3): p. 297-300.
26. Dobbins III, J.T., McAdams, H. P., Song, J-W, Li, C. M., Godfrey, D. J., DeLong, D. M., Paik, S-H, Martinez-Jimenez, S., *Digital tomosynthesis of the chest for lung nodule detection: interim sensitivity results from an ongoing NIH-sponsored trial*. Medical Physics, 2008. **35**: p. 2554-2557.
27. Dobbins III, J.T., et al., *Intercomparison of methods for image quality characterization. II. Noise power spectrum*. Medical Physics, 2006. **33**(5): p. 1466-1475.
28. Dobbins, J.T., 3rd and D.J. Godfrey, *Digital x-ray tomosynthesis: current state of the art and clinical potential*. Phys Med Biol, 2003. **48**(19): p. R65-106.
29. Dobbins, J.T., 3rd and H.P. McAdams, *Chest tomosynthesis: technical principles and clinical update*. Eur J Radiol, 2009. **72**(2): p. 244-51.
30. Du, H., et al., *Investigation of the signal behavior at diagnostic energies of prototype, direct detection, active matrix, flat-panel imagers incorporating polycrystalline HgI₂*. Phys Med Biol, 2008. **53**(5): p. 1325-51.
31. Endo, M., et al., *Performance of cone beam CT using a flat-panel imager*. Proceedings of the SPIE - The International Society for Optical Engineering, 2001. **4320**: p. 815-21.
32. Fazel, R., et al., *Exposure to low-dose ionizing radiation from medical imaging procedures*. N Engl J Med, 2009. **361**(9): p. 849-57.
33. Fink, C., et al., *Clinical comparative study with a large-area amorphous silicon flat-panel detector: image quality and visibility of anatomic structures on chest radiography*. AJR Am J Roentgenol, 2002. **178**(2): p. 481-6.
34. Fischbach, F., et al., *Dual-energy chest radiography with a flat-panel digital detector: revealing calcified chest abnormalities*. AJR Am J Roentgenol, 2003. **181**(6): p. 1519-24.
35. Fischbach, F., et al., *Flat panel digital radiography compared with storage phosphor computed radiography: assessment of dose versus image quality in phantom studies*. Invest Radiol, 2002. **37**(11): p. 609-14.

36. Fischer, P., Helmich, A., Lindner, M., Wermes, N., Blanquart, L., *A photon counting pixel chip with energy windowing*. IEEE Transactions on Nuclear Science, 2000. **47**(3): p. 881-884.
37. Floyd, C.E., Jr., et al., *Quantitative scatter measurement in digital radiography using a photostimulable phosphor imaging system*. Med Phys, 1991. **18**(3): p. 408-13.
38. Floyd, C.E., Jr., et al., *Imaging characteristics of an amorphous silicon flat-panel detector for digital chest radiography*. Radiology, 2001. **218**(3): p. 683-8.
39. Flynn, M.J., *Processing Digital Radiographs of Specific Body Parts*. Advances in Digital Radiography: RSNA Categorical Course in Diagnostic Radiology Physics 2003, 2003: p. 71-78.
40. Flynn, M.J. and E. Samei, *Experimental comparison of noise and resolution for 2k and 4k storage phosphor radiography systems*. Med Phys, 1999. **26**(8): p. 1612-23.
41. Flynn, M.J., E. Samei, and D.A. Reimann, *Experimental comparison of noise and resolution for 2K and 4K storage phosphor chest radiography systems*. Radiology, 1996. **201**: p. 1082-1082.
42. Getty, D.J., *Stereoscopic and Biplane Imaging*, in *Advances in Digital Radiography 2003*, Radiological Society of North America (RSNA) Publication: Oak Brook, IL. p. 199-209.
43. Getty, D.J., D'Orsi, C. J., Pickett, R. M., *Stereoscopic Digital Mammography: Improved Accuracy of Lesion Detection in Breast Cancer Screening*. Lecture Notes in Computer Science, 2008. **5116**: p. 74-79.
44. Giger, M.L., Doi, Kunio, and MacMahon, *Image feature analysis and computer-aided diagnosis in digital radiography. 3. Automated detection of nodules in peripheral lung fields*. Medical Physics, 1988. **15**(2): p. 158-166.
45. Ginneken, B.v., B.M.t.H. Romeny, and M.A. Viergever, *Computer-Aided Diagnosis in Chest Raiography: A Survey*. IEEE Transactions on Medical Imaging, 2001. **20**(12): p. 1228-1241.
46. Goodsitt, M.M., H.P. Chan, and L. Hadjiiski, *Stereomammography: evaluation of depth perception using a virtual 3D cursor*. Med Phys, 2000. **27**(6): p. 1305-10.
47. Granfors, P.R., et al., *Performance of a flat panel cardiac detector*. Proceedings of the SPIE - The International Society for Optical Engineering, 2001. **4320**: p. 77-86.

48. Granfors, P.R. and R. Aufrichtig, *DQE(f) of an amorphous silicon flat panel X-ray detector: detector parameter influences and measurement methodology*. Proceedings of the SPIE - The International Society for Optical Engineering, 2000. **3977**: p. 2-13.
49. Granfors, P.R. and R. Aufrichtig, *Performance of a 41X41-cm² amorphous silicon flat panel x-ray detector for radiographic imaging applications*. Med Phys, 2000. **27**(6): p. 1324-31.
50. Guo, W., et al., *A computerized scheme for lung nodule detection in multiprojection chest radiography*. Medical Physics, 2012. **39**(4): p. 2001-2012.
51. Hall, E.J. and D.J. Brenner, *Cancer risks from diagnostic radiology*. Br J Radiol, 2008. **81**(965): p. 362-78.
52. Hermann, K.P., et al., *Magnification mammography: a comparison of full-field digital mammography and screen-film mammography for the detection of simulated small masses and microcalcifications*. Eur Radiol, 2002. **12**(9): p. 2188-91.
53. Higginbotham, J., Gupta, A, Wurm, A, Nguyen, J. *Introduction to Chest Radiology*. [cited 2013; Available from: <http://www.med-ed.virginia.edu/courses/rad/cxr/index.html>].
54. Hirsch, F.R., Franklin, Wilbur A., Gazdar, Adi F. and Bunn, Jr., Paul A., *Early Detection of Lung Cancer: Clinical Perspectives of Recent Advances in Biology and Radiology*. Clinical Cancer Research, 2001. **7**: p. 5-22.
55. Hricak, H., Brenner, D. J., Adelstein, S. J., Frush, D. P., Hall, E. J., Howell, R. W., McCollough, C. H., Mettler, F. A., Pearce, M. S., Suleiman, O. H., Thrall, J. H., Wagner, L. K. , *Managing Radiation Use in Medical Imaging: A Multifaceted Challenge*. Radiology, 2010. **10101157**.
56. IEC, *Medical diagnostic x-ray equipment - Radiation conditions for use in the determination of characteristics*, in IEC-6220-12003, International Electrotechnical Commission: Geneva, Switzerland.
57. IEC, *Medical electrical equipment - characteristics of digital x-ray imaging devices: part 1. Determination of the detective quantum efficiency*, in IEC 62220-12003, International Electrotechnical Commission: Geneva.
58. Illers, H., et al., *Measurement of the modulation transfer function of digital X-ray detectors with an opaque edge-test device*. Radiat Prot Dosimetry, 2005. **114**(1-3): p. 214-9.

59. Illers, H., E. Buhr, and C. Hoeschen, *Measurement of the detective quantum efficiency (DQE) of digital X-ray detectors according to the novel standard IEC 62220-1*. Radiat Prot Dosimetry, 2005. **114**(1-3): p. 39-44.
60. Institute, N.C., *Lung cancer trial results show mortality benefit with low-dose CT*. 2010.
61. Kakeda, S., et al., *Improved detection of lung nodules on chest radiographs using a commercial computer-aided diagnosis system*. AJR Am J Roentgenol, 2004. **182**(2): p. 505-10.
62. Knoll, G.F., *Radiation Detection and Measurement*. 2nd ed 1979, New York: John Wiley & Sons, Inc.
63. Korner, M., et al., *Depiction of low-contrast detail in digital radiography: comparison of powder- and needle-structured storage phosphor systems*. Invest Radiol, 2006. **41**(7): p. 593-9.
64. Krol, A., et al., *Scatter reduction in mammography with air gap*. Medical Physics, 1996. **23**(7): p. 1263-70.
65. Kubo, T., et al., *Radiation dose reduction in chest CT: a review*. AJR Am J Roentgenol, 2008. **190**(2): p. 335-43.
66. Kuenstler, L.W.G.a.P., *A retrospective view of survey photofluorocarbons of persons with lung cancer*. Cancer, 1960. **13**(91-95).
67. Kundel, H.L., C.F. Nodine, and D. Carmody, *Visual scanning, pattern recognition and decision-making in pulmonary nodule detection*. Invest Radiol, 1978. **13**(3): p. 175-81.
68. Law, J., *Breast dose from magnification films in mammography*. Br J Radiol, 2005. **78**(933): p. 816-20.
69. Li, F., et al., *Improved detection of small lung cancers with dual-energy subtraction chest radiography*. AJR Am J Roentgenol, 2008. **190**(4): p. 886-91.
70. Li, F., et al., *Lung cancers missed on chest radiographs: results obtained with a commercial computer-aided detection program*. Radiology, 2008. **246**(1): p. 273-80.
71. Li, X., et al., *Three-dimensional simulation of lung nodules for paediatric multidetector array CT*. Br J Radiol, 2009. **82**(977): p. 401-11.
72. Liu, X., et al., *An alternate line erasure and readout (ALER) method for implementing slot-scan imaging technique with a flat-panel detector--initial experiences*. IEEE Trans Med Imaging, 2006. **25**(4): p. 496-502.

73. Liu, X., et al., *Scatter rejection and low-contrast performance of a slot-scan digital chest radiography system with electronic aft-collimation: a chest phantom study*. Med Phys, 2008. **35**(6): p. 2391-402.
74. Locker, M., Fischer, P., Krimmel, S., Kruger, H., Lindner, M., Nakazawa, K., Takahashi, T., Wermes, N., *Single photon counting x-ray imaging with Si and CdTe single chip pixel detectors and multichip pixel modules*. IEEE Transactions on Nuclear Science, 2004. **51**(4): p. 1717-1723.
75. Madan, A.K., et al., *Magnification views of mammography decrease biopsy rates*. Am Surg, 2001. **67**(7): p. 687-9.
76. McAdams, P., et al., *Recent Advances in Chest Radiography*. Radiology, 2006. **241**(3): p. 663-683.
77. McCollough, C.H., et al., *Strategies for reducing radiation dose in CT*. Radiol Clin North Am, 2009. **47**(1): p. 27-40.
78. McKinley, R.L., Samei, E., Tornai, M., Floyd, C.E., *Measurements of a quasi-monochromatic beam for x-ray computed mammatomography*. Proceedings of SPIE, 2004. **5368**: p. 311-319.
79. McKinley, R.L., Tornai, M.P., Samei, E., Bradshaw, M.L., *Simulation study of a quasi-monochromatic beam for x-ray computed mammatomography*. Med Phys, 2004. **31**(4): p. 800-813.
80. Mettler, F.A., Jr., et al., *Effective doses in radiology and diagnostic nuclear medicine: a catalog*. Radiology, 2008. **248**(1): p. 254-63.
81. Mettler, F.A., Jr., et al., *Medical radiation exposure in the U.S. in 2006: preliminary results*. Health Phys, 2008. **95**(5): p. 502-7.
82. Mettler, J., F. A., Bhargavan, M., Faulkner, K., Gilley, D. B., Gray, J. E., Ibbott, G. S., Lipoti, J. A., Mahesh, M., McCrohan, J. L., Stabin, M. G., Thomadsen, B. R., Yoshizumi, T. T., *Radiologic and nuclear medicine studies in the United States and worldwide: Frequency, radiation dose, and comparison with other radiation sources - 1950-2007*. Radiology, 2009. **253**: p. 520-531.
83. Metz, C.E. *Metz ROC Software*. [cited 2010 May 2010]; Available from: <http://metz-roc.uchicago.edu/MetzROC/software>.
84. Monnin, P., et al., *Performance comparison of an active matrix flat panel imager, computed radiography system, and a screen-film system at four standard radiation qualities*. Med Phys, 2005. **32**(2): p. 343-50.
85. Muhm, J.R., et al., *Lung cancer detected during a screening program using four-month chest radiographs*. Radiology, 1983. **148**: p. 561-565.

86. Muntz, E.P., *Analysis of the significance of scattered radiation in reduced dose mammography, including magnification effects, scatter suppression, and focal spot and detector blurring*. Med Phys, 1979. **6**(2): p. 110-7.
87. Muntz, E.P., et al., *Electronic grids for electrostatic imaging systems*. Radiology, 1976. **121**(1): p. 197-204.
88. Nasab, N.M. and E. Samei. *The impact of angular separation on the performance of biplane correlation imaging for lung nodule detection*. 2006. San Diego, CA, USA: SPIE.
89. Nasab, N.M., E. Samei, and J.T. Dobbins III. *Biplane correlation imaging for lung nodule detection: initial human subject results*. 2006. San Diego, CA, USA: SPIE.
90. Neitzel, U., et al., *Determination of the detective quantum efficiency of a digital x-ray detector: Comparison of three evaluations using a common image data set*. Medical Physics, 2004. **31**(8): p. 2205-2211.
91. Patz, E.F., Jr., P.C. Goodman, and G. Bepler, *Screening for lung cancer*. N Engl J Med, 2000. **343**(22): p. 1627-33.
92. Perisinakis, K., et al., *Film-Screen Magnification Versus Electronic Magnification and Enhancement of Digitized Contact Mammograms in the Assessment of Subtle Microcalcifications*. Investigative Radiology, 2001. **36**(12): p. 726-733.
93. Pinto, A. and L. Brunese, *Spectrum of diagnostic errors in radiology*. World J Radiol, 2010. **2**(10): p. 377-83.
94. Planar Systems, I. *Planar 3D: Stereoscopic display technology*. 27 April 2011]; Available from: <http://www.planar3d.com/3d-technology/stereoscopic-101/>.
95. Ranger, N.T., et al., *Assessment of Detective Quantum Efficiency: Intercomparison of a Recently Introduced International Standard with Prior Methods*. Radiology, 2007. **243**(3): p. 785-795.
96. Richard, S. and J.H. Siewerdsen, *Cascaded systems analysis of noise reduction algorithms in dual-energy imaging*. Med Phys, 2008. **35**(2): p. 586-601.
97. Rivetti, S., et al., *Comparison of different computed radiography systems: physical characterization and contrast detail analysis*. Med Phys, 2010. **37**(2): p. 440-8.
98. Roessl, E. and R. Proksa, *K-edge imaging in x-ray computed tomography using multi-bin photon counting detectors*. Phys Med Biol, 2007. **52**(15): p. 4679-96.
99. Rowlands, J.A., *The physics of computed radiography*. Phys Med Biol, 2002. **47**(23): p. R123-66.

100. Ruhl, R., et al., *CsI-detector-based dual-exposure dual energy in chest radiography for lung nodule detection: results of an international multicenter trial*. Eur Radiol, 2008. **18**(9): p. 1831-9.
101. Samei, E., *Image quality in two phosphor-based flat panel digital radiographic detectors*. Med Phys, 2003. **30**(7): p. 1747-57.
102. Samei, E., et al., *Bi-plane correlation imaging for improved detection of lung nodules*. Medical Imaging 2003: Physics of Medical Imaging, 2003. **5030**: p. 284-297.
103. Samei, E. and M.J. Flynn, *An experimental comparison of detector performance for computed radiography systems*. Med Phys, 2002. **29**(4): p. 447-59.
104. Samei, E. and M.J. Flynn, *An experimental comparison of detector performance for direct and indirect digital radiography systems*. Med Phys, 2003. **30**(4): p. 608-22.
105. Samei, E., et al. *DQE of direct and indirect digital radiography systems*. 2001. San Diego, CA, USA: SPIE.
106. Samei, E., M.J. Flynn, and W.R. Eyler, *Simulation of subtle lung nodules in projection chest radiography*. Radiology, 1997. **202**(1): p. 117-24.
107. Samei, E., M.J. Flynn, and W.R. Eyler, *Detection of subtle lung nodules: Relative influence of quantum and anatomic noise on chest radiographs*. Radiology, 1999. **213**(3): p. 727-734.
108. Samei, E., et al., *Subtle lung nodules: influence of local anatomic variations on detection*. Radiology, 2003. **228**(1): p. 76-84.
109. Samei, E., M.J. Flynn, and D.A. Reimann, *A method for measuring the presampled MTF of digital radiographic systems using an edge test device*. Medical Physics, 1998. **25**(1): p. 102-113.
110. Samei, E., Flynn, M. J., Eyler, W. R., *Detection of subtle lung nodules: relative influence of quantum and anatomical noise on chest radiographs*. Radiography, 1999. **213**: p. 727-734.
111. Samei, E., et al., *Comparative scatter and dose performance of slot-scan and full-field digital chest radiography systems*. Radiology, 2005. **235**(3): p. 940-9.
112. Samei, E., et al., *Intercomparison of methods for image quality characterization. I. Modulation transfer function*. Medical Physics, 2006. **33**(5): p. 1454-1465.
113. Samei, E., et al., *Effective dose efficiency: an application-specific metric of quality and dose for digital radiography*. Phys Med Biol, 2011. **56**(16): p. 5099-5118.

114. Samei, E., et al., *Detector or system? Extending the concept of detective quantum efficiency to characterize the performance of digital radiographic imaging systems*. Radiology, 2008. **249**(3): p. 926-37.
115. Samei, E., et al., *Effective DQE (eDQE) and speed of digital radiographic systems: an experimental methodology*. Med Phys, 2009. **36**(8): p. 3806-17.
116. Samei, E., et al., *Fundamental imaging characteristics of a slot-scan digital chest radiographic system*. Medical Physics, 2004. **31**(9): p. 2687-2698.
117. Samei, E., et al., *Multiprojection correlation imaging for improved detection of pulmonary nodules*. AJR Am J Roentgenol, 2007. **188**(5): p. 1239-45.
118. Saunders, R.S. and E. Samei, *A method for modifying the image quality parameters of digital radiographic images*. Medical Physics, 2003. **30**(11): p. 3006-3017.
119. Saunders, R.S., Samei, E., Majdi-Nasab, N., Lo, J. Y., *Initial human subject results for breast bi-plane correlation imaging technique*. Proceedings of SPIE, 2007. **6514**.
120. Schaefer-Prokop, C.M., et al., *DR and CR: Recent advances in technology*. Eur J Radiol, 2009. **72**(2): p. 194-201.
121. Schaetzing, R., *Computed Radiography Technology*, in *Advances in Digital Radiography 2003*, Radiological Society of North America (RSNA) Publication: Oak Brook, IL. p. 7-22.
122. Schwartz, A.G., P. Yang, and G.M. Swanson, *Familial risk of lung cancer among nonsmokers and their relatives*. Am J Epidemiol, 1996. **144**(6): p. 554-62.
123. Schwarz, C., Campbell, M., Goepper, R., Ludwig, J., Mikulec, B., Runge, K., Smith, K. M., Snoeys, W., *Measurements with Si and GaAs pixel detectors bonded to photon counting readout chips*. Nuclear Instruments and Methods in Physics Research, 2001. **A(466)**: p. 87-94.
124. Shaw, C.C., et al., *Optimization of MTF and DQE in magnification radiography-a theoretical analysis*. Proceedings of the SPIE - The International Society for Optical Engineering, 2000. **3977**: p. 466-75.
125. Shaw, R., *The equivalent quantum efficiency of the photographic process*. J. Photogr. Sci, 1963. **11**: p. 199-204.
126. Shikhaliev, P.M., *Tilted angle CZT detector for photon counting/energy weighting x-ray and CT imaging*. Phys Med Biol, 2006. **51**(17): p. 4267-87.

127. Siewerdsen, J.H., et al., *Empirical and theoretical investigation of the noise performance of indirect detection, active matrix flat-panel imagers (AMFPIs) for diagnostic radiology*. Med Phys, 1997. **24**(1): p. 71-89.
128. Siewerdsen, J.H. and D.A. Jaffray, *A ghost story: spatio-temporal response characteristics of an indirect-detection flat-panel imager*. Med Phys, 1999. **26**(8): p. 1624-41.
129. Siewerdsen, J.H. and D.A. Jaffray, *Optimization of x-ray imaging geometry (with specific application to flat-panel cone-beam computed tomography)*. Med Phys, 2000. **27**(8): p. 1903-14.
130. Singh, H., Sethi, S., Raber, M., Petersen, L. A., *Errors in Cancer Diagnosis: Current Understanding and Future Directions*. Journal of Clinical Oncology, 2007. **25**(31): p. 5009-5018.
131. Smith-Bindman, R., *Is Computed Tomography Safe?* The New England Journal of Medicine, 2010. **363**: p. 1-4.
132. Sorenson, J.A. and J. Floch, *Scatter Rejection by Air Gaps - an Empirical-Model*. Medical Physics, 1985. **12**(3): p. 308-316.
133. Tognina, C.A., Mollov, Ivan, Yu, Jiann M., Webb, Chris, Roos, Pieter G., Batts, Mark, Trinh, Delenah, Fong, Robert, Taie-Nobraie, Nima, Nepo, Boris, Job, Isaias D., Gray, Keith, Boyce, Sarah, Colbeth, Richard E., *Design and performance of a new a-Si flat-panel imager for use in cardiovascular and mobile C-arm imaging systems*. Proc. SPIE, 2004. **5368**: p. 648-656.
134. Uffmann, M., et al., *Computed radiography and direct radiography: influence of acquisition dose on the detection of simulated lung lesions*. Invest Radiol, 2005. **40**(5): p. 249-56.
135. Vedantham, S., et al., *Full breast digital mammography with an amorphous silicon-based flat panel detector: physical characteristics of a clinical prototype*. Medical Physics, 2000. **27**(3): p. 558-67.
136. Vikgren, J., et al., *Comparison of chest tomosynthesis and chest radiography for detection of pulmonary nodules: human observer study of clinical cases*. Radiology, 2008. **249**(3): p. 1034-41.
137. Webb, L.J., et al., *Comparative performance of multiview stereoscopic and mammographic display modalities for breast lesion detection*. Medical Physics, 2011. **38**(4): p. 1972-1980.
138. Weiss, J.M., et al., *Menstrual and reproductive factors in association with lung cancer in female lifetime nonsmokers*. Am J Epidemiol, 2008. **168**(11): p. 1319-25.

139. Wikipedia, T.F.E., *Wilhelm Rontgen*. 2011.
140. Xu, T., et al., *Dynamic dual-energy chest radiography: a potential tool for lung tissue motion monitoring and kinetic study*. *Phys Med Biol*, 2011. **56**(4): p. 1191-205.
141. Yorkston, J., *Digital Radiographic Technology*, in *Advances in Digital Radiography 2003*, Radiological Society of North America (RSNA) Publication: Oak Brook, IL. p. 23-36.
142. Zhang, Y., Li, X., Segars, W., Samei, W., *Comparative dosimetry of radiography, tomosynthesis, and CT for chest imaging across 59 adult patients*. *Proc of SPIE*, 2013. **8668**(866844): p. 8.